

**A COMPACT DUAL-CIRCULARLY POLARIZED CAVITY-BACKED RING-SLOT ANTENNA**

by

**Riaan Ferreira**

Submitted in partial fulfilment of the requirements for the degree  
Master of Engineering (Electronic Engineering)

in the

Department of Electrical, Electronic and Computer Engineering  
Faculty of Engineering, Built Environment and Information Technology

UNIVERSITY OF PRETORIA

February 2018

## SUMMARY

---

### **A COMPACT DUAL-CIRCULARLY POLARIZED CAVITY-BACKED RING-SLOT ANTENNA**

by

**Riaan Ferreira**

Supervisor: Prof J. Joubert and Prof J. W. Odendaal  
Department: Electrical, Electronic and Computer Engineering  
University: University of Pretoria  
Degree: Master of Engineering (Electronic Engineering)  
Keywords: Artificial magnetic conductor (AMC) reflector, branch-line coupler, low profile structure, circular polarization, ring-slot antennas, uni-directional.

Dual-circularly polarized antennas usually consist of a radiating structure and a feed network capable of generating the  $\pm 90^\circ$  modes required for dual circular polarization. The problem is that these feed networks often take up a large amount of space. It was found that a compact dual-circularly polarized antenna could be made by placing a reduced-size hybrid coupler on top of the center conductor of a ring-slot antenna.

Two cavity-backed ring-slot antennas are presented with unidirectional radiation properties. The first is a linearly polarized CPW-fed ring-slot antenna. A T-shaped CPW feed was used to capacitively excite the ring-slot structure. The bottom of the cavity is formed by an AMC reflector consisting of an array of rectangular patches, a substrate and an electric ground plane. Experimental results for the final antenna design with a size of  $0.457\lambda_0 \times 0.457\lambda_0 \times 0.056\lambda_0$  exhibits a 5.5% impedance bandwidth, maximum gain of approximately 7 dBi, a front-to-back ratio of 15 dB, and good cross-polarization.

In the second design a reduced-size microstrip branch-line coupler was placed on top of the center conductor of the ring-slot in order to feed two T-shaped microstrip feedlines, in order to achieve dual circular polarization. Two coaxial cables were used to feed the branch-line coupler from the back of the structure. This resulted in a significantly better front-to-back

ratio. Experimental results for the final antenna design with a size of  $0.5\lambda_0 \times 0.5\lambda_0 \times 0.056\lambda_0$ , exhibits a 4% isolation bandwidth, 12% impedance bandwidth, maximum gain of approximately 6.8 dBic, and good cross-polarization and axial ratio results were achieved. If the branch-line coupler is removed, dual-linear polarization can be achieved. This makes the antenna polarization diverse. Future work will focus on improving the isolation bandwidth without significantly increasing the overall size of the antenna.

These antennas are simple to manufacture using simple photolithography as no shorting posts or solid sidewalls are necessary. It can potentially be used as a flush-mounted single radiator or as an element for an array. This polarization-diverse small-footprint and low-profile antenna with relatively high gain is a good candidate for 2.4 GHz WLAN applications.

## LIST OF ABBREVIATIONS

AMC	Artificial magnetic conductor
BAN	Body area networks
CP	Circular polarization
CPW	Co-planar waveguide
DCP	Dual circular polarization
EBG	Electromagnetic bandgap
FSS	Frequency selective surface
HIS	High impedance surface
HP	Horizontal polarization
LHCP	Left-hand circular polarization
MMIC	Monolithic microwave integrated circuits
PEC	Perfect electrical conductor
PMC	Perfect magnetic conductor
RFID	Radio frequency identification
RHCP	Right-hand circular polarization
UC	Uniplanar compact
UWB	Ultra-wideband
VP	Vertical polarization
WLAN	Wireless local area network

# TABLE OF CONTENTS

<b>CHAPTER 1</b>	<b>INTRODUCTION .....</b>	<b>1</b>
1.1	PROBLEM STATEMENT .....	1
1.2	RESEARCH OBJECTIVE AND QUESTIONS.....	2
1.3	RESEARCH CONTRIBUTION .....	3
1.4	OVERVIEW OF STUDY .....	4
<b>CHAPTER 2</b>	<b>LITERATURE STUDY .....</b>	<b>5</b>
2.1	CHAPTER OBJECTIVES .....	5
2.2	METAMATERIAL BASED REFLECTORS .....	5
2.2.1	Advantages of using a metamaterial surface reflector.....	5
2.2.2	Fundamental concepts of metamaterial surfaces .....	6
2.2.3	AMC geometries.....	8
2.3	COMPACT ANTENNAS AND DESIGN CONSIDERATIONS.....	9
2.4	SLOT ANTENNAS .....	11
2.4.1	Different types of slot antennas found in literature .....	11
2.4.2	Ring-slot antennas found in literature.....	12
2.5	ANTENNAS WITH DUAL-CIRCULAR POLARIZATION.....	13
2.5.1	Dual-circularly polarized antennas in literature.....	13
2.5.2	Proposed dual-circularly polarized ring-slot antenna .....	15
<b>CHAPTER 3</b>	<b>SIMULATION STUDY.....</b>	<b>17</b>
3.1	CHAPTER OBJECTIVES .....	17
3.2	CPW-FED RING-SLOT ANTENNAS.....	17
3.2.1	Simulation study of a CPW-fed ring-slot antenna.....	17
3.2.2	Capacitively-fed CPW ring-slot antenna. ....	22
3.3	MICROSTRIP-FED RING-SLOT ANTENNAS .....	28
3.3.1	Ring-slot antenna with a single center-fed microstrip capacitive feed. ....	28
3.3.2	Ring-slot antenna with center-fed microstrip capacitive feed. ....	34
3.4	RING-SLOT ANTENNAS LOADED WITH AMC REFLECTORS .....	39
3.4.1	Square patch AMC analysis and design.....	39
3.4.2	Capacitively-fed CPW ring-slot on top of an AMC reflector.....	44
3.4.3	Dual-fed microstrip ring-slot loaded with an AMC reflector. ....	49
3.5	RING-SLOT ANTENNAS LOADED WITH AMC REFLECTORS .....	52

3.5.1	Reduced size Branch line coupler design. ....	52
3.5.2	Dual circular ring-slot antenna loaded with an AMC reflector. ....	55
<b>CHAPTER 4</b>	<b>MEASURED RESULTS .....</b>	<b>60</b>
4.1	CPW-FED RING-SLOT ANTENNA .....	60
4.1.1	Prototype assembly and S-parameter measurements.....	60
4.1.2	Realized gain and radiation pattern measurements.....	62
4.2	DUAL-CIRCULARLY POLARIZED RING-SLOT ANTENNA .....	65
4.2.1	Prototype assembly and S-parameter measurements.....	65
4.2.2	Realized gain and radiation pattern measurements.....	67
4.2.3	Axial ratio measurements .....	70
<b>CHAPTER 5</b>	<b>CONCLUSION .....</b>	<b>73</b>
5.1	SUMMARY OF WORK.....	73
5.2	CONTRIBUTIONS.....	74
5.3	FUTURE WORK .....	75

# CHAPTER 1 INTRODUCTION

## 1.1 PROBLEM STATEMENT

Circularly polarized (CP) antennas are commonly used in applications such as radio frequency identification (RFID), radar tracking and satellite communication systems. The use of circularly polarized antennas is attractive because it is known to reduce multi-path interferences and allows for flexible alignments between the transmitter and receiver antennas [1, 2]. Dual circularly polarized (DCP) antennas can send and receive signals with left-hand circular polarization (LHCP) and right-hand circular polarization (RHCP) simultaneously. For line-of-sight communications it has been reported that antennas with circular polarization diversity can enhance channel capacity [2].

Dual-circularly polarized antennas usually consist of a radiating structure and a feed network capable of generating the  $\pm 90^\circ$  modes required for dual circular polarization. The problem is that these feed networks can take up a large amount of space. Even if the network was designed to be compact the placement of the network can increase the overall size of the antenna. Only a few DCP antennas have been reported in literature [2 – 10]. These antennas have been shown to either have low front-to-back ratios, low cross-pol discriminations or they are large in terms of overall size.

Body area networks (BAN) have been gaining increasing research interest over the years; this is because these networks are used in a variety of applications such as: wearable computing, battlefield survival, health monitoring and patient tracking [11]. The antennas used in these applications needs to be compact, lightweight and due to their close proximity to the human body they are often required to have low back radiation emissions [11].

Slot antennas are often used for portable units and unobtrusive base stations of mobile communication systems, and it is often required that the antennas be small and low profile [12]. Slot antennas are also known to have a bi-directional radiation pattern, which is not practical for such applications [12]. A variety of techniques are available to achieve uni-directional radiation of a printed slot radiator [12 - 25]. One such method is to place an

electric conducting reflector below the slot. The typical distance to place such an electric reflector is a quarter of a wavelength [13, 14], resulting in antennas that have quite substantial heights. It is possible to use a smaller spacing between the antenna and electric ground plane, but impedance matching of the antenna may become a problem if the distance between the antenna and the reflector becomes too small.

In order to reduce the profile of the slot radiator, the authors in [15 - 17] used a closely spaced electric ground plane with a series of shorting posts between the conducting layer of the slot and the ground plane. Another method involves placing a thin metal cavity behind the slot radiator [18 - 20]. Both these types of implementations achieved a fairly low front-to-back ratios (no better than 15 dB), which makes these types of slot antennas undesirable for many applications.

A more attractive solution is to use a meta-material based reflector behind the slot [12, 21 - 25]. These types of reflectors can be placed much closer than a quarter of a wavelength and can also be used to reduce the surface wave propagation on the reflector; which can drastically increase the front-to-back ratio [26].

## **1.2 RESEARCH OBJECTIVE AND QUESTIONS**

The main objective of the research was to investigate the ring-slot antenna geometry as a potential candidate of the further development of dual circularly-polarized antennas. The research aimed to design, analyze, and formulate a design procedure for a compact dual-circularly polarized ring-slot antenna that has good unidirectional radiation properties. The proposed antenna should be designed to be manufactured using simple photolithography technology and operate in the 2.4 GHz WLAN band. The following research questions have been proposed:

- What dual-circularly polarized antennas are available in literature?
- What types of meta-material based reflectors are available in literature and how can they be used to improve the radiation characteristics of an antenna?
- Is the ring-slot geometry a suitable candidate for this type of problem?

### 1.3 RESEARCH CONTRIBUTION

The proposed antenna is a novel extension of the single polarized antennas proposed in [23, 27] to obtain a dual-circularly polarized ring-slot radiator backed by an AMC reflector. The structure of the AMC reflector consists of a  $2 \times 2$  patch array. The patch structure was chosen because it is known to be polarization invariant [28]. The two capacitive feeds are connected to a branch-line coupler in order to produce dual-circular polarization.

The reduced size branch-line coupler proposed by Joubert et al. [29] was used and placed over the center conductor of the ring-slot and was fed with two coaxial lines through the back of the cavity. This means that dual-circular polarization could be achieved without increasing the overall size of the antenna. The antenna matching was achieved using a capacitive feed network as proposed in [30].

Several simulation studies were performed in order to formulate a simple design procedure and to get an intuitive understanding of how the proposed antenna works. CST Microwave Studio<sup>TM</sup> was used to perform these simulations [31].

As a first prototype a CPW ring-slot radiator with a linear polarization with an AMC reflector was also analyzed and manufactured. This prototype used a capacitive feed structure similar to that used in [27]. This antenna arrangement was investigated in order to show that the ring-slot geometry is an ideal basis for the further development of compact antennas with dual-polarization sense. The investigation also shows the advantages of using a coaxial back-fed structure as opposed to a side-fed CPW structure.

The end result and contribution of the research presented in this work is a very low profile and small footprint antenna with reasonable gain and bandwidth, with two ports for dual-circular polarization operation, and very good front-to-back ratio and cross-polarization. To the author's knowledge this is the smallest antenna published up to date that has a suitable bandwidth for use in 2.4 GHz wireless local area network (WLAN) communication systems. The proposed antenna is also the first dual-circularly polarized antenna for which a

metamaterial reflector has been used to achieve a compact and unidirectional antenna. The new antenna has a smaller footprint than most previously published dual-polarized antennas [2-9], and a better front-to-back ratio than any of the previously published works [2-10].

#### **1.4 OVERVIEW OF STUDY**

In Chapter 2 a literature study is presented which relates to various aspects of the proposed antenna designs. Metamaterial reflectors and various antenna geometries were investigated. The literature study also shows that ring-slot antennas are versatile structures which can be implemented to have both frequency and polarization diversity. Various dual-circularly polarized antennas are compared in terms of size and performance. The literature study concludes by giving background knowledge and possible benefits of the proposed dual-circularly polarized antenna design.

In Chapter 3 a simulation study is presented to investigate various aspects relating to the design of a dual-circularly polarized ring-slot antenna loaded with an AMC reflector. This investigation was performed through various CST simulations. Both CPW and microstrip feeding structures were investigated. A dual capacitive feed configuration with polarization diversity was also investigated, as well as an analysis on a square patch AMC reflector. The rest of the Chapter focuses on the design of two ring-slot antennas loaded with AMC reflectors, the first of which is a capacitively-fed CPW ring-slot antenna and the second a dual-circularly polarized ring-slot antenna.

Chapter 4 presents results for two prototypes of ring-slot antennas loaded with AMC reflectors. The Chapter shows how the measurements were performed and how the measured data was processed. The measured results are shown to be in good agreement with the simulated results.

Chapter 5 concludes this thesis by giving an overview of what was achieved by this work. A full comparison of results achieved by this and previous work is presented. Future improvements and possible applications are also discussed.

# CHAPTER 2 LITERATURE STUDY

## 2.1 CHAPTER OBJECTIVES

This chapter will review the literature available that deals with the various aspects related to the design of a compact dual-circularly polarized antenna with uni-directional properties. In Section 2.2 of this study, background knowledge on metamaterial reflectors is given. This section also discusses the different types of metamaterial reflectors found in literature. Section 2.3 investigates various kinds of compact antennas found in literature, and how these antennas could potentially be used to implement a dual-circularly polarized antenna. This section also discusses how antennas with AMC reflectors have been implemented in previous research. In Section 2.4 different types of slot antennas are investigated. In this section the various feeding mechanism of the ring-slot geometry is also discussed. In Section 2.5 results of dual-circularly polarized antennas found in literature are discussed and compared. This chapter concludes by giving background knowledge on the proposed dual-circularly polarized antenna.

## 2.2 METAMATERIAL BASED REFLECTORS

### 2.2.1 Advantages of using a metamaterial surface reflector

Flat metal reflectors are often used to achieve uni-directional radiation properties from bi-directional or omni-directional antennas. The presence of the conductor can improve the antenna gain by redirecting the energy in the back lobe into a forward direction, which is known to increase the gain by 3 dB [23]. When a perfect electric conductor (PEC) reflector is placed in close proximity to a radiator, the image currents of the antenna tends to cancel out, resulting in degraded radiation patterns [26]. This is because a PEC reflector has a reflection phase of  $180^\circ$ . Another disadvantage of using a closely spaced metal reflector is that it makes impedance matching only possible over a narrow bandwidth [28]. In order to avoid these problems metal reflectors are typically placed a  $\lambda/4$  away from the radiator, resulting in an antenna with a substantial height [13, 14].

A perfect magnetic conductor (PMC) has a reflection phase of  $0^\circ$  which allows for in-phase reflection when placed in close proximity to a radiator, without severe impedance matching degradation [28]. Both PMC and PEC reflectors supports a parallel-plate mode that is also excited in the region between the radiator and the closely spaced reflector, which causes an increase in stored electromagnetic energy and results in a reduced radiation efficiency [23, 28]. They also support surface waves, which will propagate until they reach a discontinuity like an edge or a corner at which point these waves scatter into free space, which often results in a significant ripple in the radiation pattern [26].

In the work done by Vallecchi et al. [32], a simulation study was performed comparing the directivities and input impedances of a planar dipole on top of PEC and a PMC reflector at various spacing distances. When a small spacing between the reflectors and the dipole was used, it was found that for the PEC case the directivity was significantly higher, while for the PMC case had a better return loss. They investigated a third case where a dipole was placed on top of a metamaterial based reflector in close proximity. It was found that the metamaterial based reflector case combined the advantages of both PEC and PMC ground planes [32]. This case achieved a higher forward directivity than the PEC case and a better impedance bandwidth than the PMC case [32].

### **2.2.2 Fundamental concepts of metamaterial surfaces**

The term metamaterial is often used to describe a material that is artificially engineered to have unique or unusual electromagnetic properties [33, 34]. Electromagnetic bandgap (EBG) metamaterials has the property of exhibiting a stopband (over a limited frequency band) where surface waves cannot propagate and antenna radiation efficiency is improved [23, 34]. The most common terms used to describe metamaterial reflectors in literature are: high impedance surfaces (HIS), artificial magnetic conductors (AMC) and reactive impedance surfaces (RIS) [32, 34]. Note that these terms often describe similar types of structures and are often used interchangeably. Metamaterial surfaces have also been reported in multiband and ultra-wideband (UWB) applications [25, 35]. The term frequency selective surfaces (FSS) are also commonly used to describe some these types of metamaterial surfaces [25,

35]. These structures are known to be large, and the area of each unit cell has to be increased dramatically for each band that is added.

The structure of a single layer metamaterial reflector usually consists of a repeating pattern (unit cell) etched on top of a substrate and a ground plane at the bottom of the structure. In many cases, a via connecting each unit cell to the ground plane is added [36]. An EBG surface has a reflection phase that varies continuously from  $+180^\circ$  to  $-180^\circ$  as a function of frequency. The region from  $< 180^\circ$  to  $> 0^\circ$  is known as the inductive region, and the  $< 0^\circ$  to  $> -180^\circ$  region is known as the capacitive region. At the  $0^\circ$  reflection phase point ( $\omega_0$ ) the surface impedance is very high and behaves like a PMC, whereas when the phase tends asymptotically towards  $\pm 180^\circ$  it has a very low impedance and behaves like a PEC [32, 37]. AMC reflectors are usually designed to operate near the  $0^\circ$  region, since in this region the front-to-back ratio will be at its highest. When a AMC reflector is designed to operate in the  $90^\circ \pm 45^\circ$  inductive region, it can be shown to enhance the operating bandwidth of the EBG surface, although operating in this region is known to cause pattern degradation in some cases [28, 32].

The fundamental concepts of how AMC reflectors work were summarized by Sievenpiper et al. [26]. This work proposed the popular “mushroom” structure which consist of conductive square or honeycomb shaped patches with vias connecting the unit cells to the ground plane. According to this work the operation of an AMC reflector is similar to that of a corrugated metal slab commonly used in corrugated waveguide antennas [26]. A flat conducting metal sheet has a very low surface impedance. When closely spaced  $\lambda/4$  slabs is added, the surface impedance is transformed to a high impedance. Similarly the “mushroom” structure transforms the low impedance of the ground plane into a high impedance, as shown in figure 2.1. The capacitance can be adjusted by changing the ratio of the patch size and the spacing between the patches. The inductance and the bandwidth of the surface impedance is increased by increasing the height of the structure. Equation (2.1) shows the relationship between the surface capacitance, inductance and the  $\pm 90^\circ$  reflection phase bandwidth. This arrangement allows the profile to be significantly smaller in profile than a wavelength [26].

Equation (2.1) also applies to AMC and RIS surfaces, although the inductance is modelled differently [28].

$$\frac{\Delta\omega}{\omega_0} = \frac{Z_0}{\eta_0}, \text{ where } \omega_0 = \frac{1}{\sqrt{LC}} \text{ and } Z_0 = \sqrt{L/C} \quad (2.1)$$

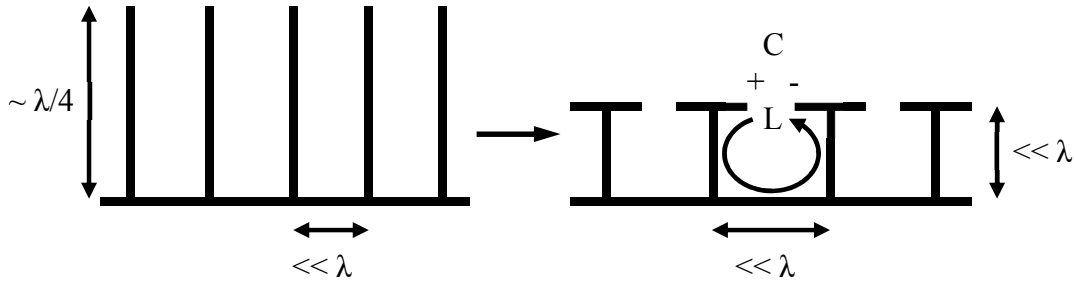


**Figure 2.1.** Transformation of the corrugated surface into a high impedance surface [23].

### 2.2.3 AMC geometries

This subsection will focus on investigating different AMC geometries found in literature. The authors Sohn et al. [37] performed a comparative study on four types of AMC surfaces namely: a uniplanar compact EBG (UC-EBG) [38], a first order Peano curve [39], a second order Hilbert curve [40], and a “mushroom” type AMC surface [26]. The UC-EBG and the Peano curve achieved a similar reflection phase bandwidth. The Hilbert curve achieved the lowest reflection phase bandwidth, although it also had the smallest unit cell size. Both the Hilbert and the Peano curve only have one axis of symmetry, which makes these structures undesirable for polarization diversity applications. The “mushroom” geometry was found to have the largest reflection phase bandwidth and the unit cell size was similar to that of the UC-EBG and the Peano curve EBG. It has been suggested that the presence of the vias could cause an additional ripple in the radiation pattern if the vias are not flush to the surface of the unit elements [32].

In [12] the authors did a simulation study comparing the “mushroom” with a patch AMC (without any vias) and found that the “mushroom” structure yielded a marginally better reflection phase bandwidth [12]. The authors also investigated the Jerusalem cross AMC

structure [41] and concluded that the reflection phase bandwidth was substantially less than the patch AMC [12]. In [42] the authors presented results of a UWB circularly polarized antenna on top of dual-layer AMC surface. Both layers of the AMC consisted of periodic patches. A single layer patch AMC was also designed and the results of the antenna on both types of AMC structures were compared and it was found that the dual-layer structure achieved a marginally improved impedance bandwidth.

Baracco et al. [43] proposed a spiral AMC surface. This is an interesting geometry because it is one of a few AMC geometries which is asymmetrical, and which is suitable for use as a reflector for an antenna with circular polarization. Due to the asymmetry of the structure, it is suspected that this type of geometry will not be suited for dual-circularly polarized antennas.

A commonly used AMC surface is the “dog-bone” shaped geometry [11, 32]. This type of structure can be made significantly smaller in the direction orthogonal to the polarization sense (direction of the cross-polarization) than the patch structures discussed earlier, and can achieve a phase reflection bandwidth similar to that of the patch structure. This structure only has one axis of symmetry, which makes this type of AMC structure only suitable for single linearly polarized antennas.

### **2.3 COMPACT ANTENNAS AND DESIGN CONSIDERATIONS**

In this section various antennas are investigated that could potentially be used to implement a compact dual-circularly polarized antenna with a unidirectional radiation pattern. In the literature it was found that AMC reflectors were implemented on a vast array of printed radiators such as: curl antennas [43], dipoles [32], monopoles [11, 44], patch antennas [1, 28, 34, 45, 46], and slot antennas [12, 23, 25].

Curl antennas are often used in applications where circular polarization is required. This type of antenna is inherently circularly polarized which means that it only requires a simple feed network in order to produce a circular polarization sense [43]. In order to have dual-circular polarization, two curl antennas with opposite polarization sense would be required,

which would increase the overall size without increasing the gain, since only one of the antenna elements can be excited at a given time. This makes the use of curl antennas undesirable for use in circular polarization diversity applications.

Vallechi et al. [32] proposed a fully planar folded dipole placed on top of a “dog bone” shaped AMC reflector. The dipole used in this work was very compact, having an overall lateral size of only  $0.3\lambda_0 \times 0.054\lambda_0$ . The problem with dipole antennas in general, is that they often require a balun (balanced to unbalanced transformer) in order to function properly, since dipoles are balanced structures and feeding structures like coaxial cables and microstrip transmission lines are unbalanced structures [32]. These balun structures can take up a significant amount of space. For the case of the work in [32], the balun transformer had overall size larger than that of the dipole.

Jiang et al. [11] published results for a very compact printed monopole radiating above a “dog bone” shaped AMC. The final dimensions of this antenna were  $0.5\lambda_0 \times 0.3\lambda_0 \times 0.028\lambda_0$ . It achieved a -10 dB input reflection bandwidth of 5.5%, maximum gain of 6.2 dBi, and front-to-back ratio of 25 dB and cross-polarization discrimination better than 20 dB. What is interesting from these results is that the AMC structure only consisted of four unit elements, and still managed to achieve good results. McKinzie et al. [44] proposed a dual linear antenna consisting of two orthogonally overlapping bent wire monopoles placed on top of an AMC reflector. The final dimensions of this antenna were  $0.3\lambda_0 \times 0.3\lambda_0 \times 0.02\lambda_0$  and achieved an isolation of 25 dB over the impedance bandwidth of 2.6%. This implementation only achieved a maximum gain of 3 dBi with a front-to-back ratio of only 7 dB, although it is suspected that this pattern degradation is caused by the fact that the monopoles were placed too close to the AMC reflector.

Patch antennas can also benefit from being implemented with AMC reflectors. This is usually done by placing the unit cell elements in between the ground plane and the patch [1, 28, 34, 45, 46]. Ren et al. [46] did a simulation study using a patch antenna on top of an AMC structure with various lateral sizes and number of unit elements. It was found that the bandwidth increases as the number of elements increases. When the lateral size of the AMC

reflector was increased, it was found that the bandwidth only increased up to an optimal point and then decreased as the size continues to increase. These results show that when considering the bandwidth of the antenna with loaded with an AMC reflector, it is important to consider the overall dimensions of the AMC structure as well as the unit cell dimensions. The end result of this research was a patch antenna on top of an AMC consisting of a  $4 \times 4$  patch array, with the height of the AMC substrate being  $0.05\lambda_0$ . The structure has overall dimensions of  $0.833\lambda_0 \times 0.833\lambda_0 \times 0.0625\lambda_0$ , and operated from 2.4 GHz to 2.6 GHz with a return loss better than 10 dB. This implementation achieved a gain and front to back ratio of 4.2 dBi and 15 dB respectively.

## 2.4 SLOT ANTENNAS

### 2.4.1 Different types of slot antennas found in literature

A slot radiator above an AMC reflector is often regarded as an open cavity problem, where the objective is to minimize the radiation leakage from the open sides of the cavity [12]. Joubert et al. [12] showed that the energy leakage from the open cavity can be minimized if the cavity dimensions (the upper and lower cavity surfaces are respectively the AMC reflector ground plane and the slot radiator ground plane) are optimized [12]. It was found that when the cavity dimensions are chosen incorrectly a significant portion of the energy can radiate outwards from the cavity's open walls. This work also presented results of a CPW-fed rectangular slot radiator backed by an AMC reflector. The final dimensions of the slot radiator were  $1.02\lambda_0 \times 0.82\lambda_0 \times 0.063\lambda_0$ . This antenna achieved a 5% impedance bandwidth, low cross-polarization, and a front-to-back ratio of 25 dB.

Various other slot geometries were found in literature such as the square slot antenna [47], rhombus shaped slot antennas [48], the stair-shaped slot antenna [49], and the ring-slot geometry [15, 24, 27, 50 - 53]. Chen et al. [47] proposed a UWB square slot antenna fed with an offset patch feed structure. This implementation achieved an impedance bandwidth of 124% and had an overall lateral size of  $1.55\lambda_0 \times 1.55\lambda_0$ , which is fairly compact when considering the large operating bandwidth. The results from this work show some pattern breakup and a very low cross-polarization discrimination (close to 0 dB) in various

frequency regions within the band. Lin et al. [48] proposed a CPW-fed multiband rhombus shaped slot antenna, which operated in the 2.4/5.2/5.8-GHz WLAN bands. From the results it is clear that this implementation achieved very low cross-polarization discrimination. Wang et al. [49] proposed a compact circularly polarized stair shaped slot antenna. This implementation had an overall lateral size of  $0.545\lambda_0 \times 0.363\lambda_0$ , and achieved a 3 dB axial ratio bandwidth better than 31%. This antenna also achieved reasonable radiation patterns and good cross-polarization discrimination.

#### 2.4.2 Ring-slot antennas found in literature

The ring-slot or annular slot antennas are known to have a compact structure and is often used in aircraft and spacecraft applications [54]. Ring-slot antennas are versatile structures and can be designed to have frequency and polarization diversity [14, 27, 50, 52].

Several methods exist to produce circular polarization in a ring-slot antenna. One such method involves breaking the symmetry of the ring-slot in order to produce two orthogonal modes [24, 51]. Another commonly used method involves the use of an L- or a V-shaped feed structure [15, 50]. The use of a splitter network where the outputs are  $90^\circ$  out of phase have also been shown to be a good way to produce circular polarization in ring-slot antennas [14].

Ring-slot antennas usually have relatively narrow impedance bandwidths [19], although several methods exist that can significantly increase the bandwidth. Elek et al. [23] showed that the bandwidth of a CPW-fed ring-slot can be improved by the use of a quarter-wave impedance transformer, although this is an undesirable feed structure since it increases the size of the structure significantly. A capacitive coupled feed structure is a more compact solution to this problem. Sim et al. [27] published results of a dual-band CPW-fed ring-slot antenna with a capacitively coupled feed. The results show a -10 dB input reflection bandwidth which covers a frequency range 1.97 GHz to 4.25 GHz (73.3%) and 4.92 GHz to 5.93 GHz (18.6%). In the first frequency band a peak gain of 5 dBi was measured and a cross-polarization discrimination of better than 10 dB. In the second band the co-polarization radiation patterns exhibit deep nulls and a cross-polarization discrimination close to 0 dB.

The overall lateral size of the antenna was  $0.52\lambda_0 \times 0.52\lambda_0$  at the center frequency of the first band (3.11 GHz). Gallo et al. [52] published results of capacitively-fed dual-linear UWB ring-slot antenna shorted at two points. The results show a return loss and isolation of 10 dB and 15 dB respectively over a bandwidth 120%. The overall lateral size of the antenna was  $0.5\lambda_0 \times 0.5\lambda_0$ . When comparing the result from the ring-slot antennas in [27] and [52] to the CPW-fed ring in [23], it is clear that a capacitively coupled ring-slot antennas are advantageous in terms of bandwidth and overall size.

## 2.5 ANTENNAS WITH DUAL-CIRCULAR POLARIZATION

### 2.5.1 Dual-circularly polarized antennas in literature

Dual-circularly polarized antennas are usually implemented in a single or dual feed configuration. An example of a single feed dual-circularly polarized antenna is when a slot antenna without a reflector is circularly polarized, the top beam would have the opposite circular polarization sense than the bottom part of the beam [15, 49]. This is undesirable since the antenna needs to be turned  $180^\circ$  in order to change polarization sense. Another type of single feed dual-circularly polarized antennas is when a dual-band antenna is designed to have different circular polarization senses in each of the bands. This type of configuration is commonly used in RFID applications [55]. In order to have single feed dual-circular polarization over the same bandwidth and in the same direction, PIN diodes or RF-MEMS switches are required, which can significantly increase manufacturing costs [3]. The work by Row et al. [50] showed that a ring-slot antenna with an “arrow” shaped feed and three pin-diodes could switch between RHC, LHC and a single linear polarization depending on the state of the diodes.

In order to implement dual-circular polarization over the same bandwidth and in the same direction, a dual feed configuration is needed. Microwave components such as circulators, and directional couplers are often used to generate dual-circular polarization [5]. These components are convenient since they are known to have a high isolation [5]. Dual-circular polarization is often attained by feeding a dual-linear antenna with a  $90^\circ$  hybrid coupler [3, 5, 9]. Depending on the excitation port this directional coupler can produce outputs that are

either plus or minus  $90^\circ$  out of phase, which in turn can then either produce a RHC or LHC polarization [3].

Hong et al. [9] proposed a dual-circularly polarized microstrip cogwheel shaped annular ring antenna. A planar reflector was placed underneath the antenna structure at a distance of approximately  $\lambda/4$ . Three-wire transmission lines were used to feed the antenna at two points, and a  $90^\circ$  hybrid coupler was used to produce the dual-circular polarization. The overall size of the antenna was  $0.85\lambda_0 \times 0.85\lambda_0 \times 0.28\lambda_0$ , and the results shows an effective bandwidth of larger than 8.5 %, where the effective bandwidth is defined as the frequency region where the axial ratio is better than 3 dB and the return loss and isolation are greater than 10 dB. Lai et al. [5] presented results for a dual-circularly polarized patch antenna fed by two H-shaped slots and a  $90^\circ$  hybrid coupler. The overall size of the antenna was  $0.73\lambda_0 \times 0.73\lambda_0 \times 0.067\lambda_0$ . The results show an effective bandwidth of 16%, a front-to-back ratio of 11 dB, and a cross-polarization discrimination of 16 dB. When looking at the feeding structures of these two antennas, it is clear that the hybrid coupler can take up a significant amount of space. In order to make antennas more compact, couplers with varactor diodes are often used [3].

For patch antennas many other feeding structures can be used to produce dual-circular polarization [2, 3, 7, 10]. Wu et al. [2] proposed a dual-circularly polarized patch antenna that is fed with a suspended L-shaped lines, which was located in between the patch and the ground plane. The suspended line is connected to the patch by three probe feeds, where two of the probes were placed near the ends of the L-shaped line, and one probe was placed in the corner of the L-shaped line. The suspended line structure was connected to the LHCP and RHCP feed connectors via two probe feeds at the ends of the L-shaped line. The overall size of the antenna was  $0.8\lambda_0 \times 0.8\lambda_0 \times 0.125\lambda_0$ . The results show an effective bandwidth of 12%, a cross-polarization discrimination of 10 dB, and a fairly good front-to-back ratio of 15 dB.

Narbowics et al. [3] proposed a dual-circularly polarized patch antenna that has a feed network that uses even and odd mode excitations of a CPW transmission line in order to

generate dual-circular polarization. The even mode was excited by a CPW line that splits off into two slot lines, where one of the slot lines are  $90^\circ$  longer than the other. These lines in turn feed the patch antenna orthogonally. The odd mode was excited through a microstrip feed that crosses the CPW line orthogonally and is then terminated in a radial stub, causing a microstrip to CPW transition. This is a novel method to generate dual-circular polarization, although the problem with this implementation is that there is a significant difference between the gain achieved for the LHC excitation (even mode) and RHC excitation (odd mode). The realized circular gains for the LHC- and RHC excitation were 7.23 dBic and 5.77 dBic respectively. The overall size of the antenna was  $0.8\lambda_0 \times 0.8\lambda_0 \times 0.125\lambda_0$ . The results show an effective bandwidth of 12%, a cross-polarization discrimination of 10 dB, and a fairly good front-to-back ratio of 15 dB.

The authors in [7] published results for a dual-circularly polarized patch antenna that is implemented with a microstrip ring feed network. The microstrip ring structure was placed behind the ground plane of the patch antenna and travelled, radially through four cross slots, which was used to couple to the patch radiator. In order to decrease backwards radiation a metal cavity was placed behind the cross-slots. The ports were placed on either side of the microstrip ring structure, in order to excite the LHC and RHC polarizations. The overall size of the antenna was  $0.94\lambda_0 \times 0.94\lambda_0 \times 0.189\lambda_0$ . The results show an effective bandwidth of 16%, a cross-polarization discrimination of 17 dB, a front-to-back ratio of 13 dB, and a maximum gain of 9.8 dBic. A similar type of DCP patch antenna was proposed in [10]. The antenna in this work used a microstrip ring structure with two cross slots to feed a corner truncated patch with a square hole. The structure had a very compact overall size  $0.5\lambda_0 \times 0.5\lambda_0 \times 0.025\lambda_0$ . The results from this antenna showed an effective bandwidth of only 1%. The antenna also had a fairly good front-to-back ratio and cross polarization discrimination of better than 15 dB.

### 2.5.2 Proposed dual-circularly polarized ring-slot antenna

A compact dual-circularly polarized antenna with uni-directional properties should have the following properties: a high impedance bandwidth, high isolation between the feeding ports,

radiations patterns with high front-to-back ratios, and a high cross-polarization discrimination. By examining the results from previous dual-circularly polarized antennas (as discussed in Section 2.5.1), it was found that these antennas either have low front-to-back ratios, low cross-polarization discriminations or they are large in terms of overall size.

The ring-slot geometry (discussed in Section 2.4.2) was found to be a suitable candidate for this problem since it is known to be compact and can achieve a fairly high impedance bandwidth when a capacitive feed structure is used [27, 30, 52]. The proposed antenna consists of a ring-slot antenna where two capacitive feeds are connected to a branch-line coupler in order to produce dual-circular polarization, backed by an AMC reflector. The structure of the AMC reflector consists of a  $2 \times 2$  single layer patch array. The patch structure was chosen because it is known to be polarization invariant [28].

The reduced size branch-line coupler proposed by Joubert et al. [29] was used and placed over the center conductor of the ring-slot and was fed with two coaxial lines through the back of the cavity. To the best of the author's knowledge, this type of feeding arrangement has not been implemented in this way in any previous publications. The advantage of using this type of feeding structure is that dual-circular polarization could be achieved without increasing the overall size of the antenna. The new antenna has a smaller footprint than most previously published dual-polarized antennas [2-9], and a better front-to-back ratio than any of the previously published works [2-10].

# CHAPTER 3 SIMULATION STUDY

## 3.1 CHAPTER OBJECTIVES

This chapter aims to investigate various aspects relating to the design of a dual-circularly polarized cavity-backed ring-slot antenna loaded with an AMC reflector. This investigation was performed through various CST simulations.

In Section 3.2 several CPW-fed ring-slot antennas are analyzed. The purpose of this simulation study was to determine what influence the parameters of the ring-slot has on the input impedance and radiation characteristics. This section aims to show how the addition of a capacitive feed network can improve the impedance bandwidth without increasing the overall size of the antenna.

In Section 3.3 ring-slot antennas with microstrip capacitive feeds are analyzed. The parameters of the capacitive network was categorized to show how this feeding mechanism differs from the CPW case. A dual-feed configuration was also investigated in order to show how well it works as a polarization diverse antenna.

In Section 3.4 the square patch AMC reflector was analyzed using both CST simulations and the theory described in [26, 28]. This section also includes the design and simulation results of a capacitively-fed CPW ring-slot antenna loaded with an AMC reflector.

In Section 3.5 the design and simulation results of a dual-circularly polarized cavity-backed ring-slot antenna loaded with an AMC reflector is presented.

## 3.2 CPW-FED RING-SLOT ANTENNAS

### 3.2.1 Simulation study of a CPW-fed ring-slot antenna

Simulation results for a CPW-fed ring-slot antenna are presented in this section. The structure is similar to that of the work in [23, 53], and consists of circular slot cut out of a planar conducting plane and placed on top of a substrate, as shown in Figure 3.1. The

structure was fed with a  $\sim 50 \Omega$  CPW transmission line, where the width of the center line and gap size were 3 mm and 0.25 mm, respectively. The slot length  $l$  is defined as the circumference along the center of the slot, and should be approximately equal to a wavelength.

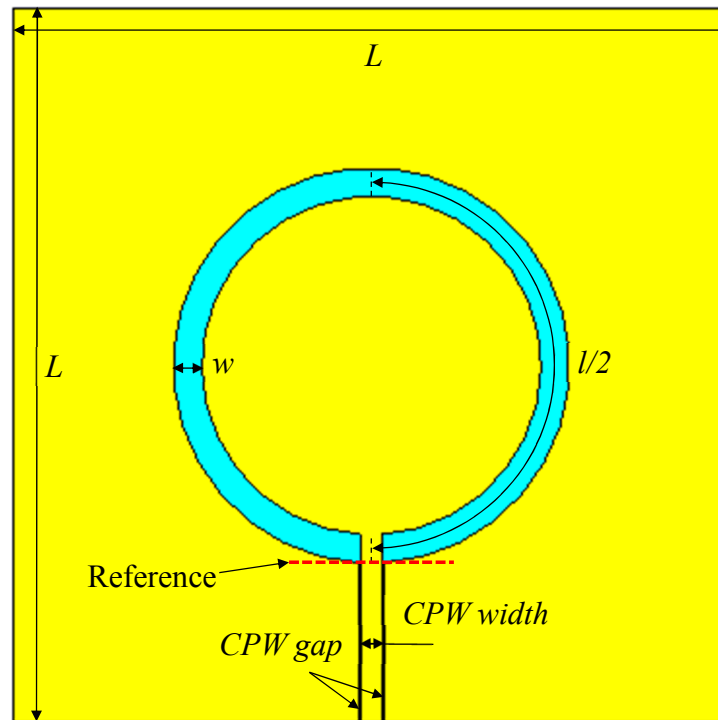


**Figure 3.1.** CPW-fed ring-slot antenna.

The purpose of this simulation study was to determine what effect that the slot width  $w$  and slot length  $l$  have on the input impedance. This experiment also investigated the effect that the ground plane size  $L$  has on the overall performance of the antenna. The simulations were performed using CST Microwave Studio<sup>TM</sup> [31]. Due to the narrow band nature of the simulation study, the “Frequency domain solver” was used for all the simulations in this chapter [31]. To increase the accuracy of the simulations, adaptive meshing was applied at the center frequency (2.45 GHz).

The radiating slot element substrate was chosen as Rogers RO4003, with  $\epsilon_r = 3.38$ ,  $\tan \delta = 0.0021$ , with a height of 0.813 mm. Note that the datasheet for Rogers RO4003 suggests that

relative permittivity  $\epsilon_r$  of 3.55 be used for electromagnetic computation, although this discrepancy is not sufficiently substantiated.

A waveguide port was used to excite the CPW line, and a reference plane was added at the end of the CPW line, as shown in Figure 3.1. For this study the ground plane size  $L$  was chosen as 100 mm. The antenna was matched to  $50 \Omega$  at 2.45 GHz by adjusting the slot width to 4 mm and a slot length to 161.8 mm. Figures 3.2 and 3.3 illustrates how impedance matching of a ring-slot antenna can be achieved, by adjusting one parameter at a time. For the cases where the slot width is adjusted while the slot length was kept constant, the shape of the curve becomes less pronounced as the slot width is increased, as shown in Figure 3.2. The results in Figure 3.3 shows that the reactance becomes higher (more inductive) as the slot width is increased. For the cases where the slot length is adjusted while the slot width is kept constant, both the input resistance and reactance shifted in frequency. Figures 3.4 and 3.5 shows how the impedance changes at 2.45 GHz as the parameters  $w$ ,  $l$  is adjusted, respectively.

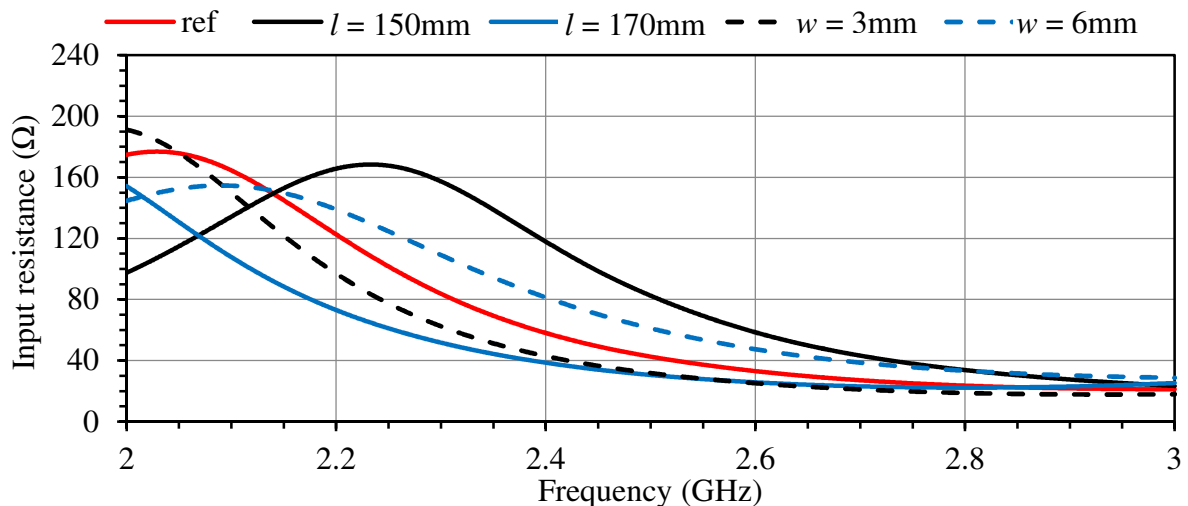


**Figure 3.2.** Input resistance over frequency, where one parameter was adjusted at a time from the reference case. The reference is the case where  $w = 4$  mm,  $l = 161.8$  mm.

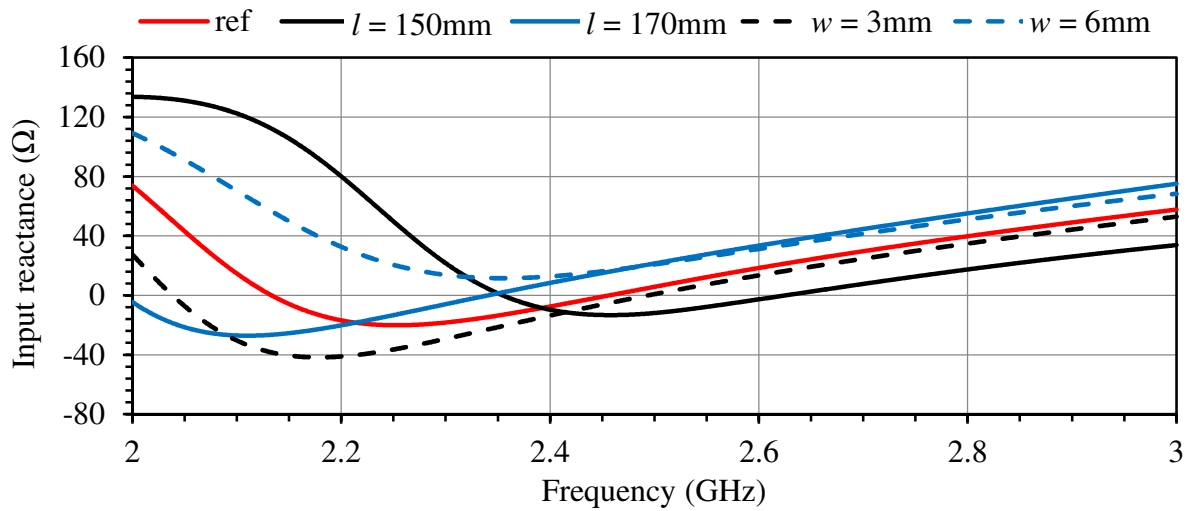


**Figure 3.3.** Input reactance over frequency, where one parameter was adjusted at a time from the reference case. The reference is the case where  $w = 4\text{ mm}$ ,  $l = 161.8\text{ mm}$ .

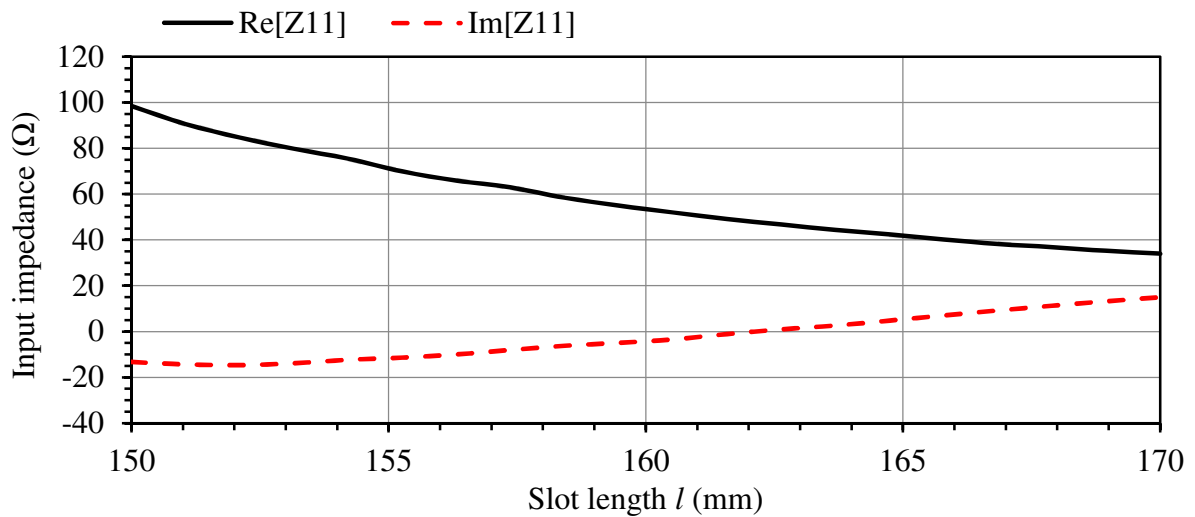


**Figure 3.4.** Input impedance over slot length  $l$  at 2.45 GHz, where  $w = 4\text{ mm}$ .

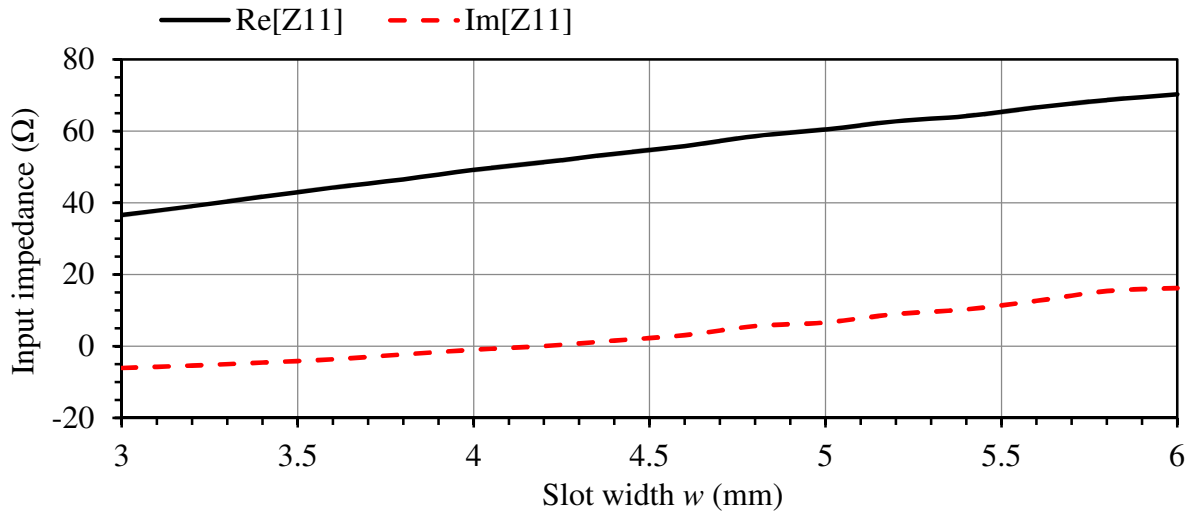


**Figure 3.5.** Input impedance over slot width  $w$  at 2.45 GHz, where  $l = 161.8$  mm.

The next part of this experiment was to determine how the performance of the antenna is affected if the ground plane size  $L$  is reduced. Figure 3.6 shows the return loss over frequency for several CPW-fed ring-slot antennas at various values of  $L$ . The slot width and slot width of each case was adjusted in order for the antenna to resonate at 2.45 GHz. Table 3.1 shows the value of the adjusted parameters, the maximum gain (dBi), and the cross-polarization discrimination (dB). From the results in Figure 3.6, an increase of the -10 dB input reflection bandwidth is noted as the ground plane size is decreased, which is most prominent in the low end of the band. A possible reason for this is that the loss of the antenna is increased as the ground plane size is reduced. Table 3.1 shows a decrease in gain and an increase in cross-polarization discrimination as the ground plane size is decreased. From these results it is clear that size of the ground plane needs to be carefully considered in order to achieve the desired characteristics.

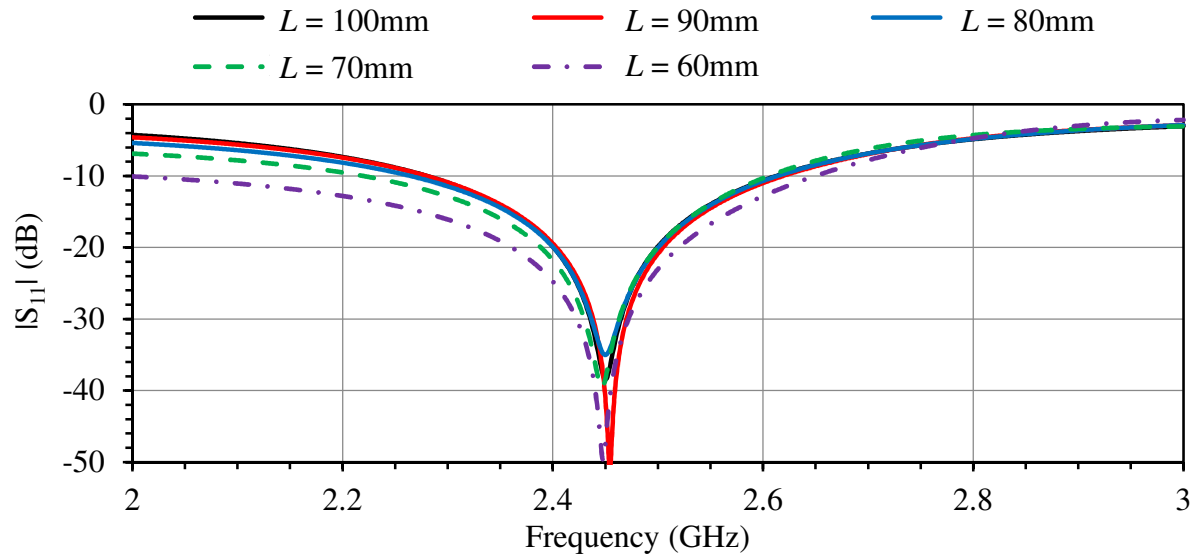


**Figure 3.6.** Amplitude of  $S_{11}$  over frequency, for CPW-fed ring-slot antennas designed at various ground plane sizes.

**Table 3.1.** Optimized parameters and summary of pattern data when parameter  $L$  is adjusted.

Chosen $L$ (mm)	Optimized slot width $w$ (mm)	Optimized slot length $l$ (mm)	Gain (dBi)	H-plane cross-pol. discrimination (dB)
60	3.5	154.2	4.05	17.83
70	4	158.8	4.40	11.84
80	4.1	159.9	4.57	8.56
90	4.1	161	4.73	6.82
100	4	161.2	4.98	5.98

### 3.2.2 Capacitively-fed CPW ring-slot antenna.

In this section results for a capacitively-fed CPW ring-slot antenna are presented. The structure is a simplified version of the antenna proposed in [27]. The feeding mechanism consists of a radial stub with a stub angle  $\theta$ , a stub width  $w_2$ , and separated from the center conductor at a distance  $d$ , as shown in Figure 3.7. The capacitive stub was fed with a  $\sim 50 \Omega$

CPW transmission line, with dimensions similar to that of the structure in Figure 3.1. The simulation setup was also similar to that of the previous section.

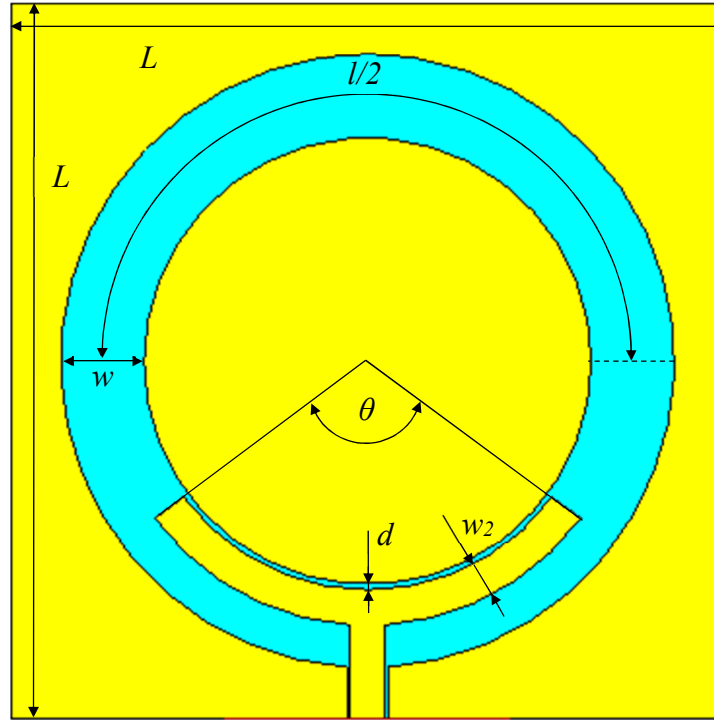


**Figure 3.7.** Capacitively-fed CPW ring-slot antenna.

The purpose of this simulation study was to characterize the effect that the feeding parameters ( $\theta$ ,  $w_2$ , and  $d$ ) has on the input impedance. For this study the ground plane size  $L$  was chosen as 60 mm. As a first step the antenna was matched to  $50 \Omega$  at 2.45 GHz. The slot width  $w$ , slot length  $l$ , and stub width  $w_2$  were chosen as 7 mm, 140 mm, and 3 mm respectively. The feed parameters  $\theta$  and  $d$  were then adjusted to  $107^\circ$  and 0.45 mm, respectively.

Figures 3.8 and 3.9 illustrates the effect on the input impedance by adjusting one of the feeding parameters at a time. For the cases where either the  $w_2$  or  $d$  were adjusted the input resistance either increased or decreased, while the input reactance remained fairly constant. On the other hand when  $\theta$  was adjusted the input reactance either increased or decreased, while the input resistance remained fairly constant. It is also important to note that these

reactive and resistive changes were fairly consistent over the frequency band, which is a convenient property for impedance matching. Figures 3.10 to 3.12 shows how the impedance changes at 2.45 GHz as the parameters  $\theta$ ,  $w_2$ , and  $d$  is adjusted. These results shown are consistent with the parametric results on capacitively-fed microstrip annular ring antennas in [30].

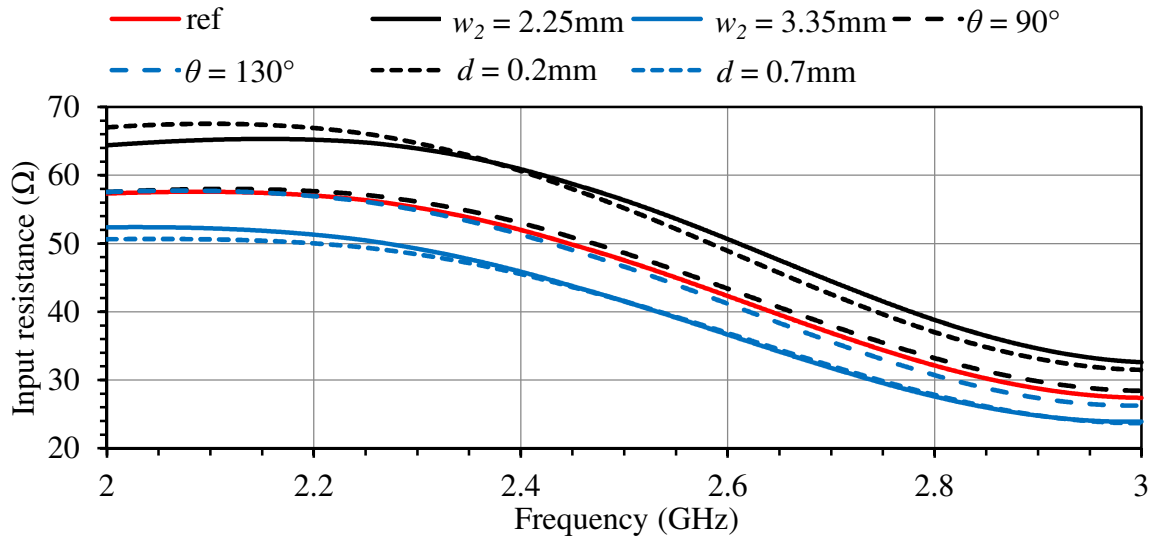


**Figure 3.8.** Input resistance over frequency, where one parameter was adjusted at a time from the reference case. The reference is the case where  $\theta = 107^\circ$ ,  $w_2 = 3$  mm, and  $d = 0.45$  mm.

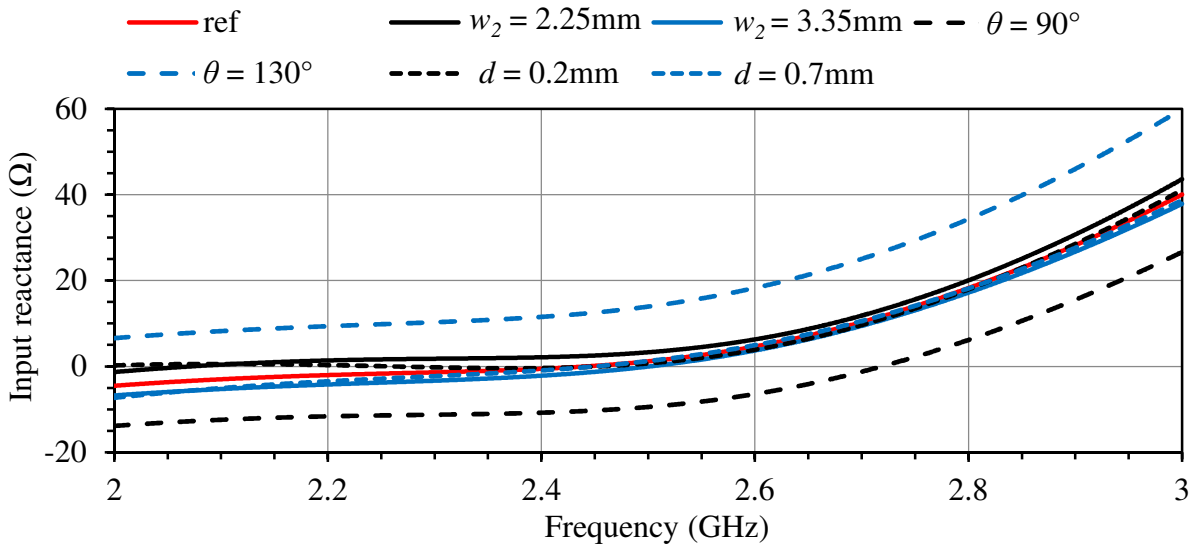


**Figure 3.9.** Input reactance over frequency, where one parameter was adjusted at a time from the reference case. The reference is the case where  $\theta = 107^\circ$ ,  $w_2 = 3$  mm, and  $d = 0.45$  mm.

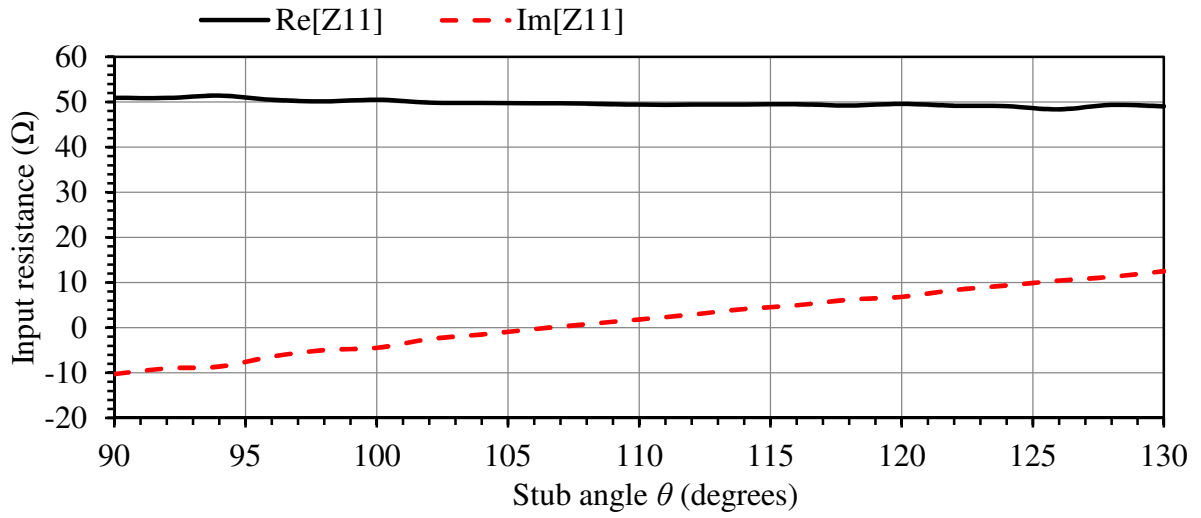


**Figure 3.10.** Input impedance over stub angle  $\theta$  at 2.45 GHz, where  $w_2 = 3$  mm and  $d = 0.45$  mm.

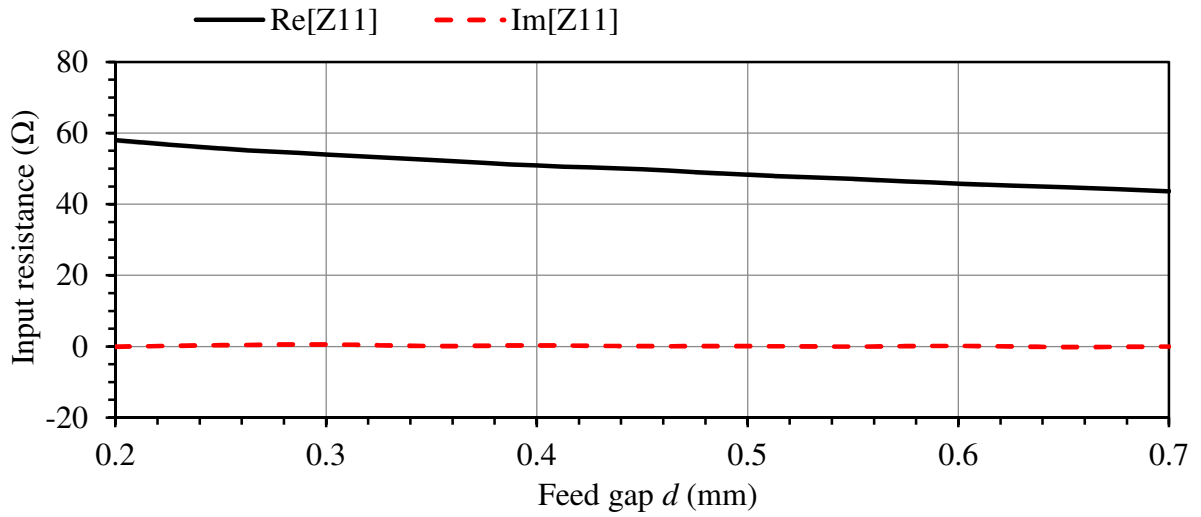


**Figure 3.11.** Input impedance over feed gap  $d$  at 2.45 GHz, where  $\theta = 107^\circ$  and  $w_2 = 3$  mm.

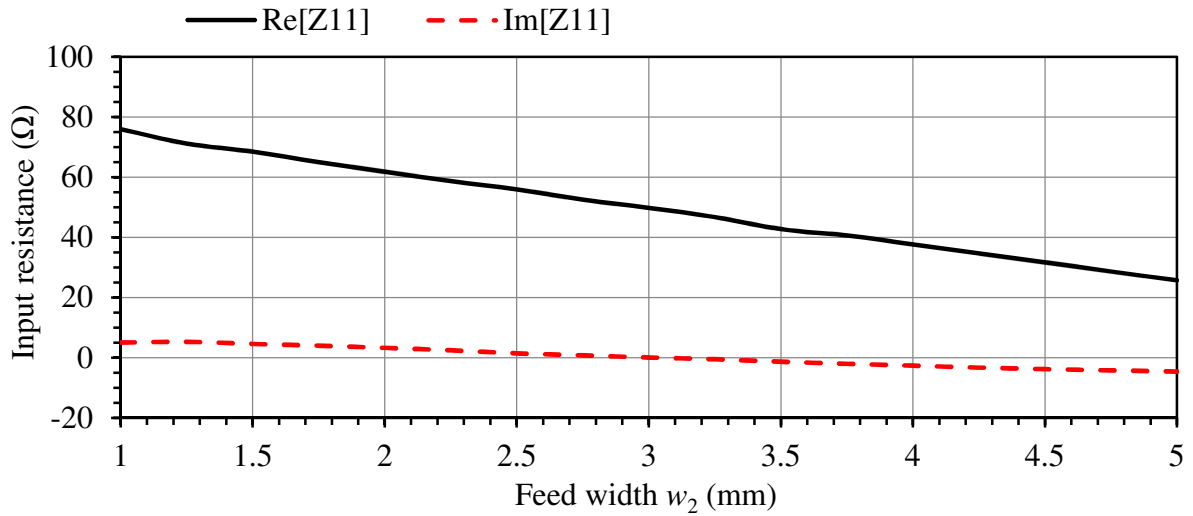


**Figure 3.12.** Input impedance over stub width  $w_2$  at 2.45 GHz,  $\theta = 107^\circ$  and  $d = 0.45$  mm.

The dimensions  $w$  and  $l$  were chosen as fixed values so far, so in this next study three different cases are investigated. This was done in order to see if the performance of the antenna changes drastically for different values of the slot dimensions. Figure 3.13 shows the return loss over frequency for three capacitively-fed ring-slot antennas. The stub angle  $\theta$  and the feed gap  $d$  of each case was adjusted, while the feed width  $w_2$  was kept at 3 mm. The goal of the optimization was to try and achieve a minimum return loss over the bandwidth of interest (2.4 GHz – 2.484 GHz). For the optimization in this chapter requiring two or less parameters to be adjusted, the “Trust region framework” optimization algorithm was used [31]. The “Nelder-Mead Simplex” algorithm was used to perform the optimization for the cases requiring more than two parameters to be adjusted [31].

Table 3.2 shows the value of the adjusted parameters, the maximum gain, and the H-plane cross-polarization achieved in each case. The case where  $w = 7$  mm and  $l = 130$  mm achieved the lowest return loss across the band of interest and the highest cross-polarization discrimination. The case where  $w = 10$  mm and  $l = 130$  mm achieved the highest maximum gain and the optimized value of  $\theta$  was significantly smaller than the other cases. This is a convenient property for an orthogonal dual feed case, where the feed stub angle must be less than  $90^\circ$ .

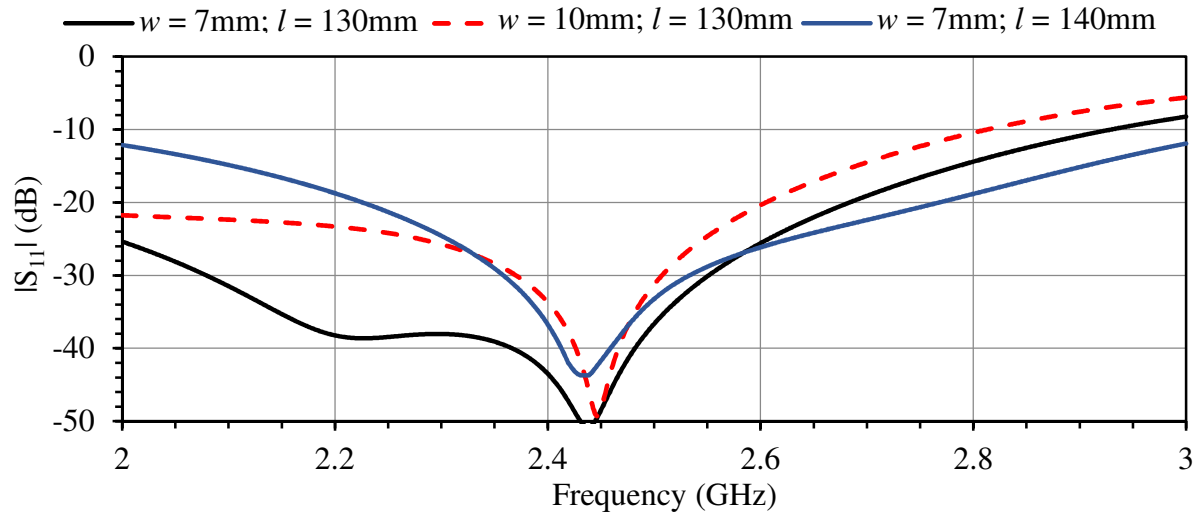


**Figure 3.13.** Amplitude of  $S_{11}$  over frequency, for three different design cases.

**Table 3.2.** Optimized parameters and summary of pattern data when parameter  $L$  is adjusted.

Chosen slot width $w$ (mm)	Chosen slot length $l$ (mm)	Optimized Feed stub angle $\theta$ (degrees)	Optimized Feed gap $d$ (mm)	Gain (dBi)	H-plane cross-pol. discrimination (dB)
7	130	110	1	4.05	21.7
7	140	107	0.45	4.40	20
10	130	83	1.7	4.57	19.32

Figure 3.14 shows the E-field distribution for the case where  $w = 7$  mm and  $l = 130$  mm. This figure illustrates the basic operation of a capacitively-fed ring-slot antenna. Since the structure is symmetrical in the E-plane, no significant cross-polarization component exists. In the H-plane however a cross-polarization component can exist, due to the asymmetry in this plane. Figure 3.15 shows the radiation patterns in the E-plane and H-plane. The E-plane pattern shows a null on the horizon, and no significant cross-polarization fields.

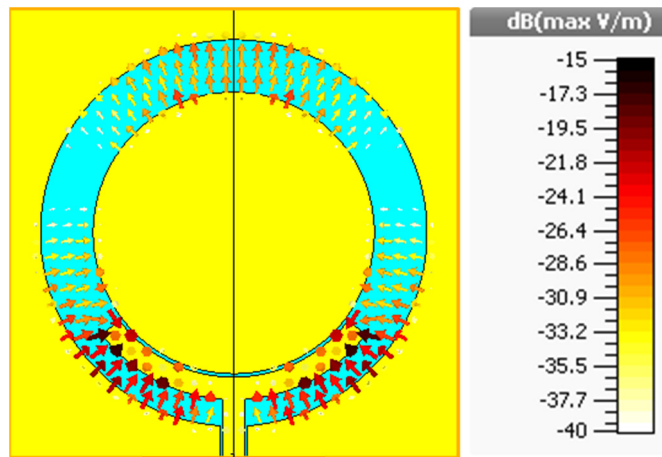


**Figure 3.14.** E-field distribution for the  $w = 7$  mm and  $l = 130$  mm case.

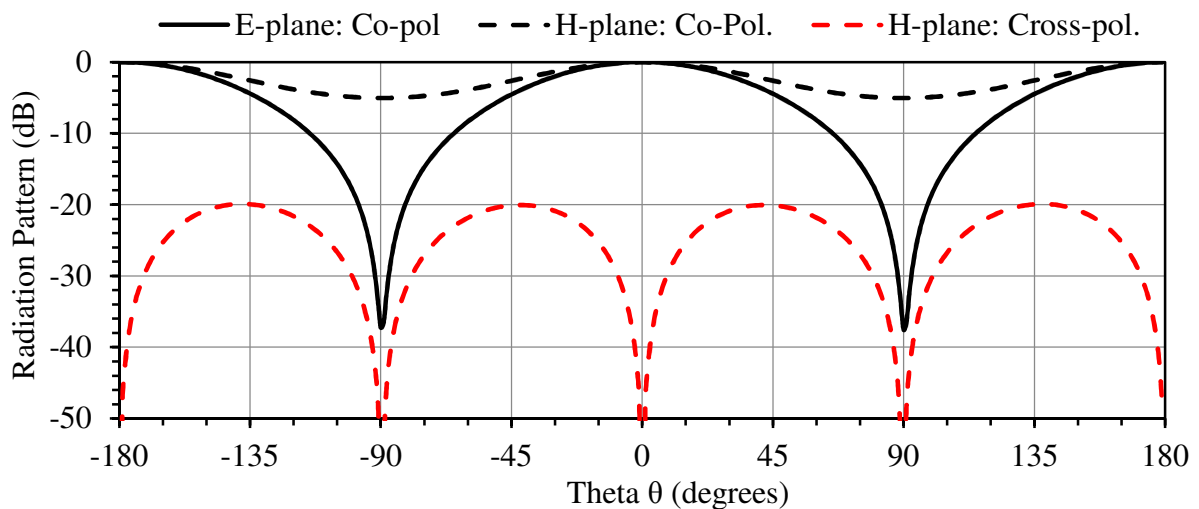


**Figure 3.15.** Radiation pattern in the E-plane and H-plane for the  $w = 7$  mm and  $l = 130$  mm case.

### 3.3 MICROSTRIP-FED RING-SLOT ANTENNAS

#### 3.3.1 Ring-slot antenna with a single center-fed microstrip capacitive feed.

Simulated results for a ring-slot antenna with a single center-fed microstrip capacitive feed are presented in this section. The structure is shown in Figure 3.16. The feed structure is similar in some respect to the outside-fed microstrip feed network proposed in [52]. To the best of the author's knowledge a center-fed (feeding from the center conductor of the ring-slot) configuration has never been implemented in published literature. For this antenna the ring-slot is placed at the bottom of the substrate, where the same substrate as described in Section 3.1 was used. The feed network consists of a microstrip transmission line that feeds

a capacitive stub and was placed on the top side of the substrate. The main advantage of using this type of feeding configuration is that it has a convenient structure for the implementation of a dual-circularly polarized antenna, which would require a dual-feed configuration that is connected to a branch line coupler. The single feed configuration was first investigated, in order to better understand how the input impedance changes as the feed parameters are adjusted. A probe feed was used to excite the microstrip line, since it was found that the use of a waveguide port in this configuration can negatively impact the radiation pattern.

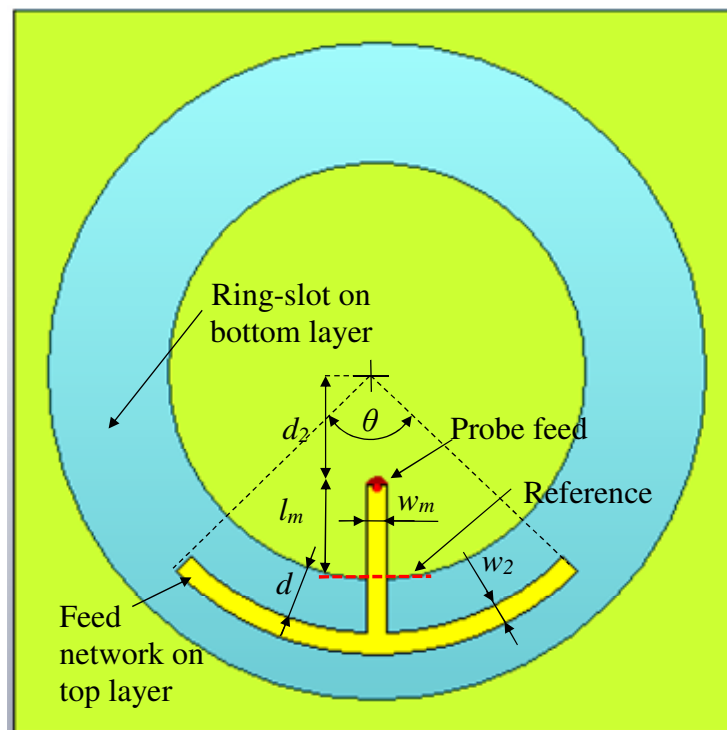


**Figure 3.16.** Ring-slot antenna with a single center-fed microstrip capacitive feed, with the following optimized dimensions:  $l = 140$  mm,  $w = 10$  mm,  $d = 4.5$  mm and  $\theta = 90^\circ$ .

For this study the ground plane size  $L$  was chosen as 60 mm. The width of the microstrip line  $w_m$  was chosen as 1.75 mm, which corresponds with a  $50 \Omega$  transmission line. The width of the angular feed stub  $w_2$  was also chosen as 1.75 mm. In order to leave enough space for a reduced size branch line coupler to comfortably fit on top of the center conductor, the parameter  $d_2$  was chosen as 9.5 mm. The antenna dimensions  $l$ ,  $w$ ,  $\theta$  and  $d$  were optimized

in order to achieve an optimal performance in terms of matching and cross-polarization discrimination in the frequency band of interest. The values of these parameters are shown in Figure 3.16 and the achieved return loss is shown in Figure 3.17. The return loss across the bandwidth of interest is approximately 35 dB, which is comparable to the results of the capacitively-fed CPW ring-slot antennas in Figure 3.13.

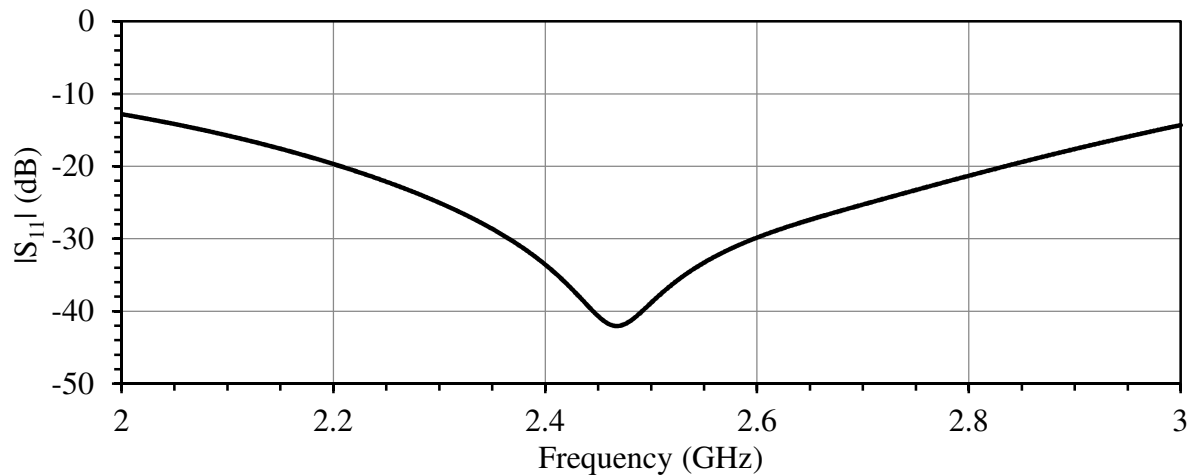


**Figure 3.17.** Return loss over frequency at the probe feed.

The maximum gain and cross-polarization discrimination of 3.8 dB and 22.4 dB was achieved, respectively. When comparing these results to the results from the capacitively-fed CPW ring-slot antennas shown in Table 3.2, the results from the antenna in Figure 3.16 achieved a lower gain and a higher cross-polarization discrimination. Figure 3.18 shows the radiation pattern in the two principle planes, which is comparable with the pattern data in Figure 3.15. Figure 3.19 shows the E-field distribution on the antenna surface. The field strength in the H-plane is significantly less than field strength in the E-plane. This means that a second feed could potentially be placed in one of the regions with low intensity E-field density with minimal cross talk between the feed elements.

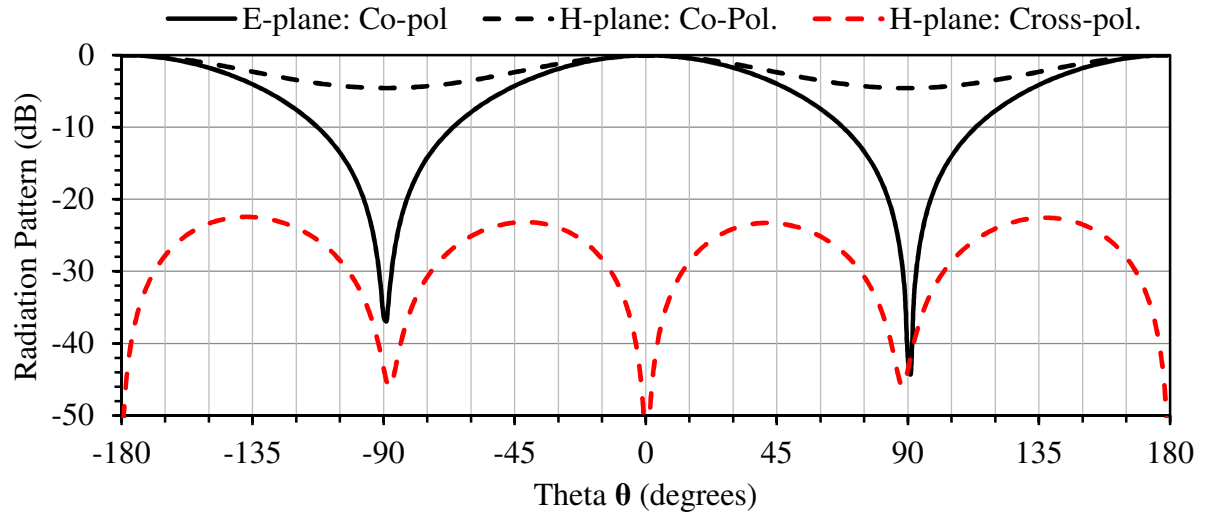


**Figure 3.18.** Radiation pattern in the E-plane and H-plane.

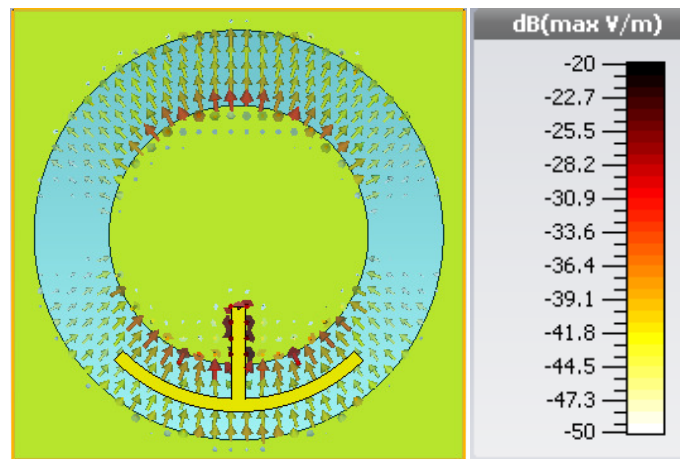


**Figure 3.19.** E-field distribution.

Since a probe feed was used to excite the microstrip line, mathematical de-embedding was required in order to obtain the impedance at the reference point, which is located where the microstrip line ends, as shown in Figure 3.16. Equation (3.1) shows the standard lossless transmission line equation used to transform the impedance from the feed point to the reference position. The characteristic impedance  $Z_0$  and the wavenumber  $\beta$  were determined through CST for a given value of the microstrip line width  $w_m$ .

$$Z_{11ref} = \frac{Z_0(Z_{11} + jZ_0 \tan(-\beta l_m))}{(Z_0 + jZ_{11} \tan(-\beta l_m))} \quad (3.1)$$

Figures 3.20 to 3.22 show how the impedance changes at 2.45 GHz as the parameters  $\theta$ ,  $w_2$ , and  $d$  are adjusted. The results from Figure 3.20 shows that when  $\theta$  was adjusted the input reactance either increased or decreased, while the input resistance remained fairly constant, similar to the trend shown in Figure 3.10. For the cases when either  $w_2$  or  $d$  were adjusted the input resistance either increased or decreased, although an inverted relationship to the results shown in Figure 3.11 and 3.12 is observed. Also note while the input reactance also changed significantly as the parameters  $w_2$  or  $d$  were adjusted. This makes the matching more difficult than for the capacitively-fed CPW ring-slot case. Matching can still be achieved by first adjusting the parameters  $w_2$  or  $d$  until the desired input resistance is achieved, then by adjusting  $\theta$ , the desired input reactance can be achieved.

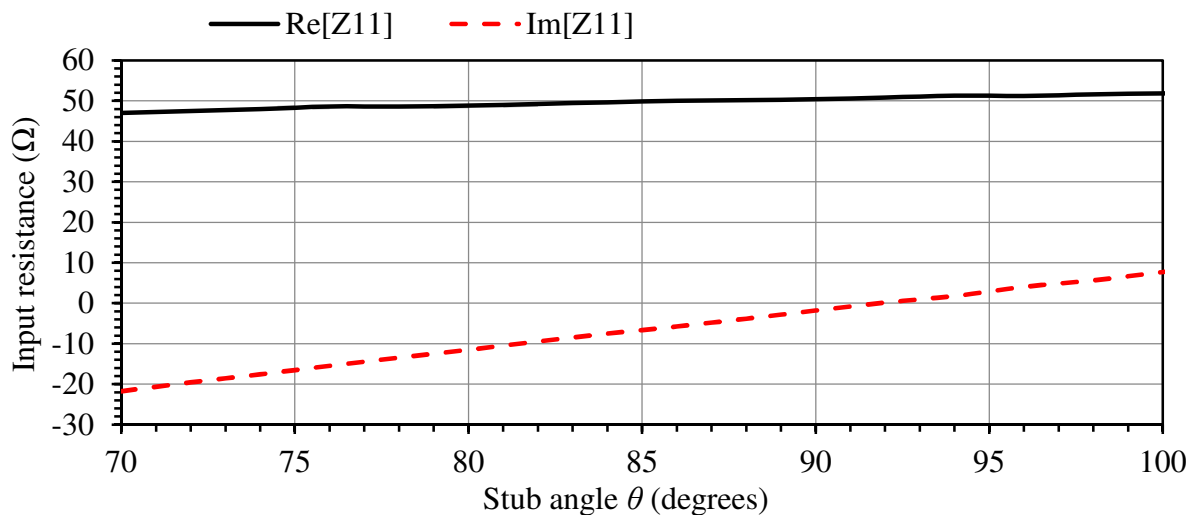


**Figure 3.20.** Input impedance at the reference over stub angle  $\theta$  at 2.45 GHz, where  $d = 4.5$  mm,  $w_2 = w_m = 1.75$  mm.

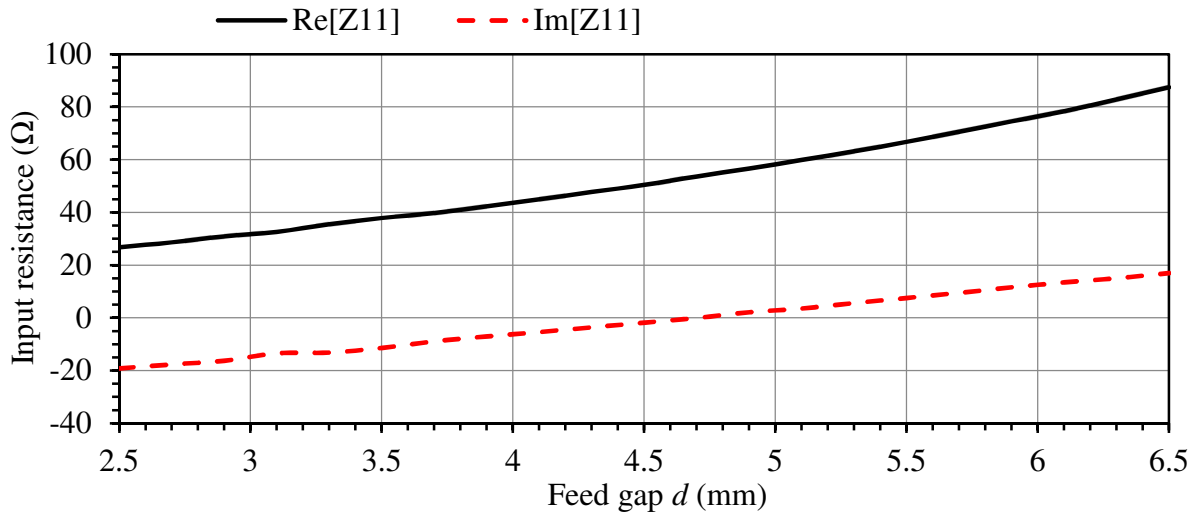


**Figure 3.21.** Input impedance at the reference over feed gap  $d$  at 2.45 GHz, where  $\theta = 90^\circ$ ,  $w_2 = w_m = 1.75$  mm.

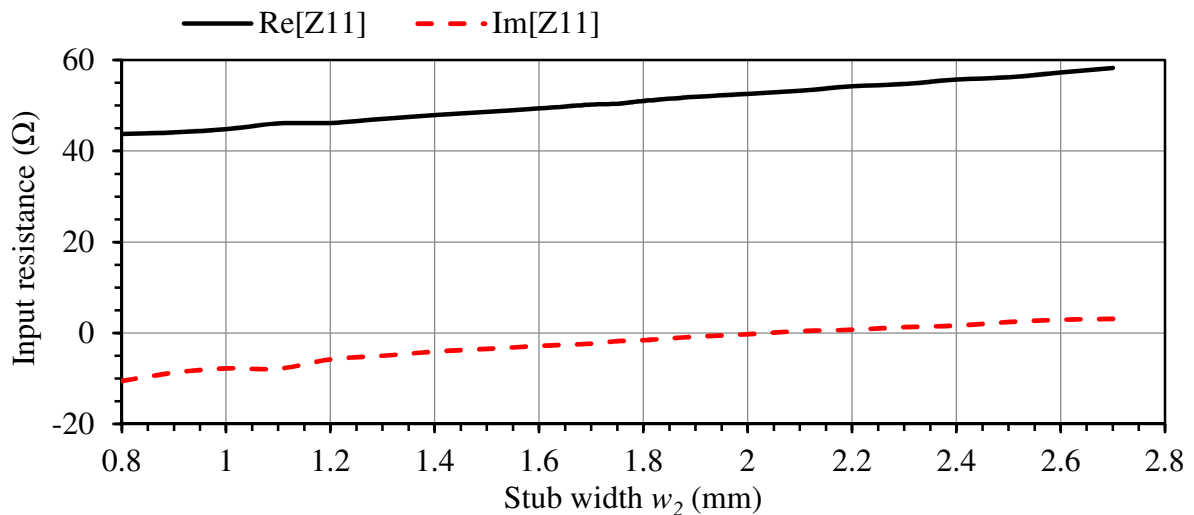


**Figure 3.22.** Input impedance at the reference over stub width  $w_2$  at 2.45 GHz, where  $\theta = 90^\circ$ ,  $d = 4.5$  mm,  $w_m = 1.75$  mm.

Note that the optimal matching was achieved when  $\theta = 90^\circ$ , which is too large for the use of an orthogonal dual-feed network. So a method of reducing this angle (other than increasing the slot width) was investigated. It was found that by reducing the width  $w_m$ , the input inductance can be increased and the stub angle  $\theta$  can then be decreased. Figure 3.23 shows the input impedance at the reference as the width  $w_m$  is adjusted.

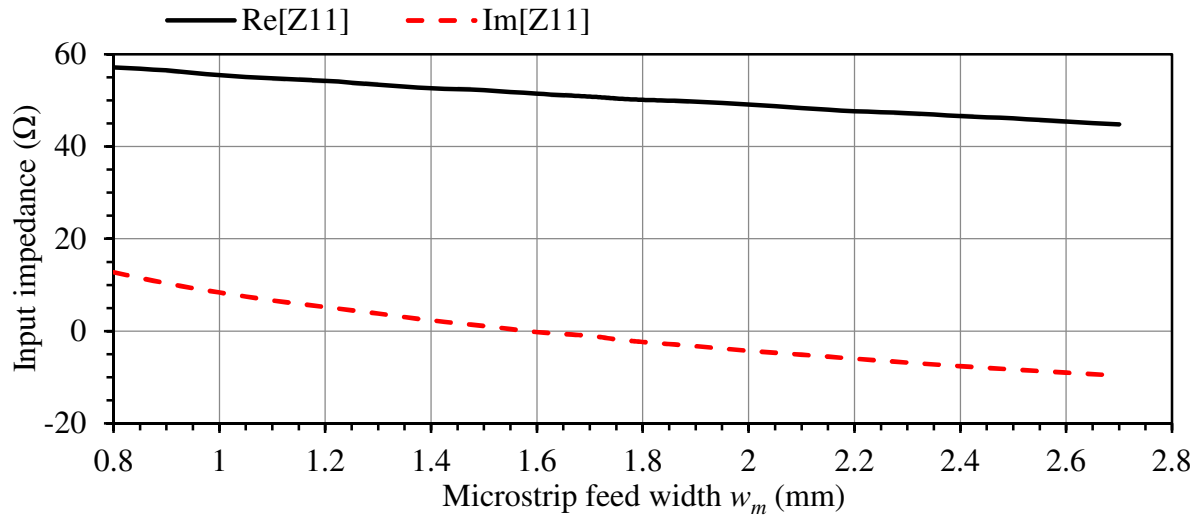


**Figure 3.23.** Input impedance at the reference over feed width  $w_m$  at 2.45 GHz, where  $\theta = 90^\circ$ ,  $d = 4.5$  mm,  $w_2 = 1.75$  mm.

### 3.3.2 Ring-slot antenna with center-fed microstrip capacitive feed.

In this section a ring-slot antenna with a single center-fed microstrip capacitive feed was extended to an orthogonal dual-feed configuration. The structure is shown in Figure 3.24. The impedance matching was found to work in a similar way to the single feed case, although for the dual-feed case the isolation between the ports also becomes a crucial design concern. It was found that only the slot width  $w$  and the slot length  $l$  have a significant effect on the isolation. The maximum achievable isolation was found to be mainly determined by the slot width  $w$ , while the frequency where the maximum isolation is located was found to be determined by the slot length  $l$ .

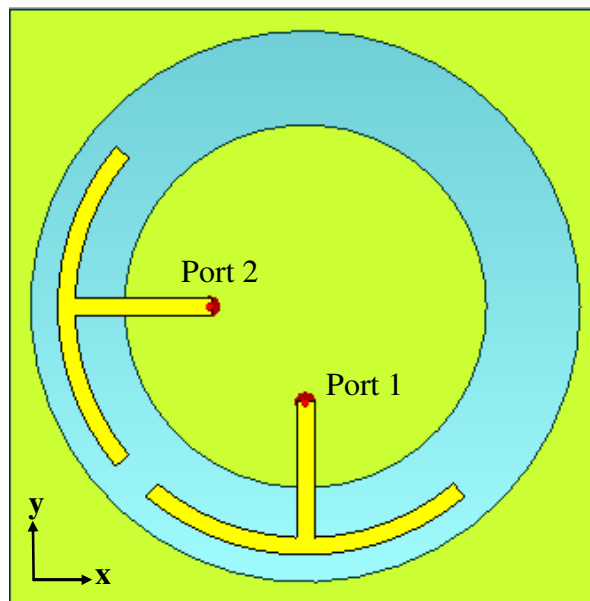


**Figure 3.24.** Ring-slot antenna with dual center-fed microstrip capacitive feeds.

As a first design attempt the antenna parameters were optimized while keeping the microstrip width  $w_m$  at 1.75 mm ( $\sim 50 \Omega$ ). The goal was to achieve a minimum return loss and a maximum isolation in the bandwidth of interest. Figure 3.25 shows the return loss and isolation for this design attempt (labelled “Case 1”). The results shows a return loss and isolation of 20 dB and 12 dB in bandwidth of interest, respectively. The return loss is significantly higher than the results achieved for the single feed case. In order to improve the return loss, the width  $w_m$  was also optimized together with the other parameters. The results for this design attempt is also shown Figure 3.25 (labelled “Case 2”), and the optimized parameters for both cases are shown in Table 3.3. From the result is clear that the return loss improved significantly from the initial design.

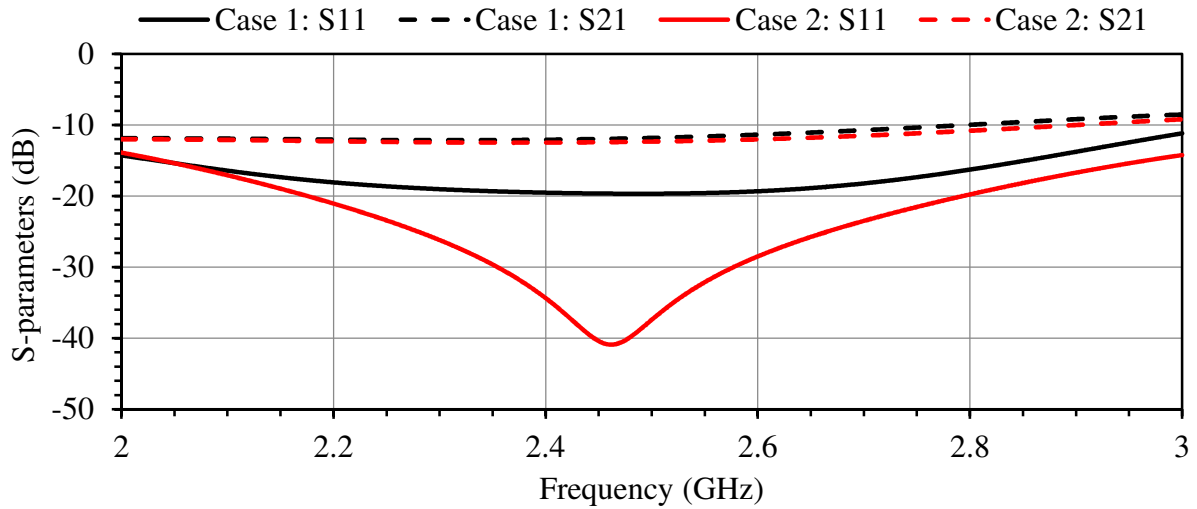


**Figure 3.25.** S-parameters over frequency for two design cases.

**Table 3.3.** Optimized parameters of the two design cases.

Case	slot width $w$ (mm)	slot length $l$ (mm)	Stub angle $\theta$ (degrees)	Feed gap $d$ (mm)	Stub width $w_2$ (mm)	Feed width $w_m$ (mm)
1	10	145	80	5	1.75	1.75
2	10	145	66	5	1.75	1.2

The results in Figure 3.25 shows that the isolation remained fairly constant even though the stub angle  $\theta$  was decreased from  $80^\circ$  to  $66^\circ$ , which seems counter-intuitive. In order to investigate the origin of the weak isolation, the E-field distribution on the antenna surface was simulated, as shown in Figure 3.26. Note that  $t = 0$  was defined as the time where the field had a maximum in the  $+y$  direction. What was learned from this simulation is that a portion of the field that travels along the center conductor couples to the microstrip line of the second feed. A portion of the coupled energy gets re-radiated by the second capacitive feed and causes a fairly significant cross-polarization component, as shown in Figure 3.26b.

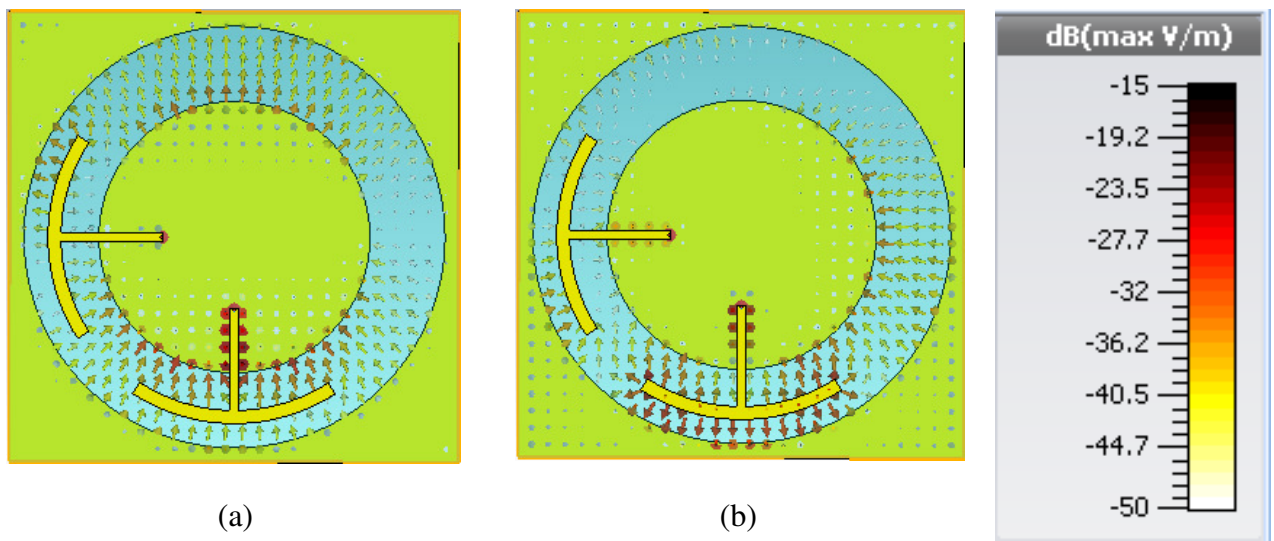


**Figure 3.26.** E-field distribution for a Port 1 excitation: (a)  $\omega t = 0$ , (b)  $\omega t = \pi/4$ .

In order to generate a circular polarization in the antenna, both ports were fed simultaneously with a  $90^\circ$  phase difference. For a LHCP excitation the ports were fed with a voltage ratio is  $\bar{v}_1/\bar{v}_2 = 1\angle 90^\circ$ . For this excitation a boresight axial ratio of 5.5 dB at 2.45 GHz was observed, which is undesirably high for many applications. It is suspected that this was caused asymmetrical field components shown in Figure 3.26b. As an attempt to improve the axial ratio, different amplitude ratios of  $|v_1/v_2|$  was experimented with. The results are shown in Figures 3.27 and 3.28. These results show a significant improvement in axial ratio as the voltage amplitude ratio  $|v_1/v_2|$  was decreased. This is a convenient solution since this type of signal excitation can be realized by using an un-equal split branch-line coupler, and would work equally well for a LHC or RHC excitation. When the phase ratio  $\angle v_1/v_2$  was adjusted from  $90^\circ$ , no improvement was noted. It was found however that the phase could be varied by  $\pm 1^\circ$  without any noticeable adverse effects on the axial ratio. The radiation pattern in shown in Figure 3.29 for a  $|v_1/v_2| = 0.7$  excitation. For this excitation, a gain of 3.5 dBic was achieved, which is lower than what was achieved of the single-feed case.

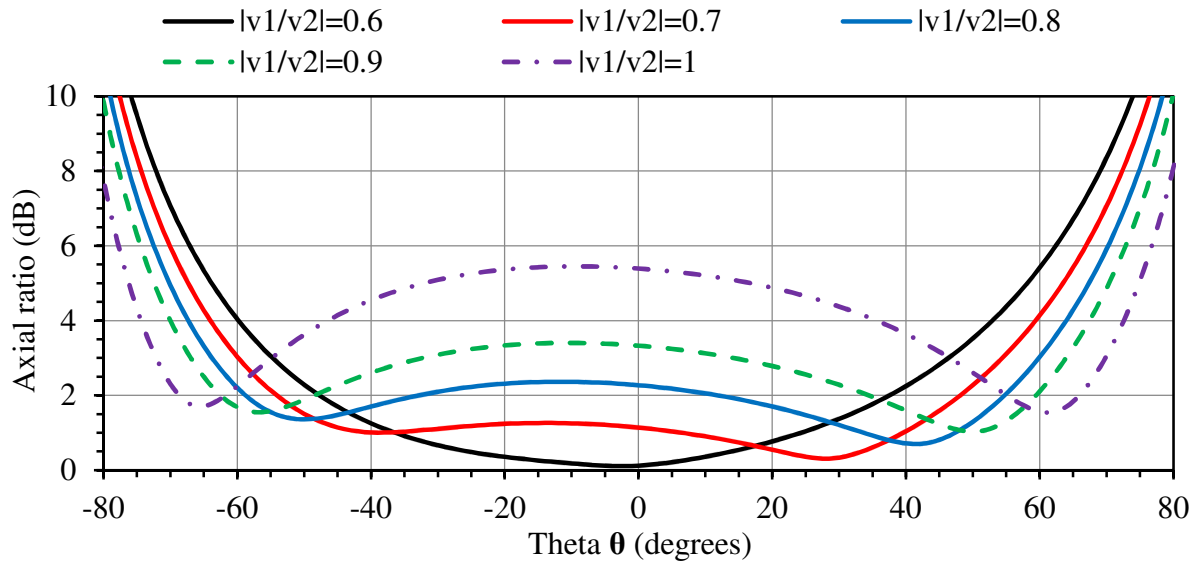


**Figure 3.27.** Axial ratio over theta angle  $\theta$  at 2.45 GHz in the YZ-plane, for various excitations of  $|v_1/v_2| \angle 90^\circ$ .

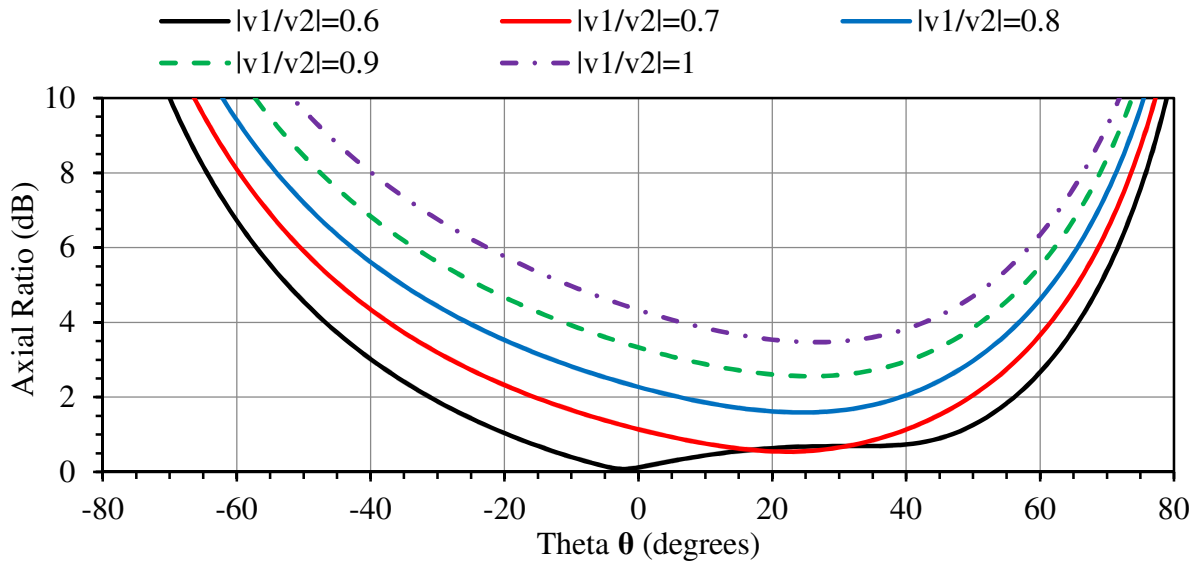


**Figure 3.28.** Axial ratio over theta angle  $\theta$  at 2.45 GHz in the XZ-plane, for various excitations of  $|v_1/v_2| \angle 90^\circ$ .

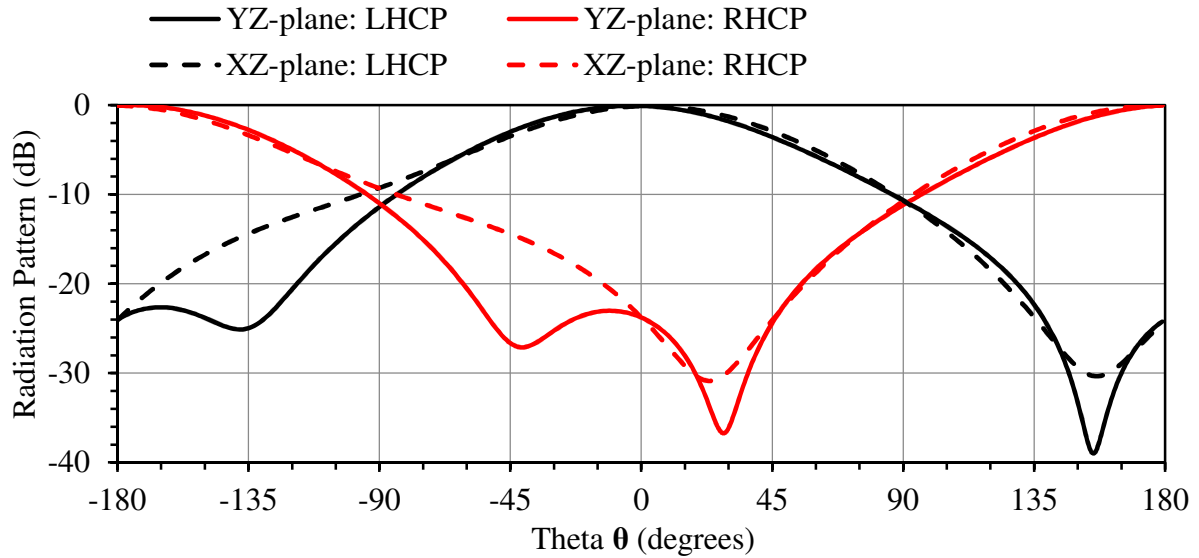


**Figure 3.29.** Radiation patterns in the YZ-plane and XZ-plane at 2.45 GHz, for a  $\bar{v}_1/\bar{v}_2 = 0.7\angle 90^\circ$  excitation.

### 3.4 RING-SLOT ANTENNAS LOADED WITH AMC REFLECTORS

#### 3.4.1 Square patch AMC analysis and design.

In Section 2.2.2 the basic operation of an AMC reflector was explained. This section will present the design and analyses of a square patch AMC reflector. This analysis is based on the equations in [26, 28]. The work by Sievenpiper et al. [26] showed that the surface impedance of a “mushroom” type AMC can be described in terms of an equivalent capacitance and inductance. The capacitance is dependent on the size of the patches and the spacing between the patches, while the inductance is dependent on the height of the via that connects the top and bottom sections of the AMC surface [26]. The surface impedance of an AMC reflector is described in Equation (3.2). According to [28], the capacitance and inductance is equivalent to that of a CPW transmission line on top of a ground plane. The dimensions of the AMC patch array is shown in Figure 3.30. The height of the AMC structure was defined as  $h$ . In order to simulate an infinite sized patch array AMC surface, a single unit cell was placed inside the boundary conditions shown in Figure 3.30. Note that the PEC side walls are orthogonal to the direction of the E-field, while PMC side walls are parallel to the direction of the E-field.

$$\eta = j \frac{X_L X_C}{X_C - X_L} = j X_{LC} \quad (3.2)$$

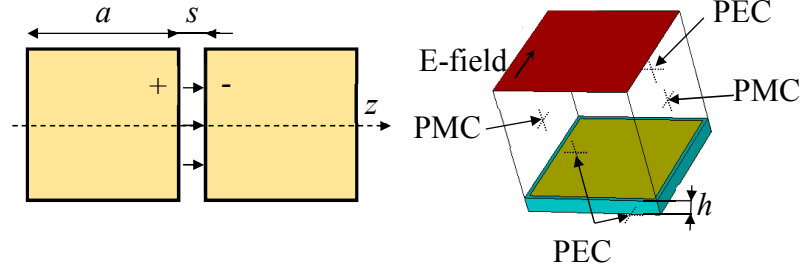


**Figure 3.30.** CST simulation setup with dimensions of AMC unit cell.

The reactance  $X_C$  is defined in Equation (3.3) and the equivalent capacitance is defined in Equations (3.4 - 3.6) [28]. Equation (3.4) states that the capacitance  $C$  is approximately equal to the capacitance per unit length multiplied by the effective length  $\tilde{a}$ . According to [28], the effective length must be chosen less than the patch size  $a$ . The authors did not go into detail of how this value should be chosen. Working back from the example they gave, it was determined that they used an effective length of  $\tilde{a} = 0.7a$ . Equation (3.6) shows how the effective permittivity  $\varepsilon$  was calculated. In this equation it is assumed that half of the energy is located in the free space above the AMC, while the other half is located in the region between the patches and the ground plane.

$$X_C = \frac{1}{\omega C} \quad (3.3)$$

$$C \approx C_0 \cdot \tilde{a} = \frac{\varepsilon K \left( \sqrt{1 - \left( \frac{s}{2(a + s/2)} \right)^2} \right)}{K \left( \frac{s}{2(a + s/2)} \right)} \cdot \tilde{a} \quad (3.4)$$

$$K(z) = \int_0^{\pi/2} \frac{d\phi}{\sqrt{1 - z^2 \sin^2 \phi}} \quad (3.5)$$

$$\varepsilon = \varepsilon_0 \left( \frac{\varepsilon_r + 1}{2} \right) \quad (3.6)$$

The reactance  $X_L$  is defined in Equation (3.7) and the equivalent inductance is defined in Equations (3.8 - 3.9) [28]. Equation (3.7) shows that the inductance can be expressed as an equivalent transmission line with a characteristic impedance  $Z_h$ . The surface impedance  $\eta$  can then be converted to a reflection coefficient using Equation (3.10).

$$X_L = Z_h \tan kh = \omega L \quad (3.7)$$

$$k = k_0 \sqrt{\epsilon_r} \quad (3.8)$$

$$Z_h = \frac{\eta_0}{\sqrt{\epsilon_r}} \quad (3.9)$$

$$\Gamma = \frac{\eta - \eta_0}{\eta + \eta_0} \quad (3.10)$$

By choosing  $\epsilon_r = 3.38$ ,  $s = 1.5$  mm,  $h = 3.048$  mm, and  $\tilde{a} = 0.7a$ , the patch size was adjusted until Equation (3.10) resulted in a  $0^\circ$  phase at 2.45 GHz. The same was done for a CST unit cell simulation, as shown in Figure 3.30, where the direction of the E-field was defined in the direction one of the PEC walls. When equation (3.10) was used the optimized patch size was found to be 26.3 mm. For the CST simulation the optimized patch size was found to be 25.5 mm, where the parameter  $\epsilon_r$ ,  $s$ ,  $h$  was chosen the same. The results from Equation (3.10) was compared to a CST unit cell simulation, as shown in Figure 3.31, where the direction of the E-field was defined in the direction one of the PEC walls. The simulated and calculated results in Figure 3.31 are in good agreement.

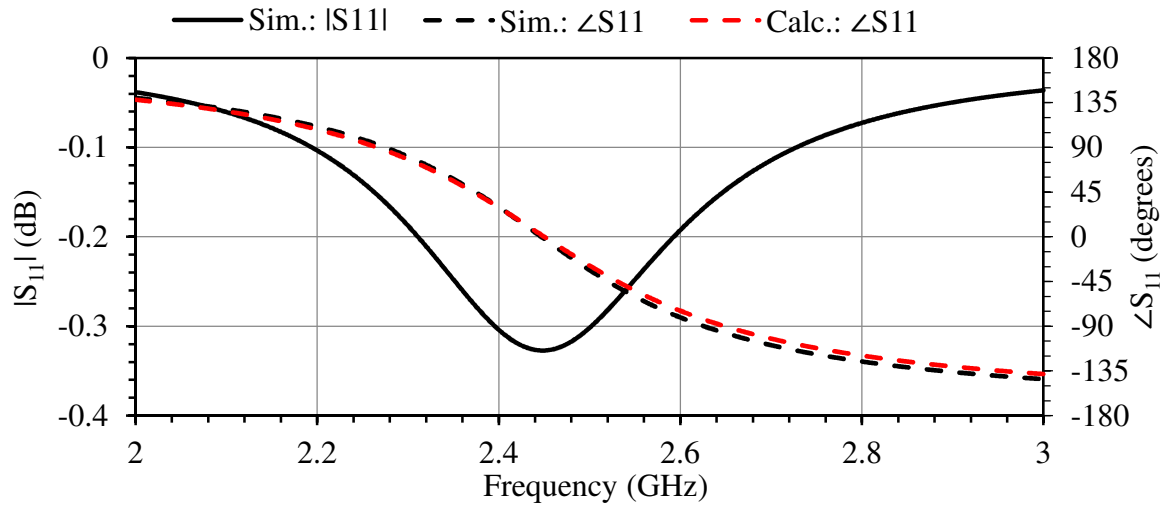


**Figure 3.31.** Simulated and calculated reflection coefficient.

Now that a solid mathematical foundation has been established, some design aspect of AMC reflectors can be investigated. As mentioned in Section 2.2.2 the fractional phase bandwidth is dependent on the capacitance and the inductance of the surface, as shown in Equation (2.1) [26]. For a given center frequency however, it seems that the capacitance does not influence the achievable fractional bandwidth. This can be illustrated by rearranging Equation (2.1), as shown in Equation (3.11). From this it is clear that the fractional bandwidth can only be increased by increasing the surface inductance or by choosing a higher the center frequency.

$$\Delta\omega/\omega_0 = \frac{\sqrt{L/C}}{\eta_0} = \frac{\omega_0 L}{\eta_0}, \quad \text{where } \omega_0 = \frac{1}{\sqrt{LC}} \quad (3.11)$$

The fractional phase bandwidth is often defined as the frequency range over which the phase response is greater than  $-90^\circ$  and less than  $+90^\circ$ . Some authors have noted that a good impedance match is often only achievable where the phase is greater than  $-45^\circ$  and less than  $45^\circ$  [11, 12]. In order to determine the  $\pm 45^\circ$  fractional phase bandwidth, the Equation (3.10) was solved numerically for a given height and the capacitance was adjusted until the reflection phase was  $0^\circ$  at the desired frequency (2.45 GHz). Figure 3.32 shows how the bandwidth increases as the height is increased. Note when  $\epsilon_r$  was increased, the bandwidth decreased for higher values of  $h$ . Figure 3.33 shows unit cell size for a given substrate height and Figure 3.34 shows unit cell size for a given relative permittivity  $\epsilon_r$  of the substrate. The

results in Figures 3.32 and 3.33 show that the overall size of the unit cell can be reduced by either increasing the height  $h$  or increasing the relative permittivity  $\epsilon_r$  of the substrate.

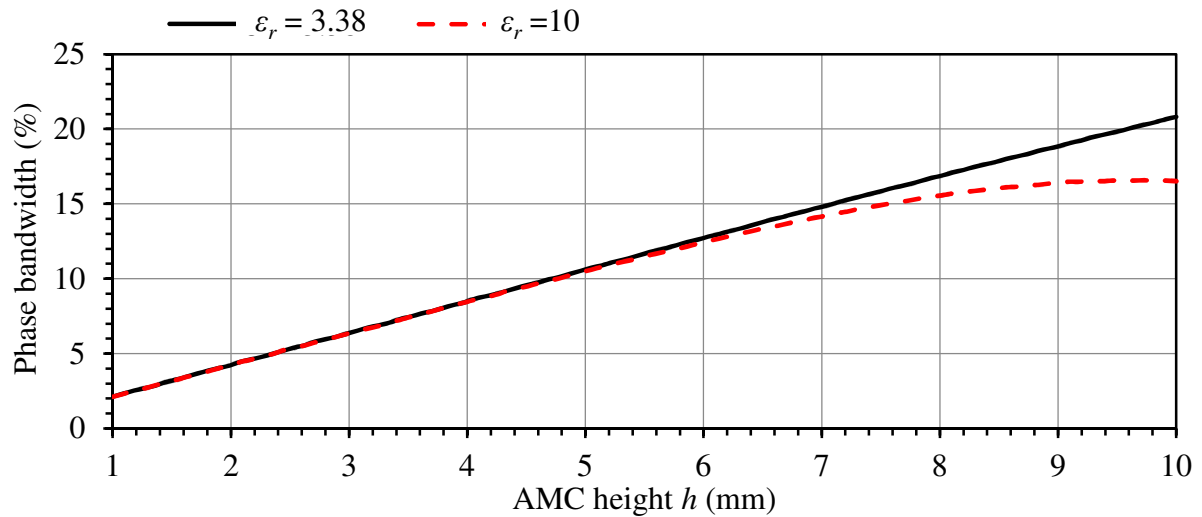


**Figure 3.32.** Calculated  $\pm 45^\circ$  fractional phase bandwidth for a given AMC height  $h$  and patch spacing  $s$ .

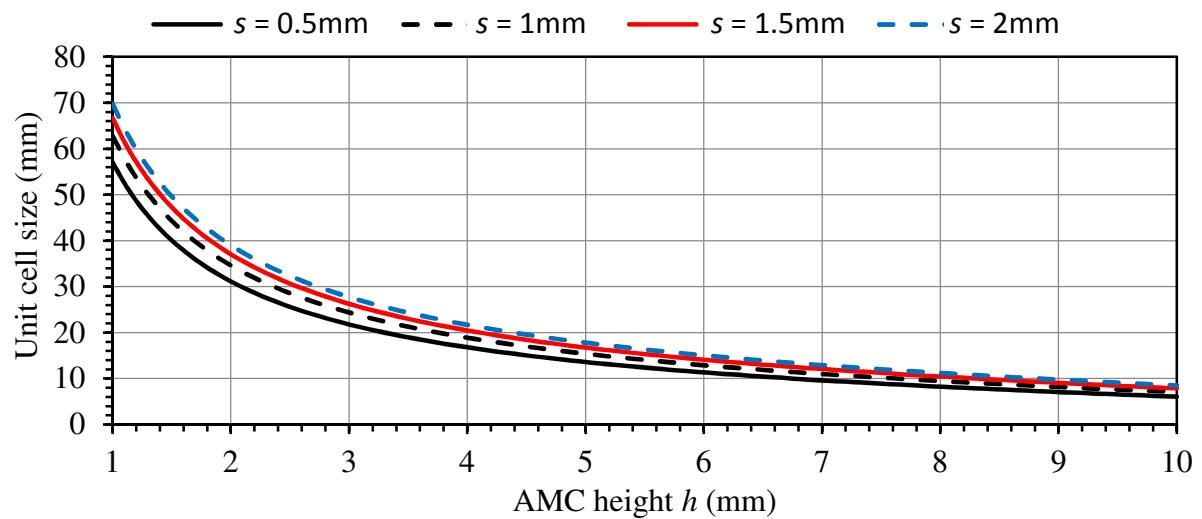


**Figure 3.33.** Calculated unit cell sizes ( $a + s$ ) for a given AMC height  $h$  and patch spacing  $s$ .

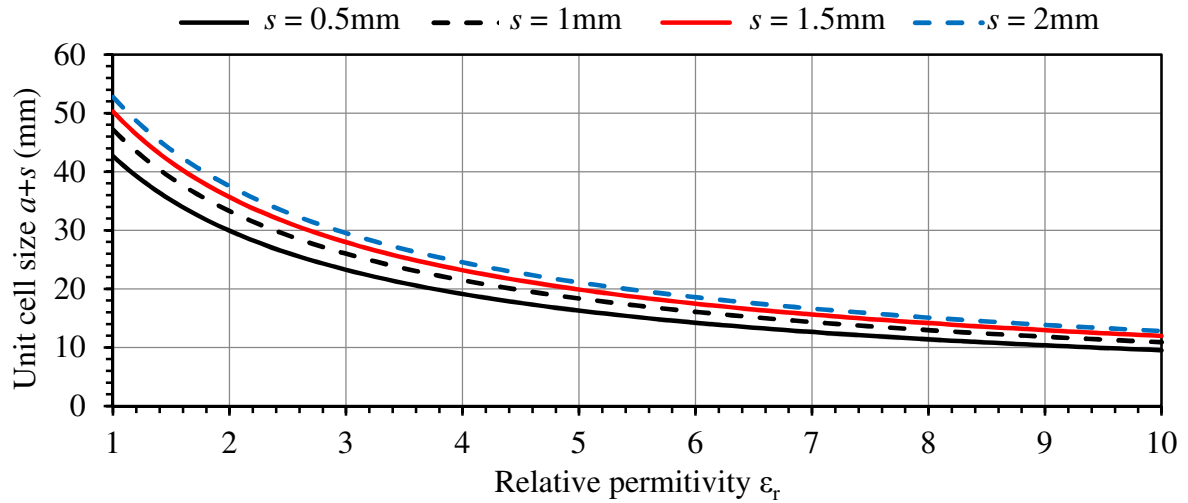


**Figure 3.34.** Calculated unit cell sizes ( $a + s$ ) for a given AMC relative permittivity  $\epsilon_r$  height  $h$  and patch spacing  $s$ .

### 3.4.2 Capacitively-fed CPW ring-slot on top of an AMC reflector.

The cavity-backed ring-slot antenna loaded with the AMC reflector as shown in Figure 3.35. The substrate used for both the radiating slot and the AMC reflector was Rogers RO4003, with  $\epsilon_r = 3.38$  and  $\tan \delta = 0.0021$ . For the radiating slot element a substrate height  $h_1$  was chosen as 0.813 mm. The height of the substrate  $h_2$  primarily controls the bandwidth of the AMC reflector and was chosen as 3.048 mm in order to have a  $\pm 45^\circ$  reflection phase bandwidth of 6.5%.

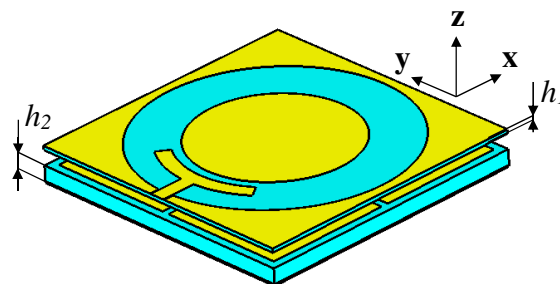


**Figure 3.35.** Printed CPW-fed ring-slot antenna above an AMC reflector.

The basic AMC reflector structure consisted of  $2 \times 2$  array of patches spaced 3.0 mm below the radiating element. It was found that when the spacing between the antenna and the AMC reflector was reduced, the front-to-back ratio was significantly worsened. The AMC reflector dimensions  $a$  and  $s$  was chosen as 25.5 mm and 1.5 mm, respectively, in order for the

structure to resonate at 2.45 GHz. A rectangular cavity dimension  $L = 56$  mm was used for this design. A slot width of  $w_1 = 10$  mm was chosen, and optimized slot length of  $l = 134$  mm was used.

The parametric study showed that the two dimensions have an almost independent effect on the real and imaginary parts of the input impedance. Figure. 3.36 shows that the imaginary part of the input impedance changes significantly as the angle  $\theta$  is adjusted, while the real component stays relatively constant. Figure. 3.37 shows the effect of varying  $d$  while keeping the angle  $\theta$  constant, with the imaginary part almost unchanged as function of dimension  $d$ . These results are consistent with the parametric study in Section 3.12, which shows that the feed structure is fairly unaffected by the AMC reflector.

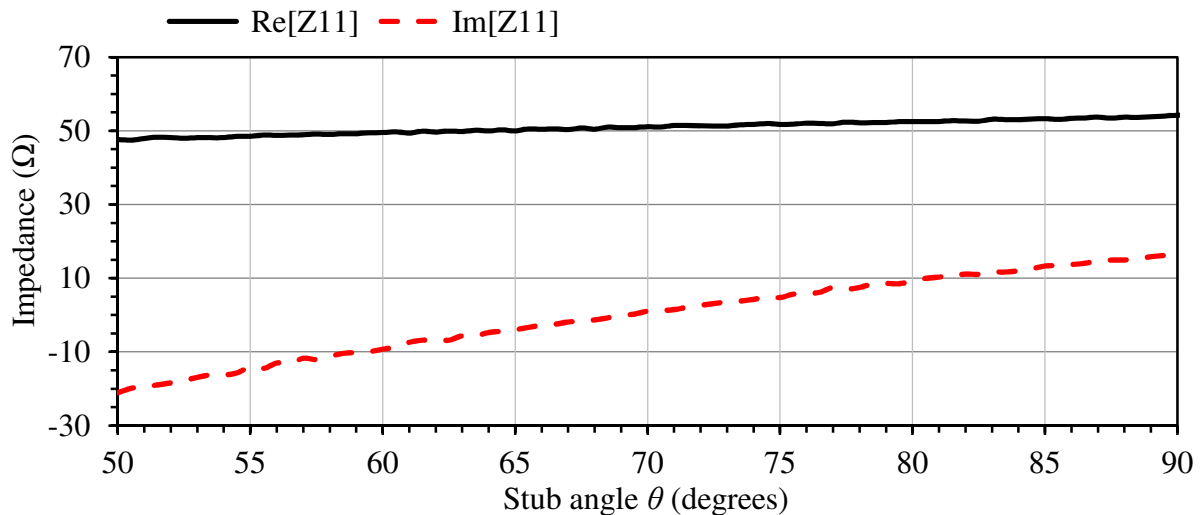


**Figure 3.36.** Input impedance of the ring-slot antenna as the stub angle was varied. The distance  $d$  was kept at a constant value of 1.89 mm.

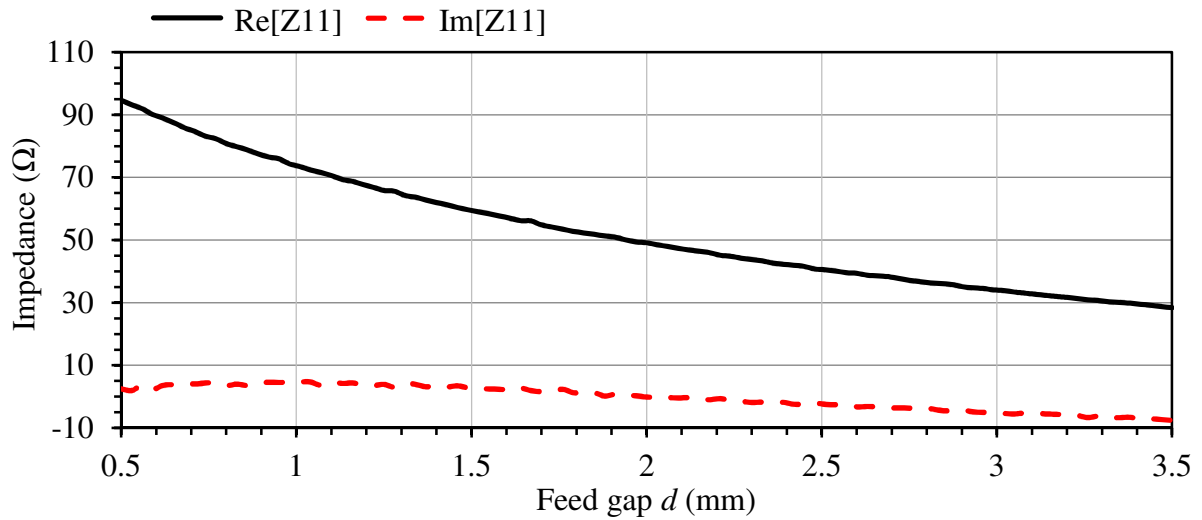


**Figure 3.37.** Input impedance of the ring-slot antenna as the parameter  $d$  was varied. The angle  $\theta$  was kept at a constant value of  $70^\circ$ .

Table 3.4 summarizes some design dimensions and characteristics for different slot widths (all performed for the same cavity dimension  $L = 56$  mm). The CPW feedline dimensions  $w_{CPW} = 3$  mm and  $s_{CPW} = 0.25$  mm were used. From these results it is clear that the impedance bandwidth increases as the slot-width increases. The front-to-back ratio and the cross-polarization are optimum for a specific slot width, which may be affected to a minor degree by the choice of the rectangular cavity dimension. The design process involved choosing the slot width and determining the optimum cavity dimension, and then an optimization process for the slot length and feed parameters to achieve impedance matching of the antenna. Figure 3.38 shows the reflection coefficient of the  $w_l = 10$  mm case and shows a -10 dB input reflection bandwidth of 5.5 %.

**Table 3.4.** Ring-slot radiators with different slot widths.

Slot width $w_l$ [mm]	Slot length $l$ [mm]	$\theta$ [degrees]	$d$ [mm]	-10 dB Band. [%]	F/B ratio [dB]	X-pol. [dB]
7	124	77.6	1.51	4.1	20.1	21.1
10	132	70	1.89	5.5	31	27
13	131	24	0.5	6	30.7	15.1

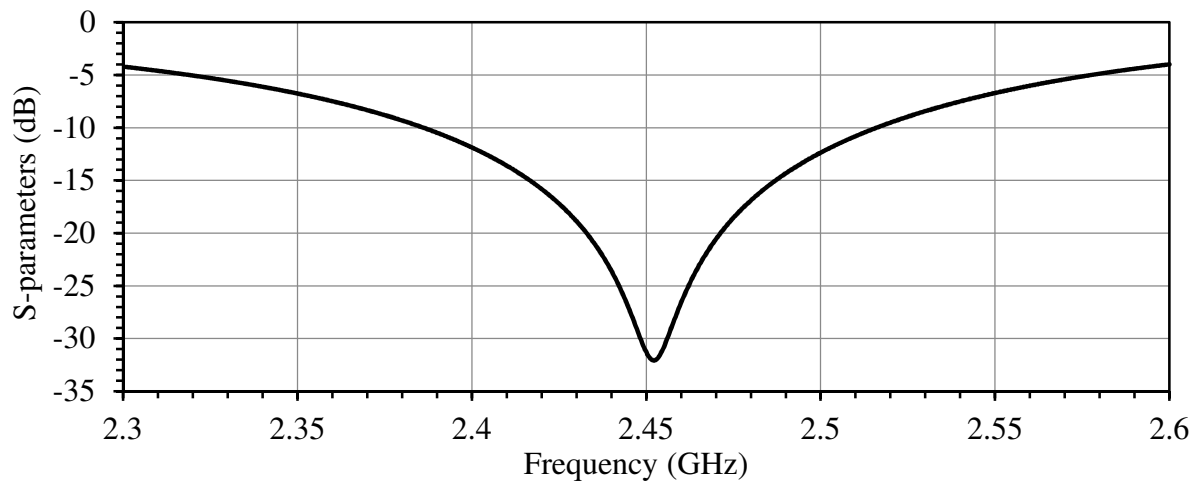


**Figure 3.38.** Input reflection coefficient for the case where  $w_l = 10$  mm.

The radiation patterns were also simulated for the  $w_l = 10$  mm case. Figure 3.39 shows the radiation patterns in the principle planes at the center frequency. The co-polarization patterns are fairly similar in the  $\pm 90^\circ$  region. Figure 3.40 shows how the gain changes over frequency. The results show a gain better than 6.9 dBi over the 2.4 GHz to 2.5 GHz bandwidth, with maximum gain of 7.23 dBi. Figures 3.41 and 3.42 show how the front-to-back ratio and the cross-polarization discrimination changes over frequency, respectively. In the bandwidth of interest a front-to-back ratio better than 23 dB and a cross-polarization discrimination better than 25 dB was achieved.

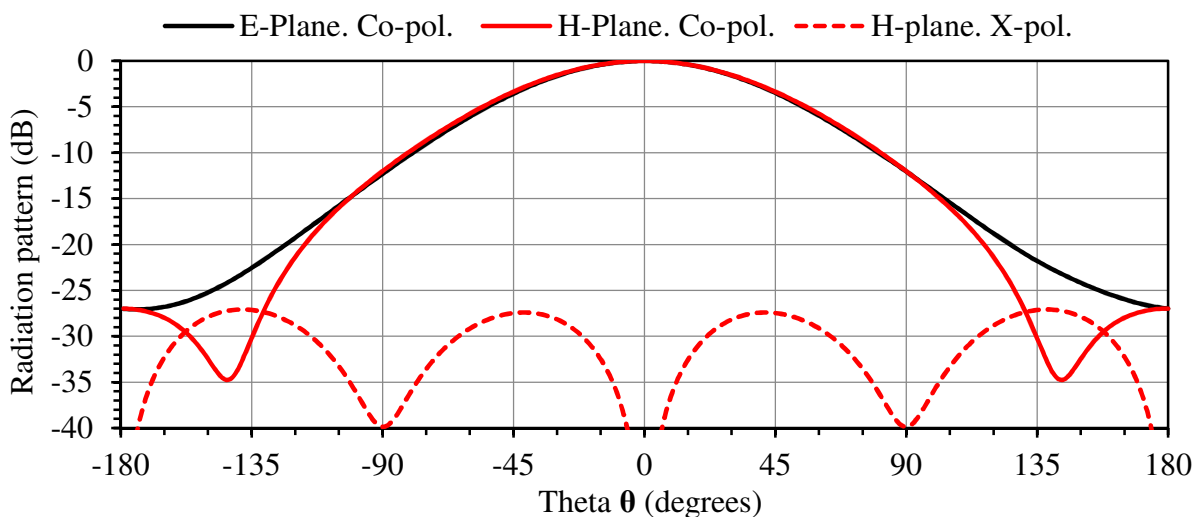


**Figure 3.39.** Radiation patterns in the E-plane and H-plane at 2.45 GHz, for the case where  $w_l = 10$  mm.

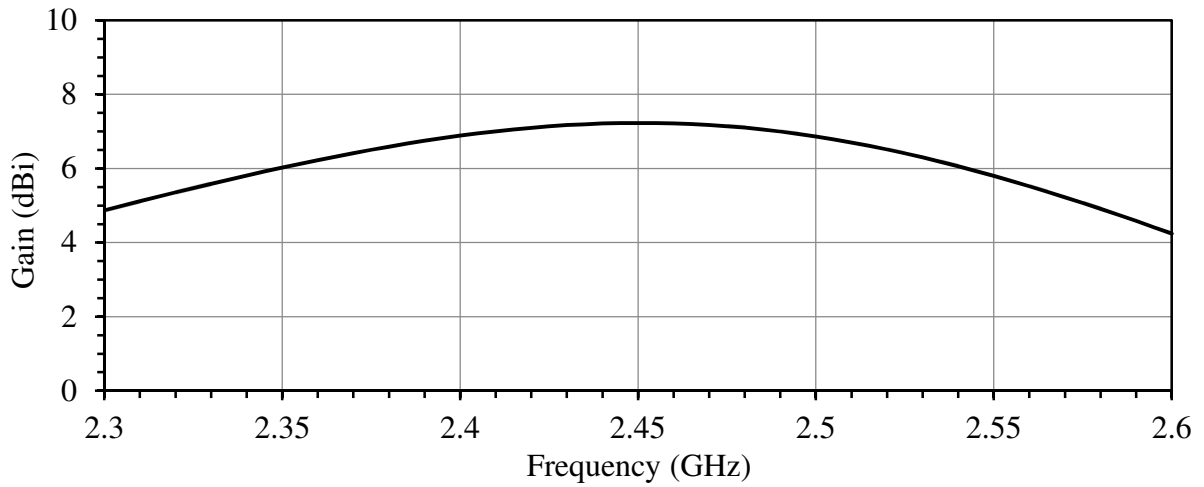


**Figure 3.40.** Gain over frequency for the case where  $w_l = 10$  mm.

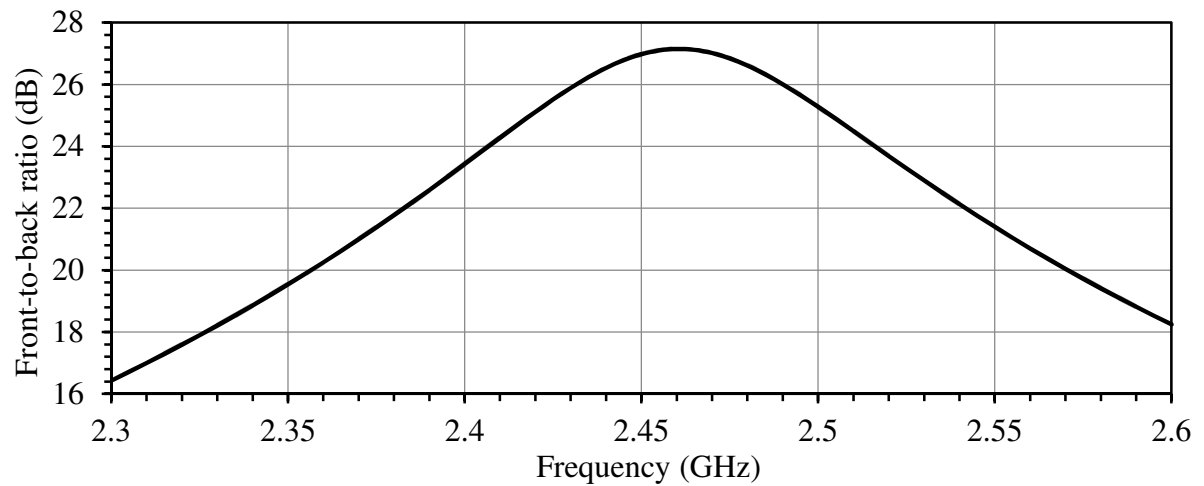


**Figure 3.41.** Front-to-back ratio over frequency for the case where  $w_l = 10$  mm.

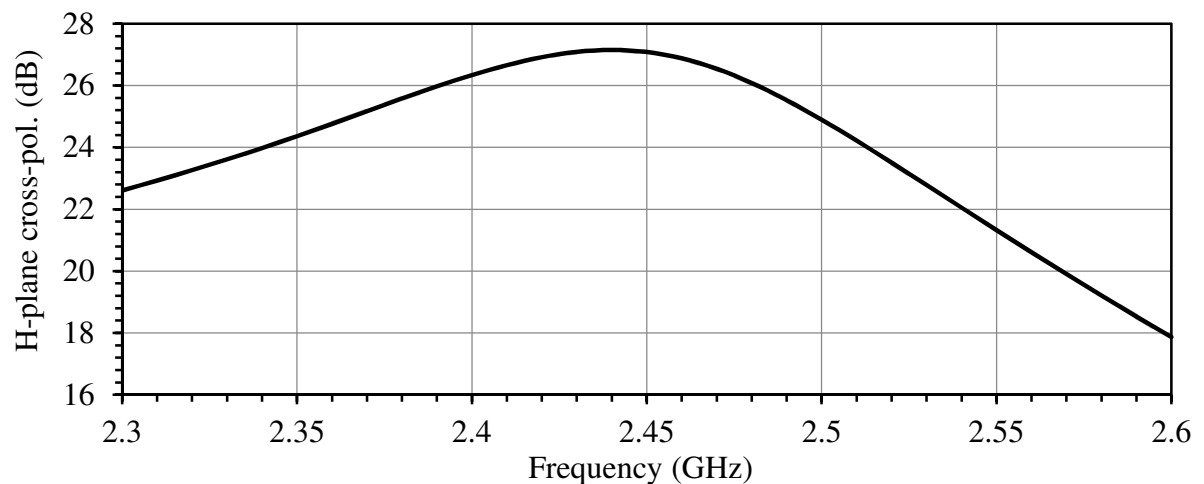


**Figure 3.42.** H-plane cross-polarization discrimination ratio over frequency for the case where  $w_l = 10$  mm.

### 3.4.3 Dual-fed microstrip ring-slot loaded with an AMC reflector.

In this section the dual-fed antenna from Section 3.2.2 was placed on top of an AMC reflector which consisted of  $2 \times 2$  array of patches spaced 3.0 mm below the radiating element. Once again the substrate heights  $h_1$  and  $h_2$ , was chosen as 0.813 mm and 3.048 mm respectively. This section also attempts to determine whether the coaxial cables that is required for a center-fed implementation, can have a significant effect on the performance of the antenna. As a first design attempt the parameters of the antenna was optimized without any coaxial feed lines. A second design attempt included the loadings effects of the coaxial cable, by modeling it as two lossy conductive cylinders that extends from the ground plane of the AMC reflector to the center conductor of the ring-slot antenna. The S-parameters for both designs are shown in Figure 3.43, and the optimized parameters are shown in Table 3.5.

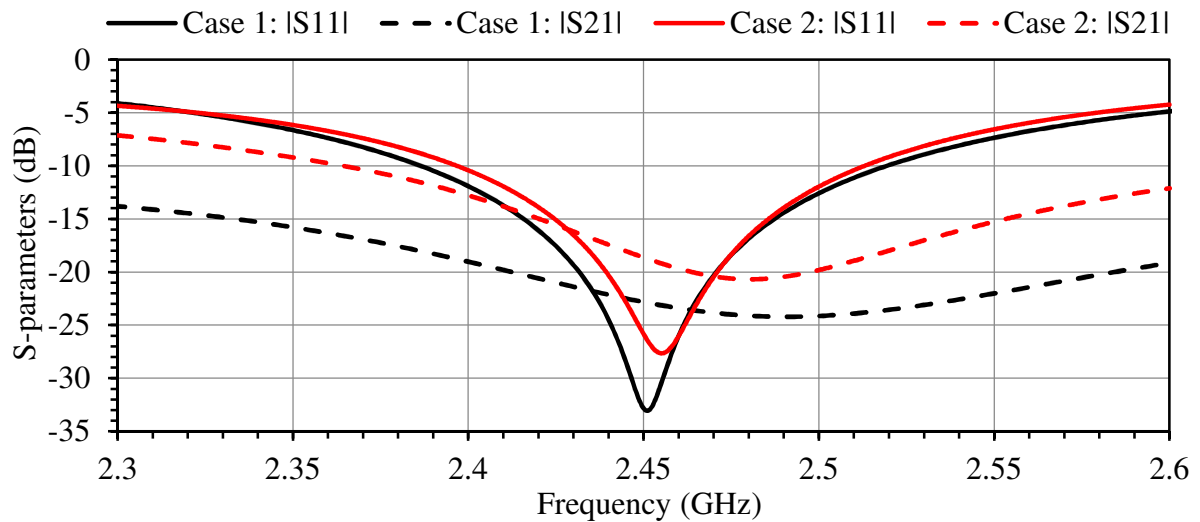


Figure 3.43. S-parameters of the dual-feed antennas.

**Table 3.5.** Optimized parameters for the two design cases.

Case	Slot width $w_1$ [mm]	Slot length $l$ [mm]	Stub angle $\theta$ [degrees]	Feed gap $d_1$ [mm]	Stub width $w_2$ [mm]	Feed width $w_m$ [mm]	Patch size $a$ [mm]	Patch spacing $s$ [mm]
1	10	145	65	5	1.75	1.2	23.2	1.5
2	10	127.5	70	2.83	0.88	0.45	25.5	1.5

For the first design (Case 1) a -10 dB input reflection bandwidth of 5.6 % was achieved, which is similar to what was achieved with the CPW-fed antenna discussed in Section 3.3.2. Across the 2.4 GHz to 2.5 GHz bandwidth of interest an isolation of better than 19 dB was achieved. As mentioned earlier the resonant frequency can be shifted higher or lower by adjusting the slot length. The resonant frequency can also be shifted in frequency by adjusting the patch size to gap ratio  $a/s$ , although it was found when this ratio was adjusted too far from its natural resonance frequency, the front-to-back ratio can be significantly reduced.

For a second design attempt (Case 2) metal cylinders with a diameter of 2.1 mm was added to the simulation model. The diameter of the cylinders corresponds to the outside diameter of a SUCOFORM SM 86 coaxial cable. The inside corners of some of the AMC patches were slightly modified because an open gap ( $r_1 = 1.6$  mm) was etched to electrically isolate the outer coaxial cable conductor from the AMC patches, as shown in Figure 3.44. The placement of the coaxial cables  $d_2$  was found to be very important. When the coaxial cables are not centrally located within the structure, it was found that the AMC reflector did not function as intended, causing the impedance matching to only be possible over a significantly smaller bandwidth. When  $d_2$  was chosen as 3 mm, a reasonable -10 dB input reflection bandwidth of 4.6 % could be achieved. For this design the isolation was 13 dB across the bandwidth of interest, which is significantly less than what was achieved in the previous case. This reduction in isolation can be attributed to the low value of the feed gap  $d_1 = 2.83$  mm that was used, in order to achieve the desired impedance bandwidth.

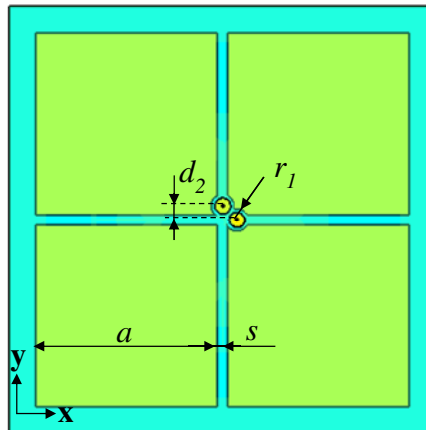


**Figure 3.44.** AMC reflector used for Case 2.

Figure 3.45 shows the radiation pattern for the Case 2 antenna that is excited at Port 1. The purpose of this simulation was to show how well the antenna works when used as a dual-linear antenna. The antenna achieved a maximum gain of 6.92 dBi, a front-to-back ratio of 24 dB, and a cross-polarization discrimination of 18 dB. These results show that the antenna works fairly well as a dual-linear polarized antenna. When the axial ratio study discussed in Section 2.2.3 was repeated and a voltage ratio of  $|v_1/v_2| = 0.6$  was once again found to result in the highest axial ratio beam width at the center frequency. When the axial ratio over frequency was investigated it was found that a voltage ratio of  $|v_1/v_2| = 0.75$  produced the highest 3 dB axial ratio bandwidth.

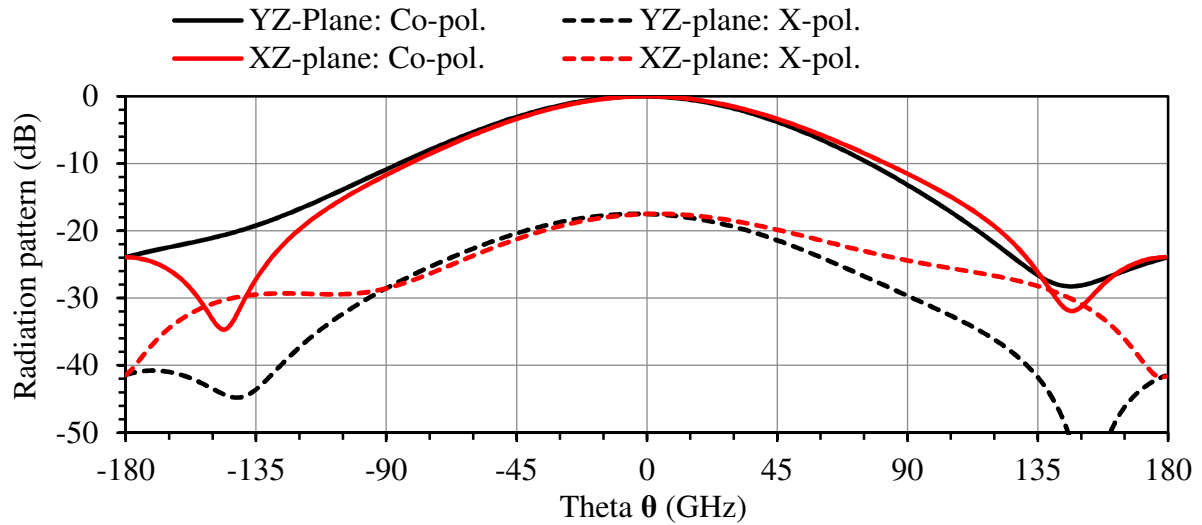


**Figure 3.45.** Radiation patterns in the YZ-plane and XZ-plane at 2.45 GHz, for a Port 1 excitation on the Case 2 antenna.

### 3.5 RING-SLOT ANTENNAS LOADED WITH AMC REFLECTORS

#### 3.5.1 Reduced size Branch line coupler design.

A conventional branch-line coupler for a Rogers RO4003 substrate would have a diameter of around 27 mm, which is too large to fit on the center conductor of the ring-slot, and hence a miniaturized version of such a coupler had to be used. The polar curves proposed in [29] were used to construct the branch-line coupler. Figure 3.46 shows the reduced size branch-line coupler fed with 50  $\Omega$  microstrip lines. The radial length from the center of the ring-slot structure to the middle of the curved microstrip line as a function of  $\phi$  is described in Equation (3.11).  $r_x$  is the minimum radius of the function. The constants  $B_1$  and  $B_2$  are the amplitudes of the sinusoids for the low impedance and high impedance lines respectively.

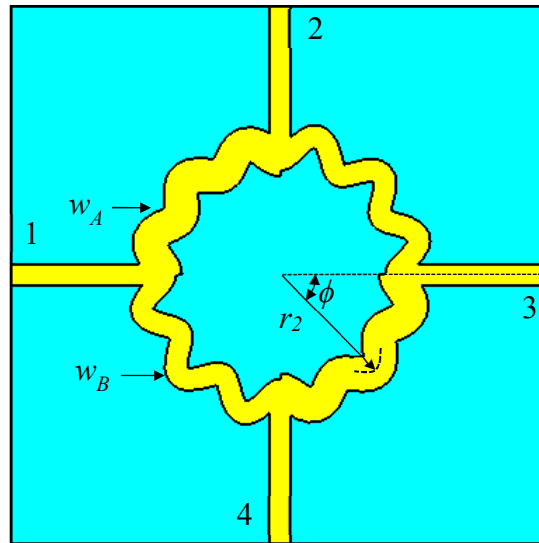


**Figure 3.46.** Simulation setup that was used to test the performance of the branchline coupler.

$$r_2(\phi) = \begin{cases} r_x + B_1(1 - \cos(12\phi)), & \phi \in [0^\circ, 90^\circ] \cup [180^\circ, 270^\circ] \\ r_x + B_2(1 - \cos(12\phi)), & \phi \in [90^\circ, 180^\circ] \cup [270^\circ, 360^\circ] \end{cases} \quad (3.12)$$

Numerical investigation on the antenna described in Section 3.3.3 showed that an unequal  $90^\circ$  hybrid coupler is required for the largest 3 dB axial ratio. It was found that a  $|v_1/v_2| = 0.75$  or 1.25 dB difference in magnitude between the two input ports of the dual-feed antenna is fairly optimum. For the case where the outputs (inputs of the dual-linear antenna) are chosen as Port 2 & 3, respectively, RHC polarization the phase and magnitude difference between capacitive feeds should be  $90^\circ$  and -1.25 dB (for LHC  $-90^\circ$  and 1.4 dB). The branchline coupler was designed to achieve the desired coupling with a return loss and isolation better than 15 dB across the bandwidth of interest. The final dimensions for the branch-line coupler are as follows:  $w_2 = 1.75$  mm,  $w_3 = 1.86$  mm,  $w_4 = 2.86$  mm,  $r_x = 9.5$  mm,  $B_1 = 0.79$  mm, and  $B_2 = 1.13$  mm. The S-parameters of the designed coupler is shown in Figure 3.47. The amplitude and phase difference is shown in Figures 3.48 and 3.49, respectively.

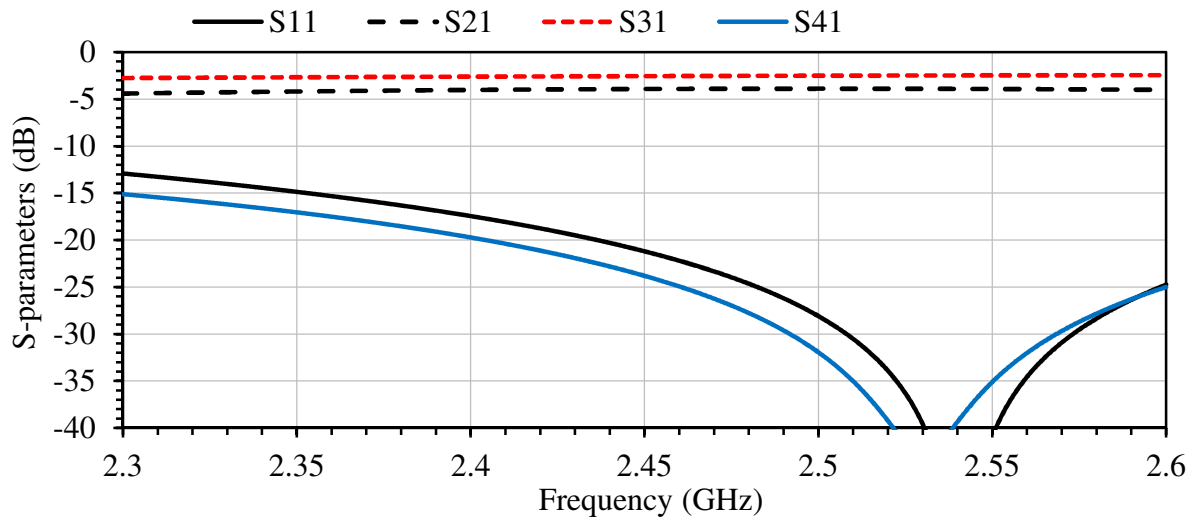


**Figure 3.47.** Amplitude and phase difference of the branch-line coupler.

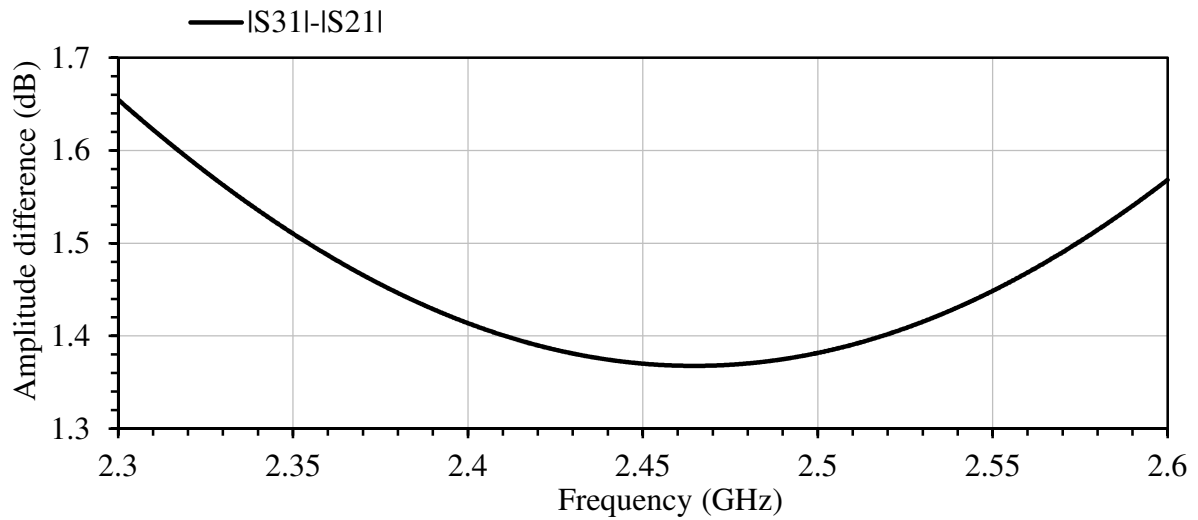


**Figure 3.48.** Amplitude difference of the branch-line coupler.

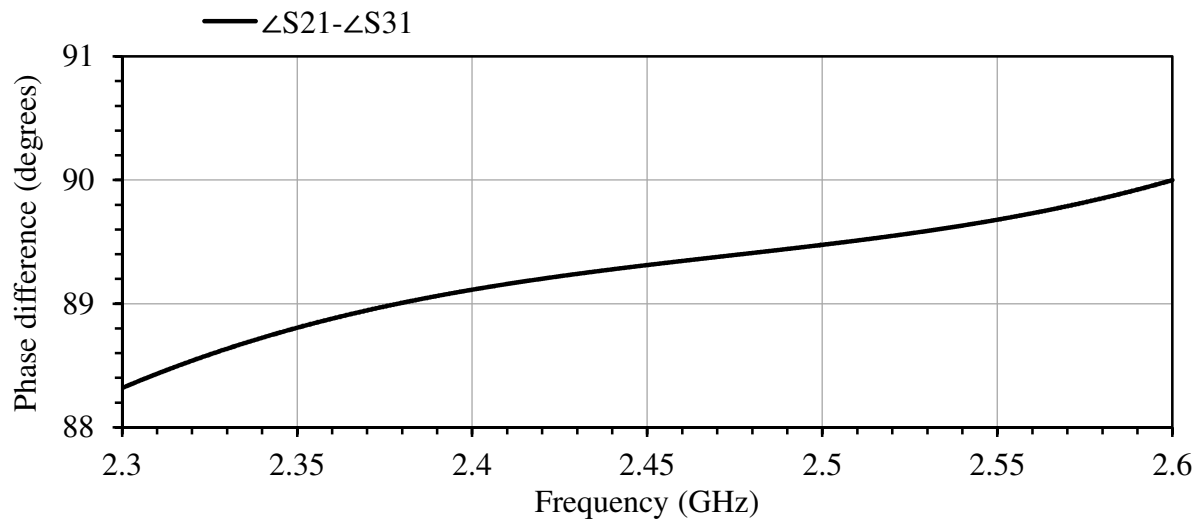


**Figure 3.49.** Phase difference of the branch-line coupler.

### 3.5.2 Dual circular ring-slot antenna loaded with an AMC reflector.

In this section the simulated results of the proposed dual circular ring-slot antenna loaded with an AMC reflector is presented. The dual linear antenna described in Section 3.3.3 (Case 2) was integrated with the branch-line coupler in Section 3.4.1. The microstrip branch-line coupler shown in Section 1.5.1 was placed on top of the center conductor of the ring-slot plane, to feed the two capacitive microstrip feedlines from the inside of the slot, as shown in Figure 3.50. Probe feeds were used to excite the  $50\ \Omega$  microstrip-line inputs of the coupler. The coaxial cables were modelled as conductive cylinders which connected the ground plane of the AMC reflector with the center conductor of the ring-slot radiator and the AMC structure shown in Figure 3.44 was used.

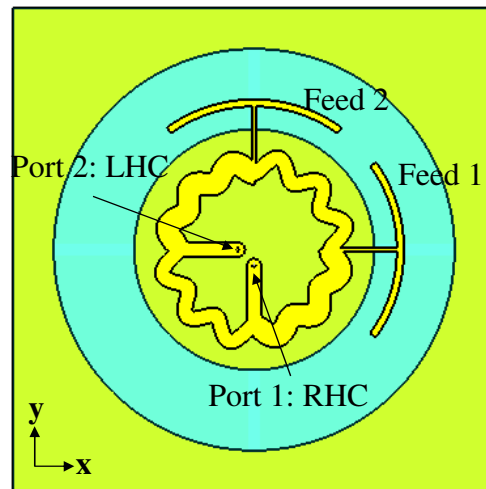


**Figure 3.50.** Dual-feed ring-slot antenna fed with a reduced size branch-line coupler.

When the S-parameters were simulated it was found that the minimum  $S_{21}$  was at slightly lower than 2.45 GHz. To compensate for this the slot length  $l$  was reduced to 125.3 mm. The simulated S-parameters of this implementation is shown in Figure 3.51. The results show a 10 dB isolation bandwidth of 4 % and a return loss of better than -12 dB across the bandwidth of interest. When comparing these results with the S-parameter results for the dual-linear case shown in Figure 3.43, it is clear that the -10 dB input reflection bandwidth approximately corresponds to the 10 dB isolation bandwidth for the dual-circular case and vice versa for the isolation response of the dual-linear antenna.

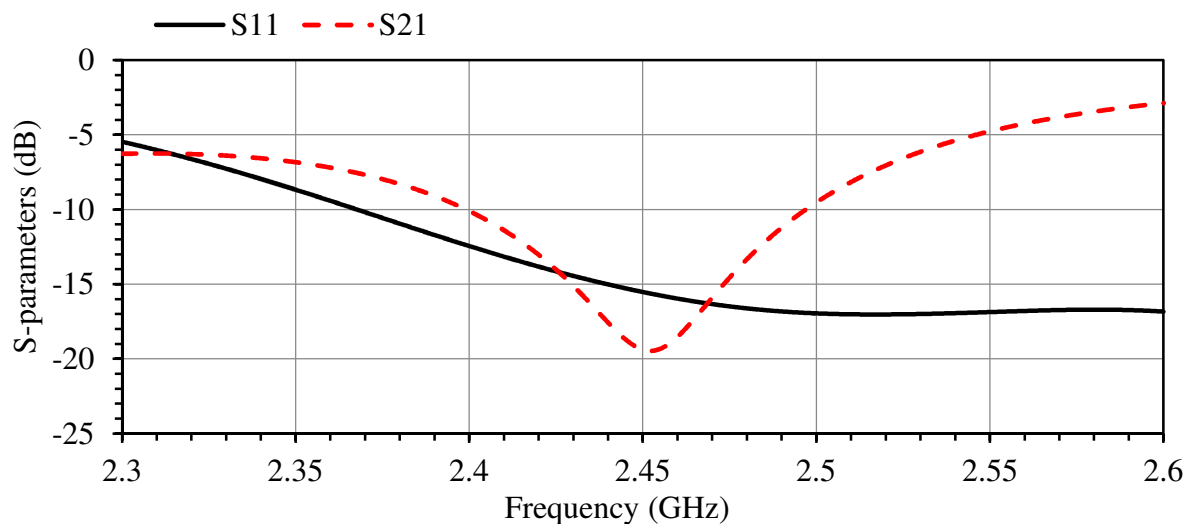


**Figure 3.51.** S-parameters of the dual-circular antenna.

Figure 3.52 shows the radiation patterns in the principle planes for a Port 1 excitation (RHCP). A front-to-back ratio better than 35 dB, and a cross-polarization discrimination of better than 20 dB is observed. Figure 3.53 shows a realized gain greater than 6 dBic in the band of interest with a maximum gain of 6.7 dBic. Figures 3.54 and 3.55 respectively shows how the front-back ratio and the cross-polarization discrimination changes over frequency.

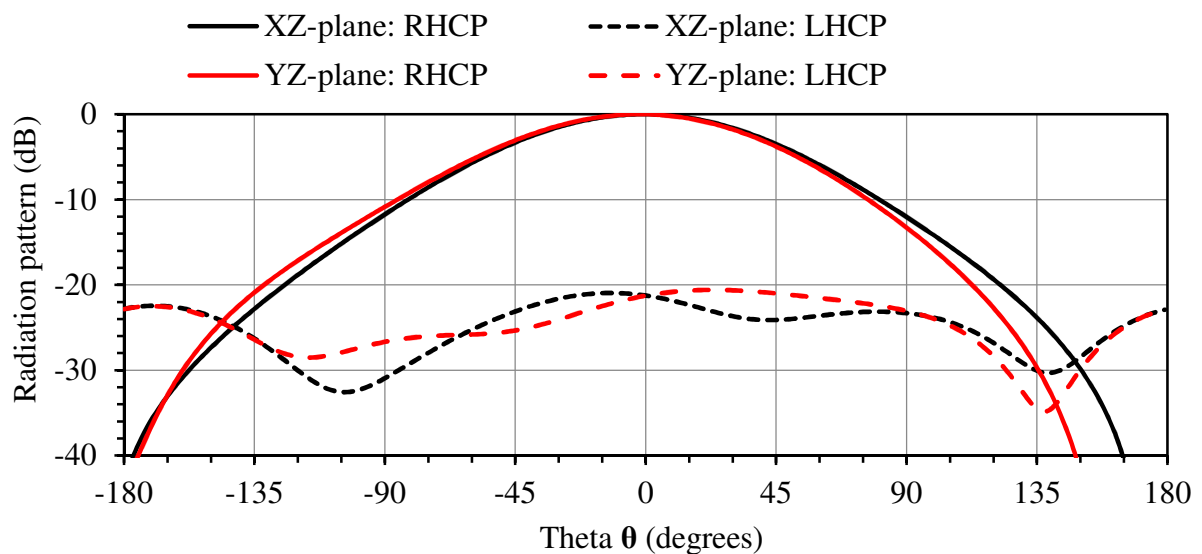


**Figure 3.52.** Radiation patterns at 2.45 GHz for a Port 1 excitation.

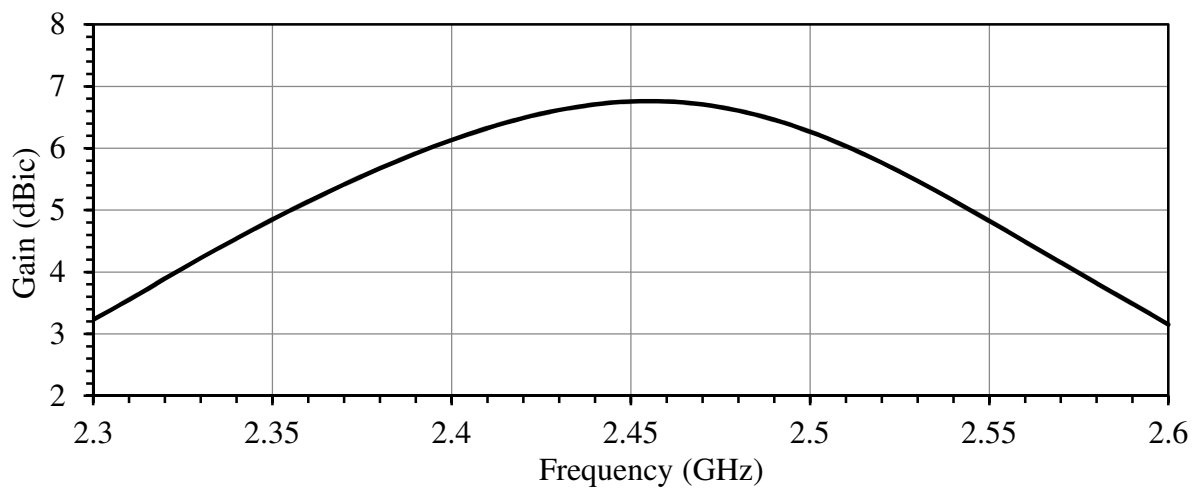


**Figure 3.53.** Bore-sight gain over frequency.

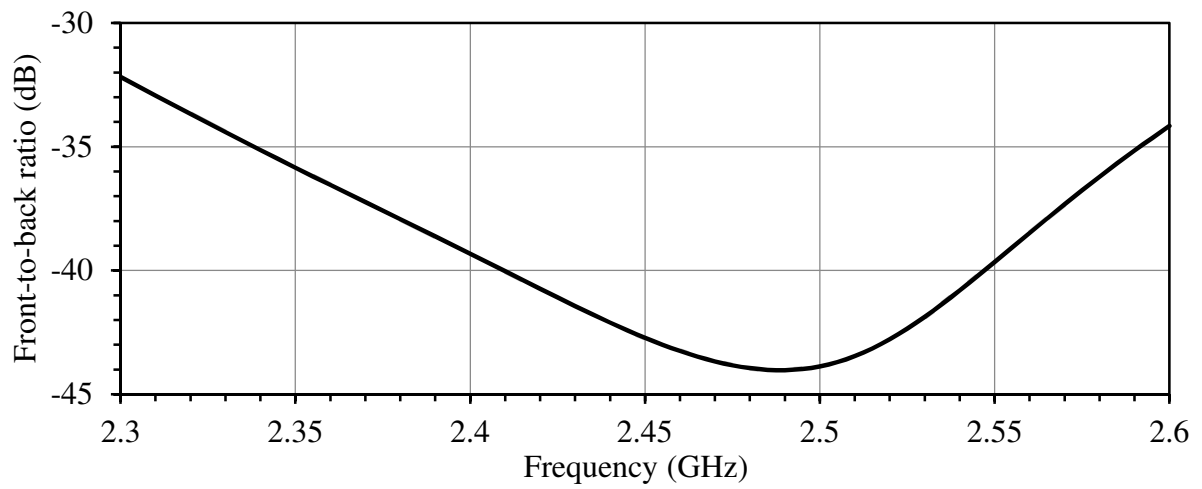


**Figure 3.54.** Front-to-back ratio over frequency.

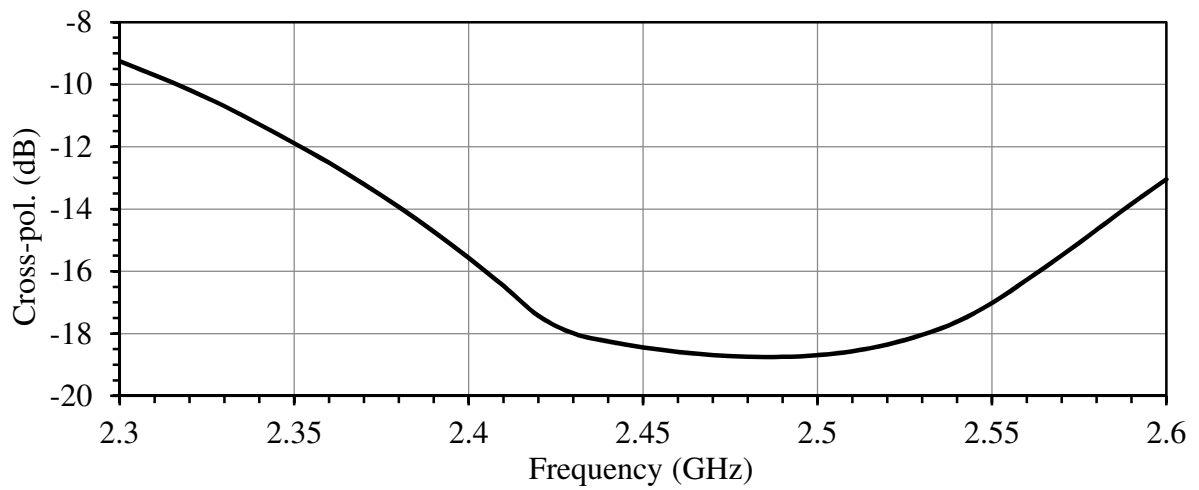


**Figure 3.55.** Cross-polarization discrimination over frequency.

Figure 3.56 shows the axial ratio over angle  $\theta$  for various angles of  $\phi$ . From this data a 3 dB axial ratio beamwidth of around  $90^\circ$  is observed, which corresponds with the 3 dB beamwidth shown in Figure 3.52. The bore-sight axial ratio was found to be better than 3 dB in the bandwidth of interest and the minimum axial ratio was found to be 1.2 dB, as shown in Figure 3.57.

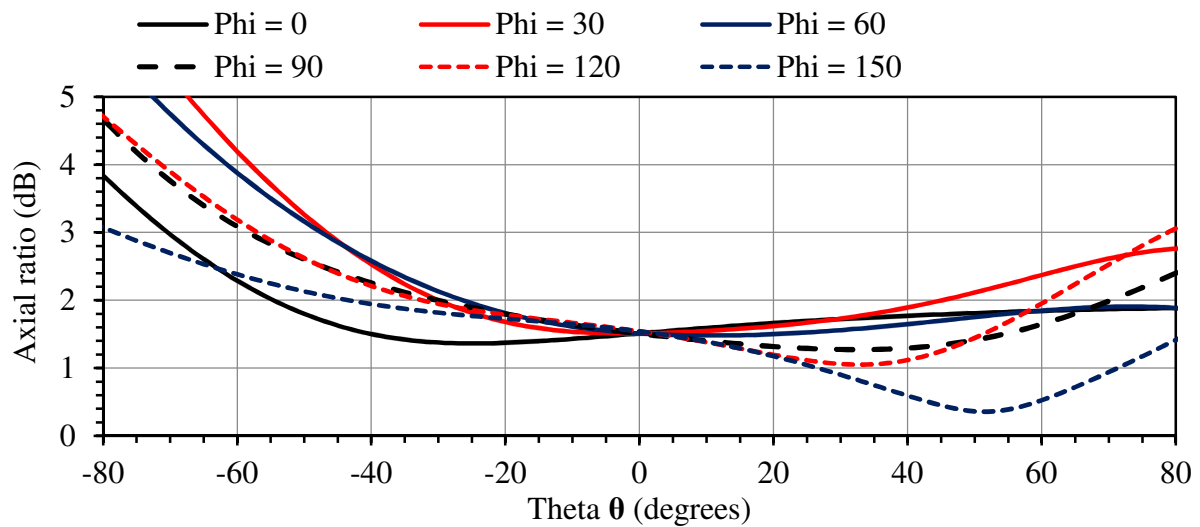


**Figure 3.56.** Axial ratio at 2.45 GHz for a Port 1 excitation.

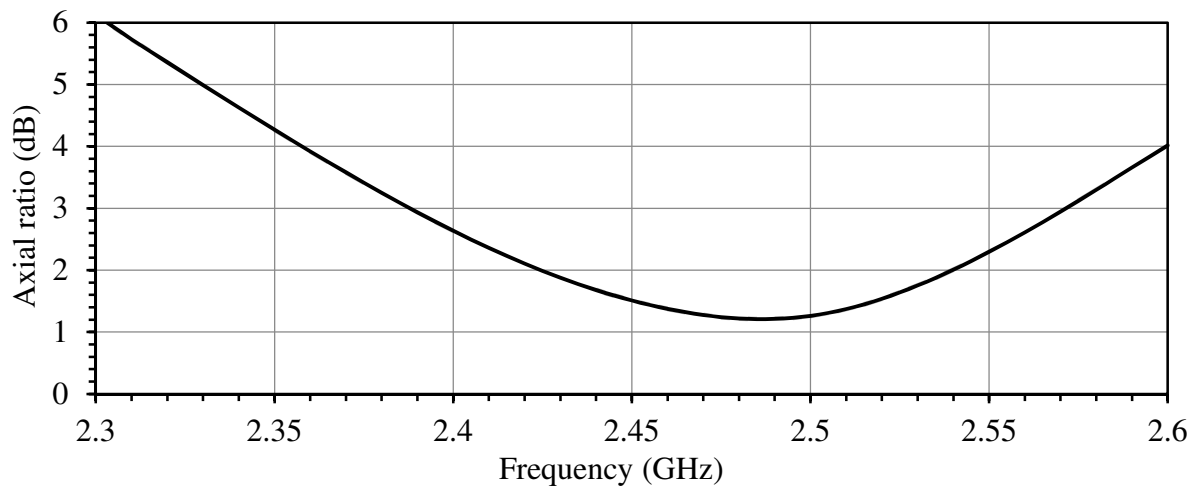


**Figure 3.57.** Bore-sight axial ratio over frequency.

# CHAPTER 4 MEASURED RESULTS

To validate the simulation results from the previous sections, two prototypes were manufactured and measured. The first was based on the CPW-fed ring-slot design presented in Section 3.4.2. The second prototype was based on the dual circularly polarized design presented in Section 3.5.2. The S-parameters of the manufactured prototypes were measured using a calibrated HP8150 VNA. The gain and relative pattern measurements were measured at the Compact Antenna Range of the University of Pretoria.

## 4.1 CPW-FED RING-SLOT ANTENNA

### 4.1.1 Prototype assembly and S-parameter measurements

For the CPW-fed ring-slot antenna loaded with an AMC reflector the 10 mm slot width case (see Table 3.4) which achieved the best front-to-back ratio and cross-polarization was manufactured and measured. Figure 4.1 shows photographs of the manufactured prototype.

The prototype consisted of three single sided PCBs (printed on Rogers RO4003 substrate), where the ring-slot PCB had a height of 0.813 mm and the AMC reflector consisted of two layers of 1.524 mm substrate. The structure was held together at each corner by Teflon fasteners, and a 3 mm spacers (also Teflon) was placed in between the ring-slot and AMC reflector. The plastic fasteners also ensured that no air gap in between the AMC PCBs were present.

To compensate for the mounting holes in the structure, the dimensions of the AMC was changed to  $a = 25.5$  mm and  $s = 1.3$  mm. The manufactured prototype resonated at 2.43 GHz, which is approximately 1% below the design center frequency of 2.45 GHz. It is suspected that this difference is mainly due to the relative permittivity  $\epsilon_r$  tolerances of the substrate. The antenna was experimentally tuned (using copper tape) by increasing angle  $\theta$  slightly. A comparison between the simulated and measured reflection coefficient (before and after the angle  $\theta$  was tuned) of the antenna is shown in Figure 4.2.

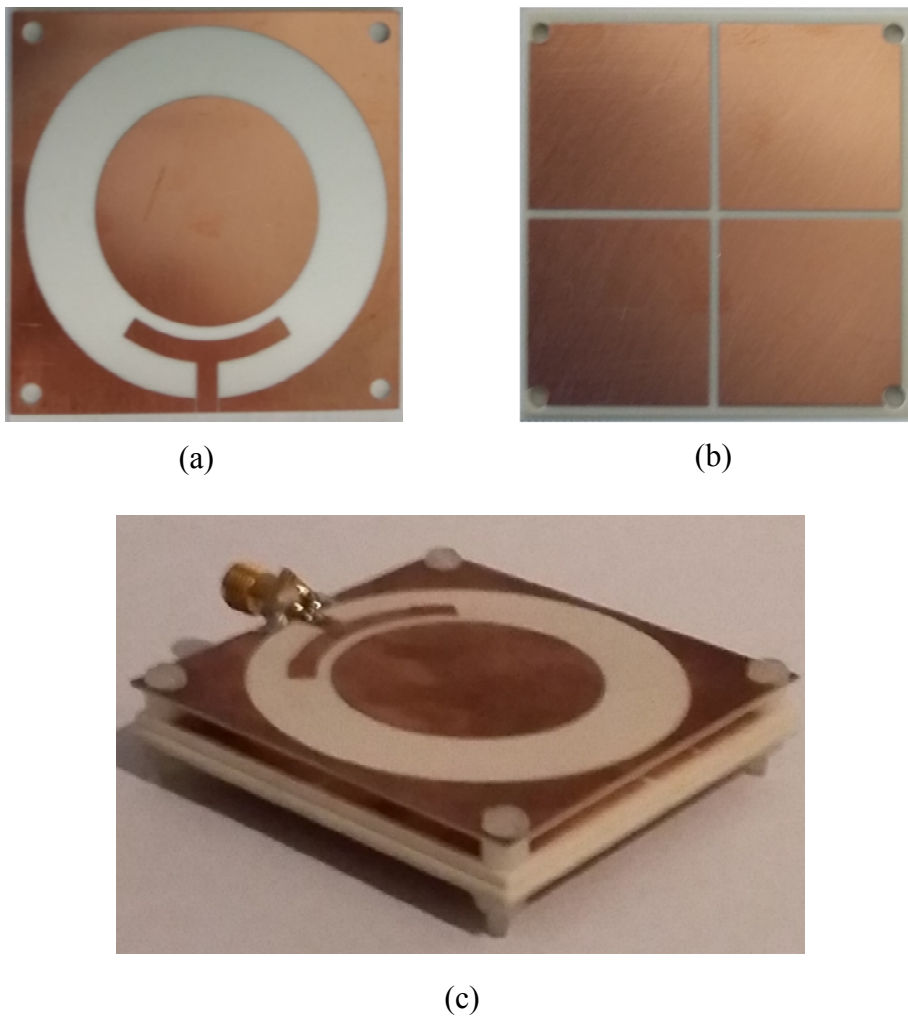


**Figure 4.1.** CPW-fed ring-slot antenna prototype: (a) top view of ring-slot PCB, (b) top view of AMC reflector PCB, (c) assembled prototype with angle  $\theta$  adjustment.

The reflection coefficient data shows that the response of the simulated and the measured data is similar, although the measured data is shifted lower in frequency. The measured data after the adjustment shows a slightly different response, where the minimum return loss being lower. This due to the fact that adjusting the angle  $\theta$  only changes the imaginary part of the impedance is changed. When a larger frequency adjustment is desired other parameters also needs to be adjusted. The sets of data correspond well, with suitable impedance bandwidth (approximately 5.5%) to operate satisfactorily in the 2.4 GHz WLAN frequency band.

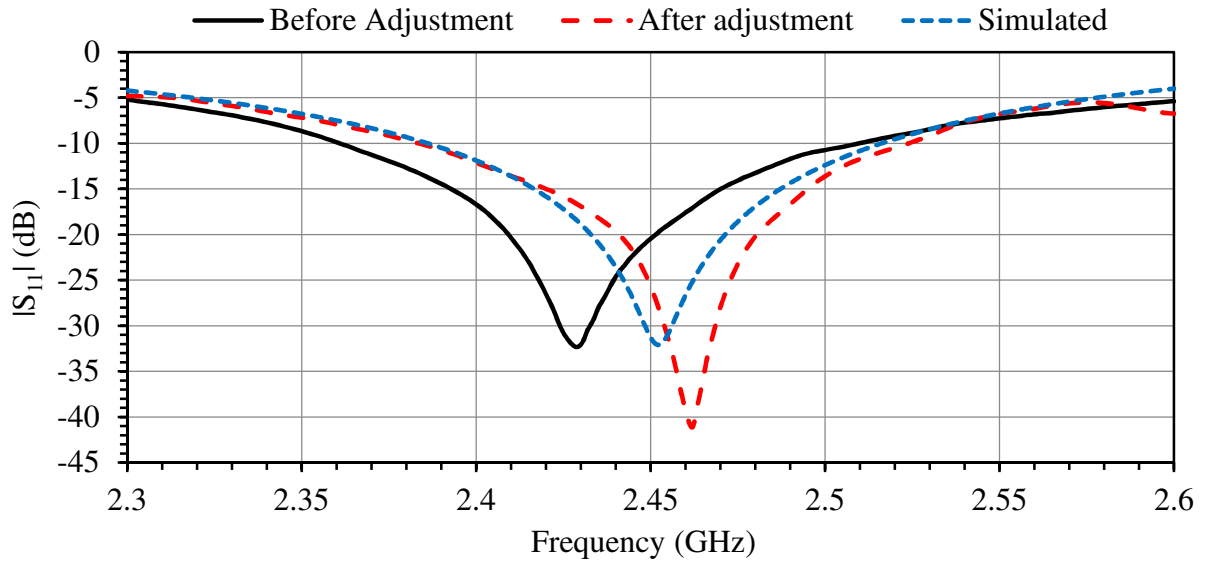


**Figure 4.2.** Simulated and measured S-parameter results.

#### 4.1.2 Realized gain and radiation pattern measurements

For the adjusted prototype, the realized gain as well as the E- and H-plane radiation patterns were measured. A simplified representation of the measurement setup inside the Compact Antenna Range is shown in Figure 4.3. The horn antenna at the focus point of the reflector was used as the source, while the device under test (DUT) was used as the receiver.

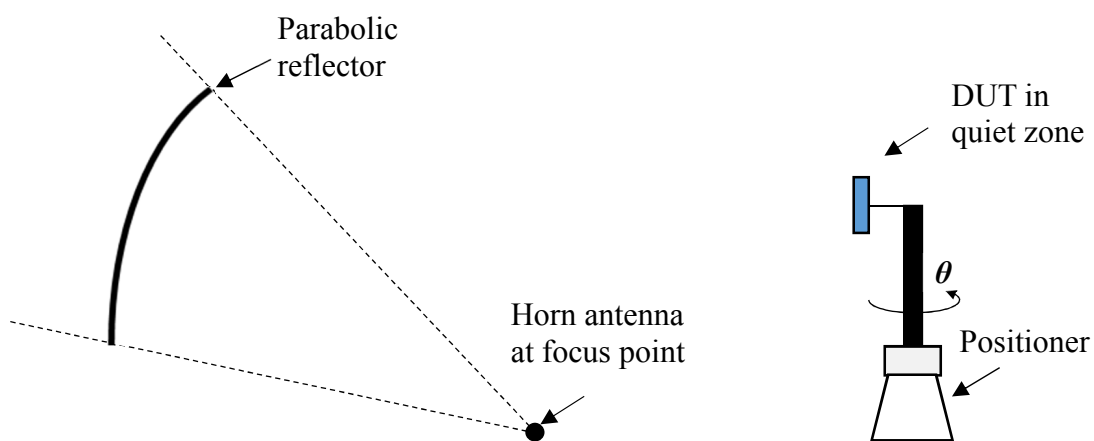


**Figure 4.3.** Gain measurement setup at the Compact Antenna Range.

The pattern measurements involved four azimuth sweeps measuring the co-polarizations and cross-polarizations in both the E- and the H-plane. The radiation patterns were measured at 2.45 GHz, and the data is shown in Figure 4.4 and Figure 4.5 respectively. The cross-polarization in the E- and H-plane was found to be better than 20 dB. The measured front-to-back ratio was found to be 15 dB which is significantly less than the expected 27 dB from the simulated results. It is suspected that this is due to coupling between the coaxial cable used to feed the CPW-line and the open cavity AMC structure.

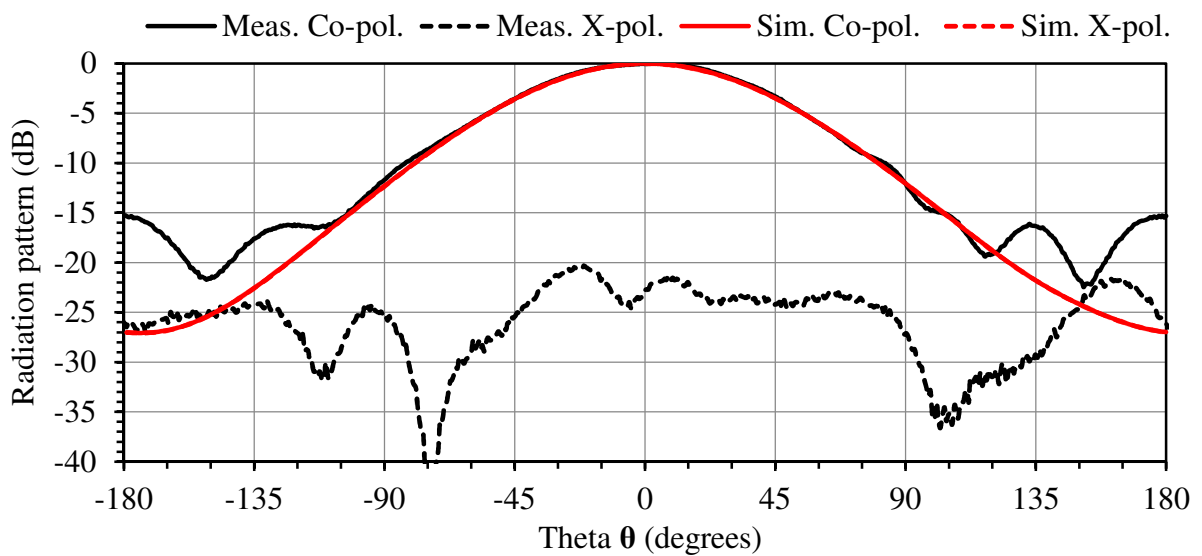


**Figure 4.4.** Simulated and measured E-plane radiation patterns at 2.45 GHz.

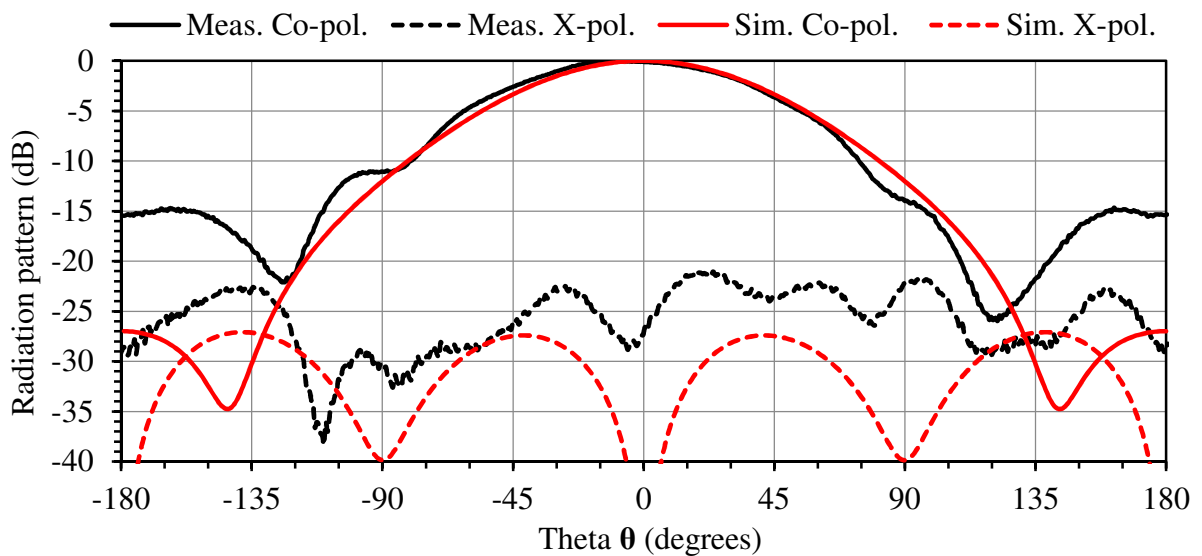


**Figure 4.5.** Simulated and measured H-plane radiation patterns.

In order to determine the realized gain, the co-polarization of the prototype was measured at the boresight position, over a frequency range of 2.3 GHz to 2.6 GHz. The prototype was then replaced with a reference horn antenna of which the gain is accurately known. The data was captured and the realized gain was calculated as shown in Equation (4.1), which states that the realized gain is equal to the through measurement ( $S_{21}$ ) of the DUT divided by the through measurement of the reference antenna and multiplied by the known realized gain data of the reference antenna. Note that the same coaxial cable was used for both measurements. Figure 4.6 shows that the simulated and measured gain compares well in the bandwidth of interest. A gain of better than 6.5 dBi was achieved across the 5.5 % bandwidth.

$$G_{realised} = \frac{|S_{21}|_{DUT}}{|S_{21}|_{ref}} \cdot G_{ref} \quad (4.1)$$

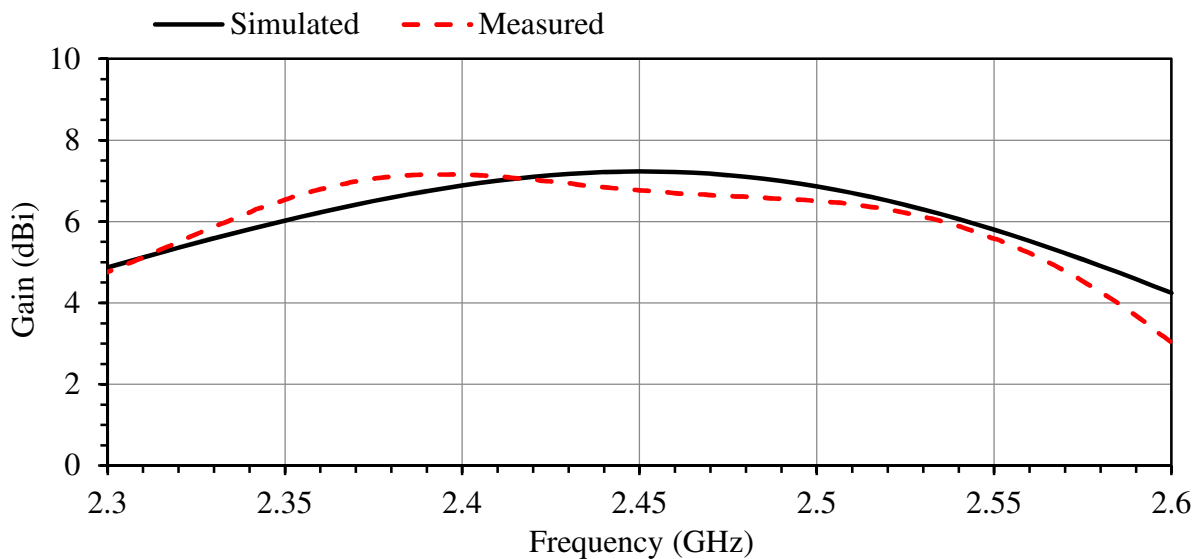


**Figure 4.6.** Simulated and measured bore-sight gain.

## 4.2 DUAL-CIRCULARLY POLARIZED RING-SLOT ANTENNA

### 4.2.1 Prototype assembly and S-parameter measurements

The dual circularly polarized antenna described in Section 3.5.2 was also manufactured and measured to validate the theory. The manufactured PCBs are shown in Figure 4.7. The assembly of the prototype was similar to that described in Section 4.1 with the notable difference of the addition of coaxial cables (SUCCOFORM SM 86) that were used as feeds to the branch-line coupler. For ease of manufacturing the length of the coaxial cables were chosen as  $\sim 7.5$  cm. The coax cables was fed through holes in the AMC structure (see Figure 4.7c). The inner conductors of the cables were fed through the small holes connecting to the microstrip lines and soldered at the top (see Figure 4.7a). The outers of the cables were soldered to the center conductor of the ring-slot (see Figure 4.7b). The assembled prototype is shown in Figure 4.8a.

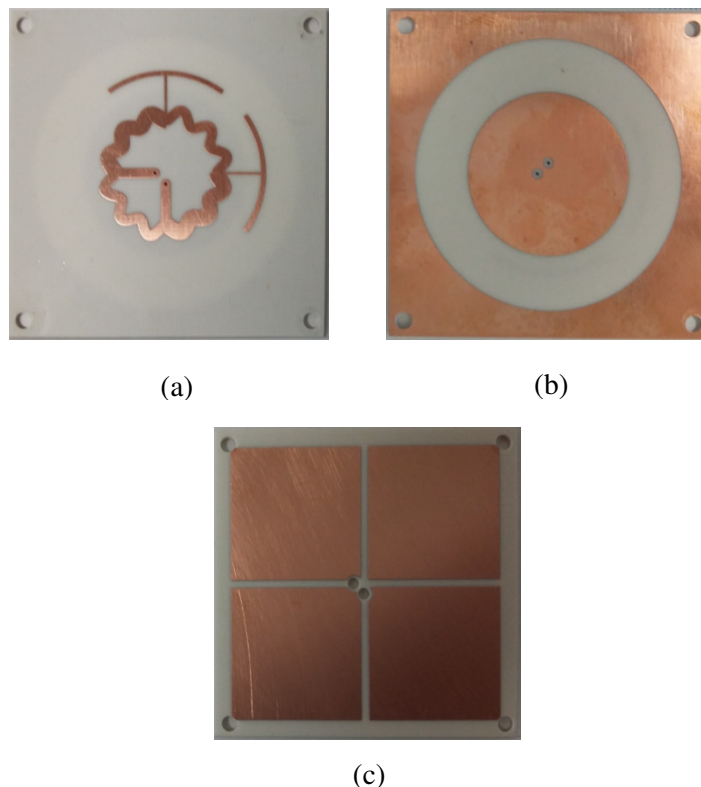


**Figure 4.7.** Manufactured PCBs: (a) top view of the ring-slot PCB, (b) bottom view of the ring-slot PCB, (c) top view of the AMC reflector PCB.

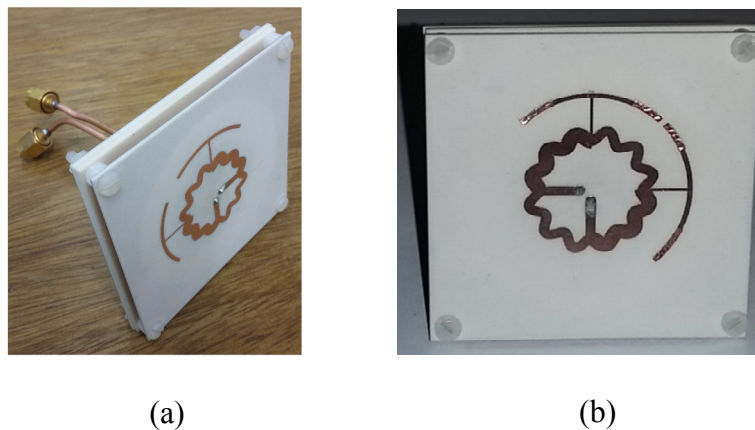


**Figure 4.8.** Dual-circularly polarized antenna prototype: (a) before adjustment, (b) after adjustment.

The S-parameters of the prototype before adjustment is shown in Figure 4.9. The prototype showed optimum isolation between the two ports at 2.4 GHz. The antenna was experimentally tuned, using copper tape, by effectively increasing angle  $\theta$  for both the ports. For the tuned antenna the optimum isolation shifted to 2.423 GHz.

A comparison between the simulated S-parameters and measured S-parameters of the adjusted antenna is shown in Fig. 4.10. A 10 dB isolation bandwidth of 4% was achieved. The measured return loss of the two ports differed somewhat from each other, but still better than 10 dB across an almost 12% bandwidth.

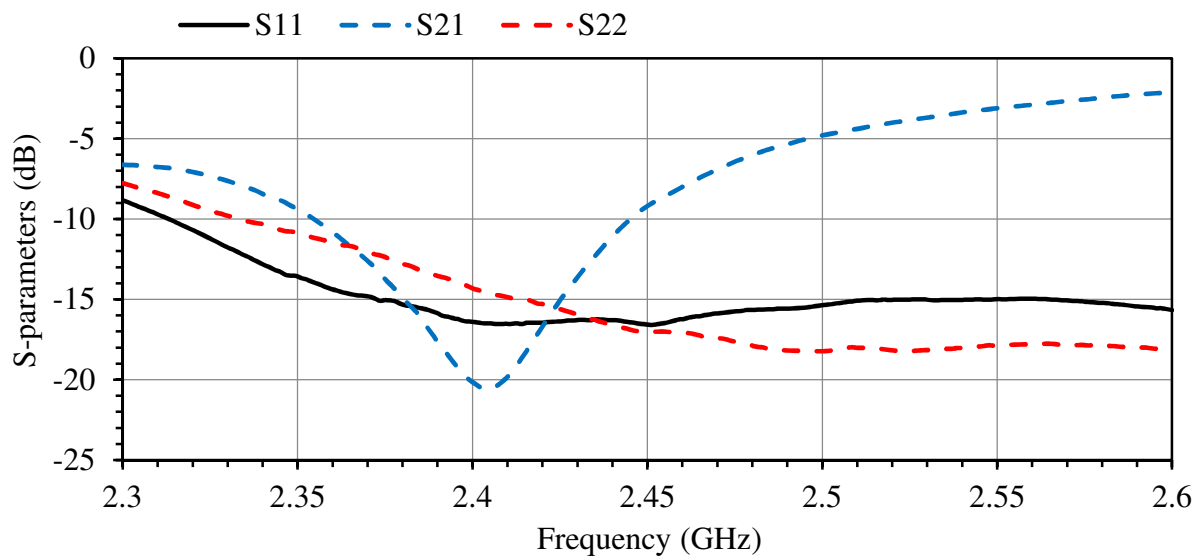


**Figure 4.9.** Measured S-parameter results before adjustment.

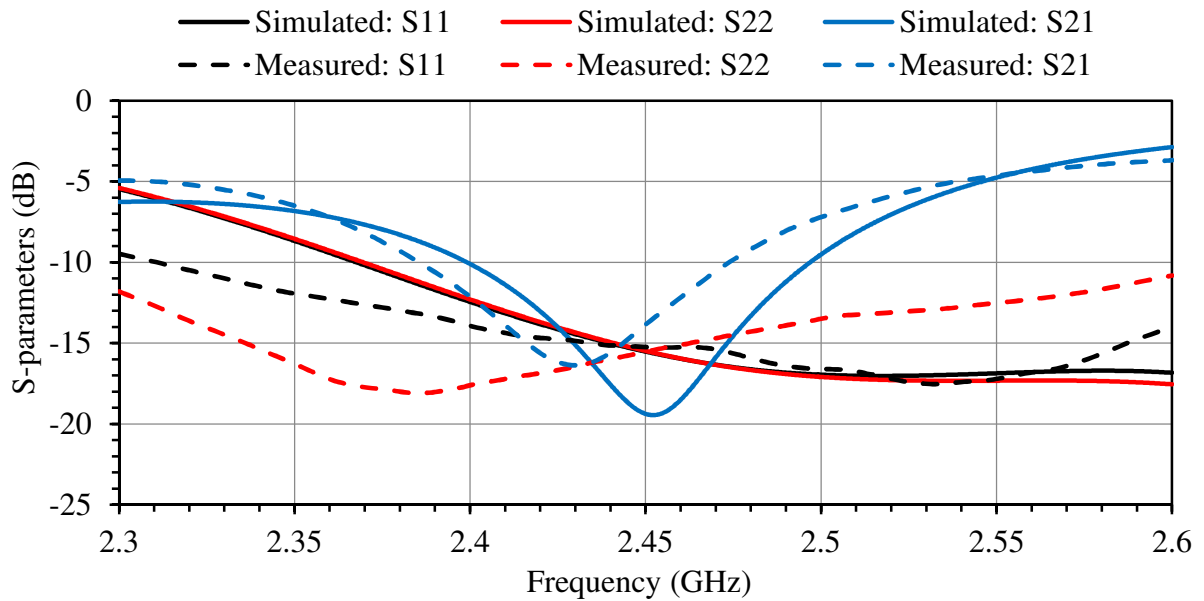


**Figure 4.10.** Simulated and measured S-parameter results after adjustment.

#### 4.2.2 Realized gain and radiation pattern measurements

The measurement of the radiation patterns and the gain for both ports were performed in a similar way to the method described in Section 1.1.2, where the radiation patterns were measured in the XZ- and the YZ-plane, as defined in Figure 4.12. Figure 4.13 shows a photograph of the prototype inside the compact range.

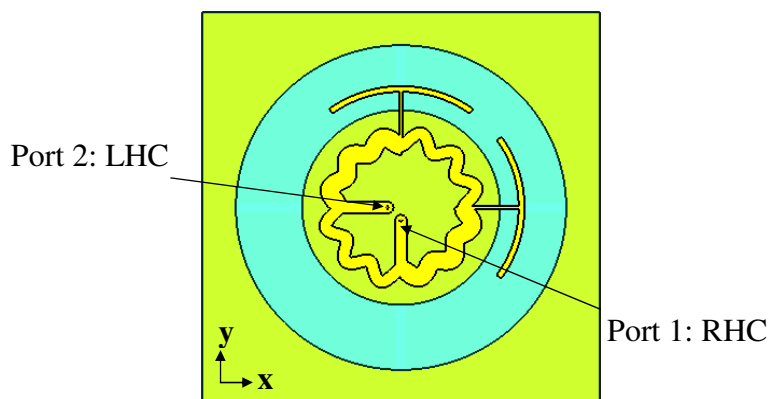


**Figure 4.12.** Diagram showing how the ports and axis were defined for the measurement.

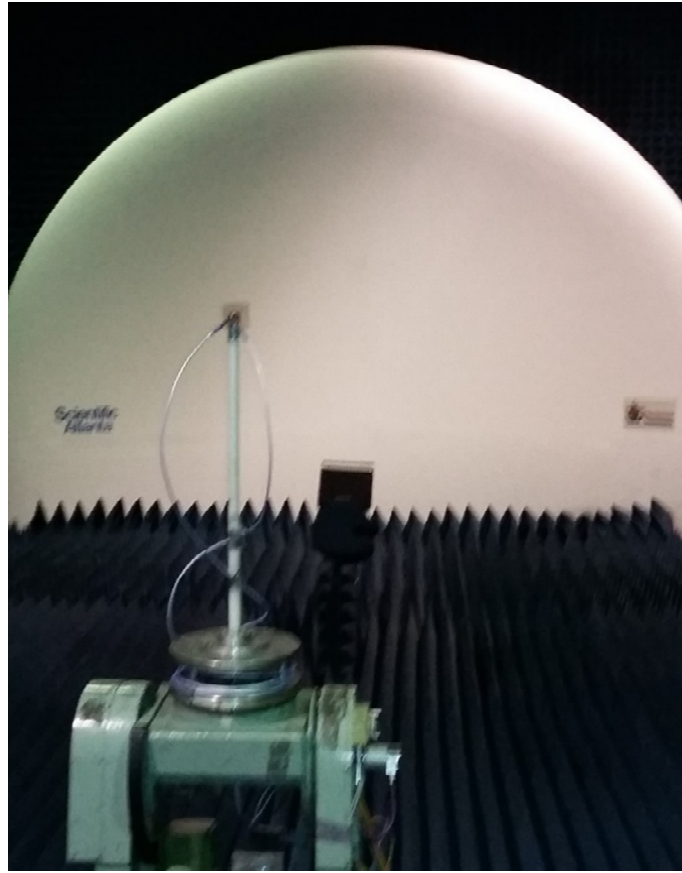


**Figure 4.13.** Antenna under test in the Compact Range.

The linear polarization gain data (dBi) was converted to circularly polarized gain (dBic) by using Equations (4.2) and (4.3), where  $G_{HP}$  and  $G_{VP}$  refers to the horizontal and vertical realized gain. Note that it does not matter if the source antenna is rotated  $+90^\circ$  or  $-90^\circ$  degrees in order to change between horizontal and vertical polarization, as long as it done in a consistent way as to avoid an 180 phase inversion, which will result in an inverted circular polarization sense that will be calculated.

$$\text{Re}\{G_{RHSP}\} = \text{Im}\{G_{LHSP}\} = \frac{(\text{Re}\{G_{HP}\} + \text{Im}\{G_{VP}\})}{\sqrt{2}} \quad (4.2)$$

$$\text{Im}\{G_{RHSP}\} = -\text{Re}\{G_{LHSP}\} = \frac{(\text{Im}\{G_{HP}\} - \text{Re}\{G_{VP}\})}{\sqrt{2}} \quad (4.3)$$

Figures 4.14 and 4.15 shows the simulated and measured radiation patterns for Port 1 and Port 2 in the XZ-plane and the YZ-plane. A front-to-back ratio and cross-polarization of 25 dB and 18 dB were achieved respectively. The simulated and measured gain of the antenna is shown in Figure. 4.15. A maximum gain of 7.4 dBic and 6.8 dBic was measured for port 1 and port 2 respectively. The measured gain was better than 6.3 dBic was achieved across the 4% isolation bandwidth.

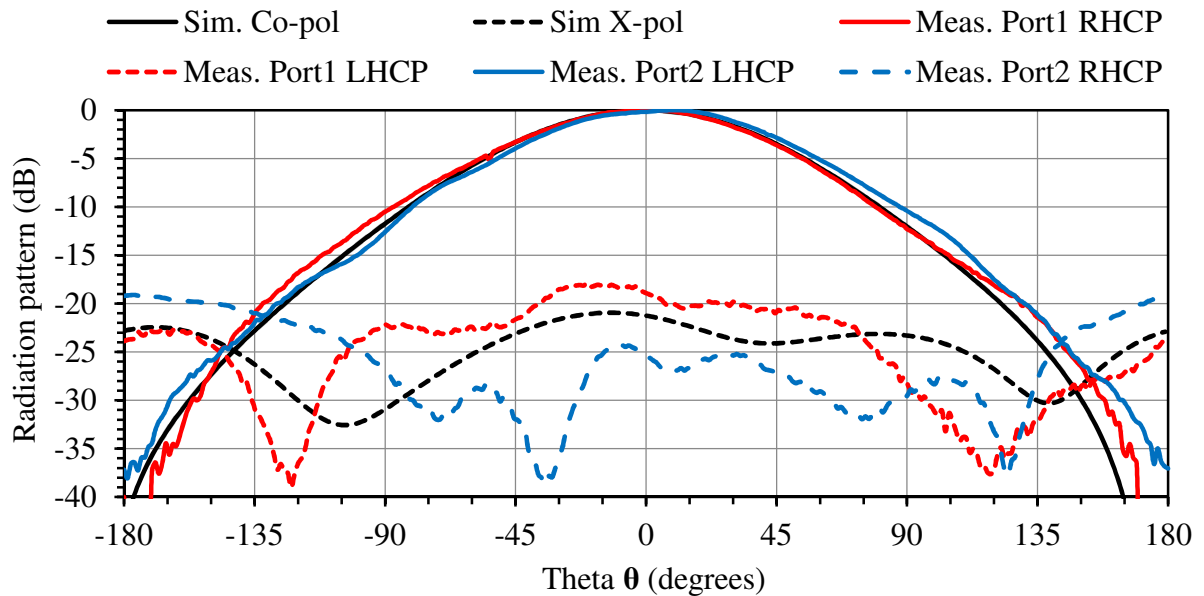


**Figure 4.14.** Simulated and measured radiation patterns at 2.45 GHz, where Port 1 and Port 2 were measured in the XZ-plane and the YZ-plane, respectively.

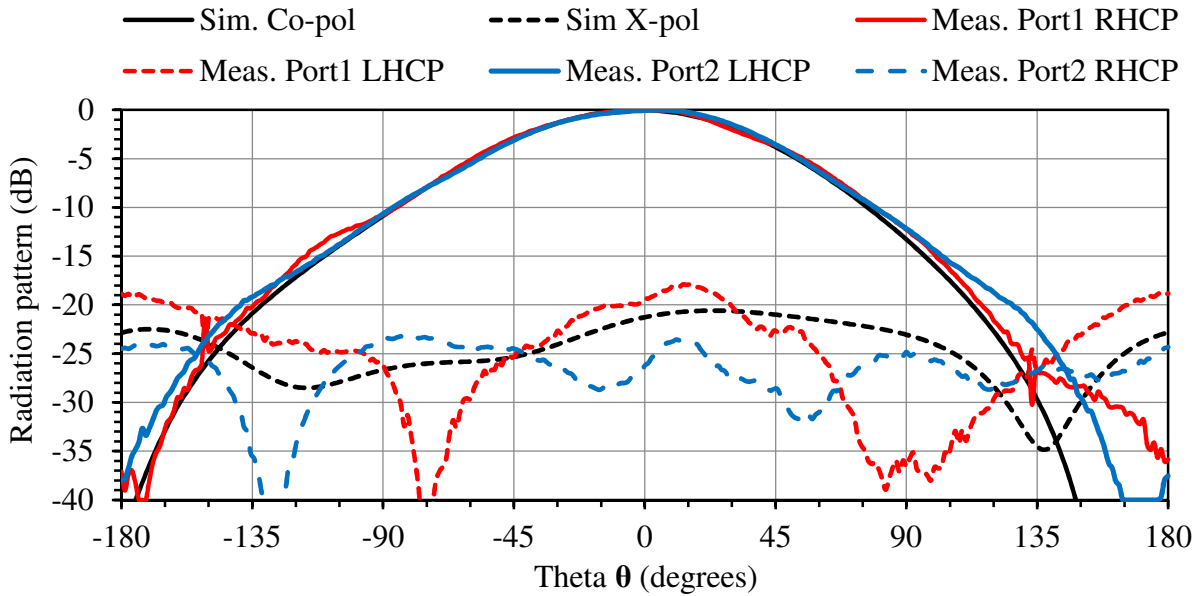


**Figure 4.14.** Simulated and measured radiation patterns at 2.45 GHz, where Port 1 and Port2 were measured in the YZ-plane and the XZ-plane, respectively.

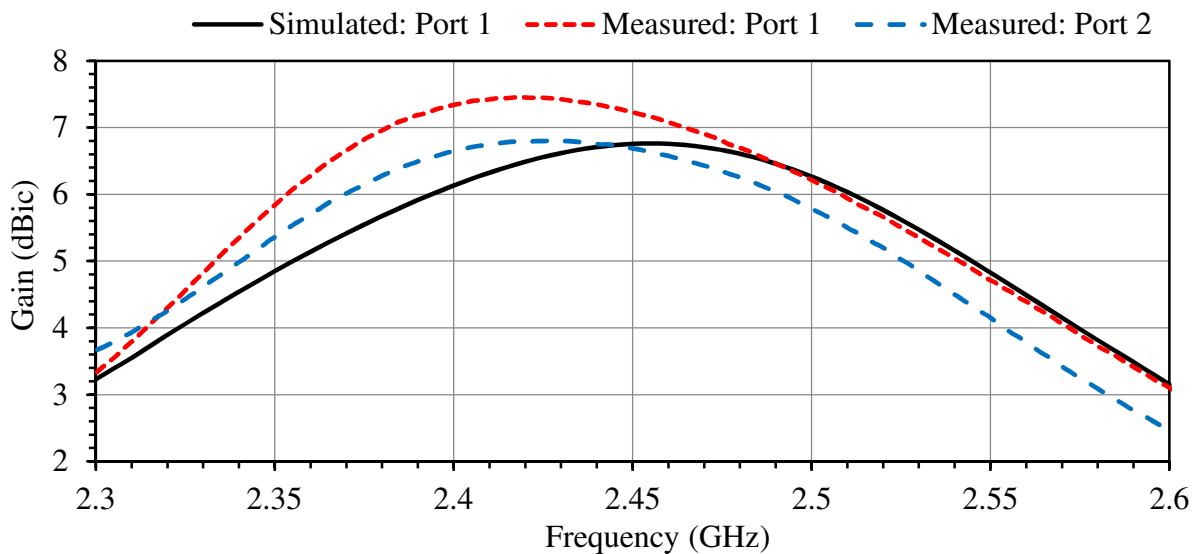


**Figure 4.15.** Simulated and measured bore-sight gain over frequency.

### 4.2.3 Axial ratio measurements

The purpose of the axial ratio measurements was to determine how good the axial ratio is within the main beam of the antenna and to determine the axial ratio bandwidth. The measurement setup used to measure the axial ratio is shown in Figure 4.16. The positioner

was setup in such a way that the prototype could be rotated in both the Theta  $\theta$  and the Phi  $\phi$  angles, as indicated in Figure 4.16.

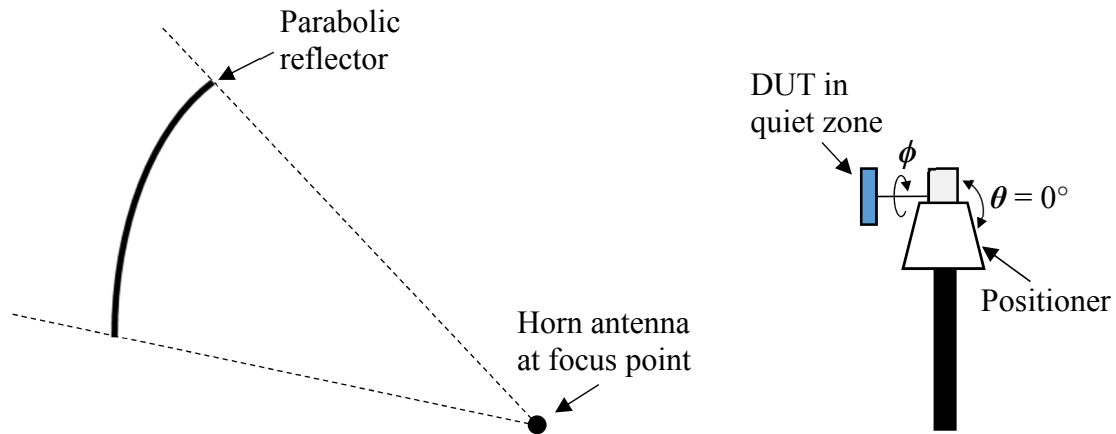


**Figure 4.16.** Axial ratio setup at the Compact Antenna Range.

In order to determine the axial ratio beam-width, the positioner was set up to start at the position  $(\theta, \phi) = (-80^\circ, 0^\circ)$ . The prototype was spun  $360^\circ$  in the Phi  $\phi$  direction, while taking several measurements at 2.45 GHz. The process was then repeated for several incremental steps in the  $\theta$  angle until an angle  $+80^\circ$  was reached. The axial ratio was determined by dividing the maximum by the minimum measured data for each  $\theta$  angle. The measured axial ratio over angle theta results are shown in Figure 4.17. The resulting 3 dB axial ratio was achieved over a beam width of  $110^\circ$ . Figure 4.18 shows the bore-sight axial ratio over frequency. The measured axial ratio was better than 3 dB over a bandwidth of 4.7%.

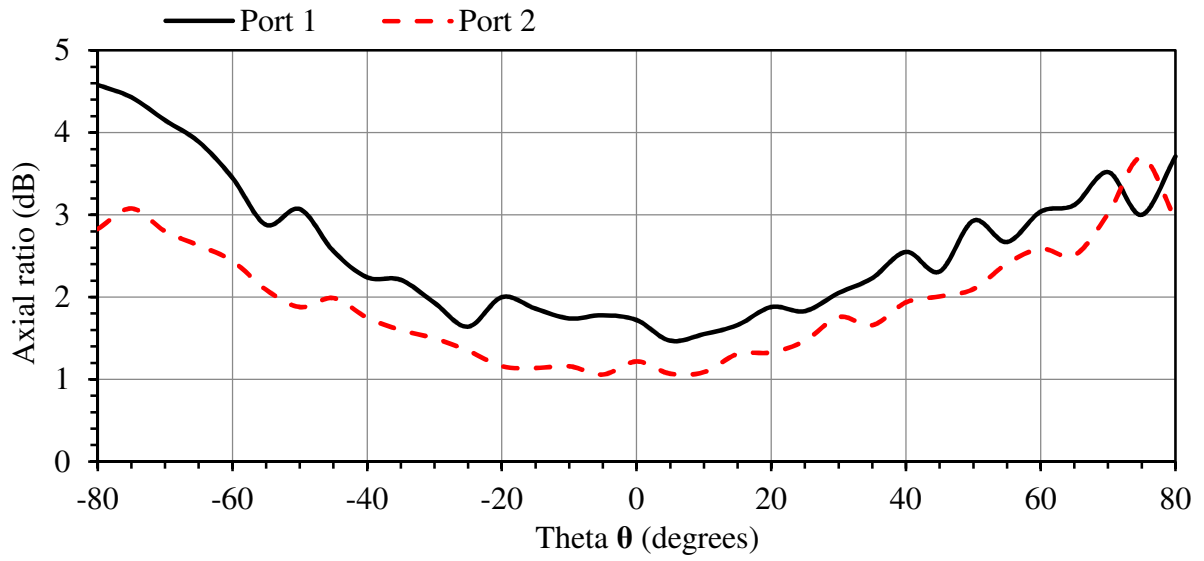


**Figure 4.17.** Measured axial ratio at 2.45 GHz of the dual-feed antenna in the YZ-plane.

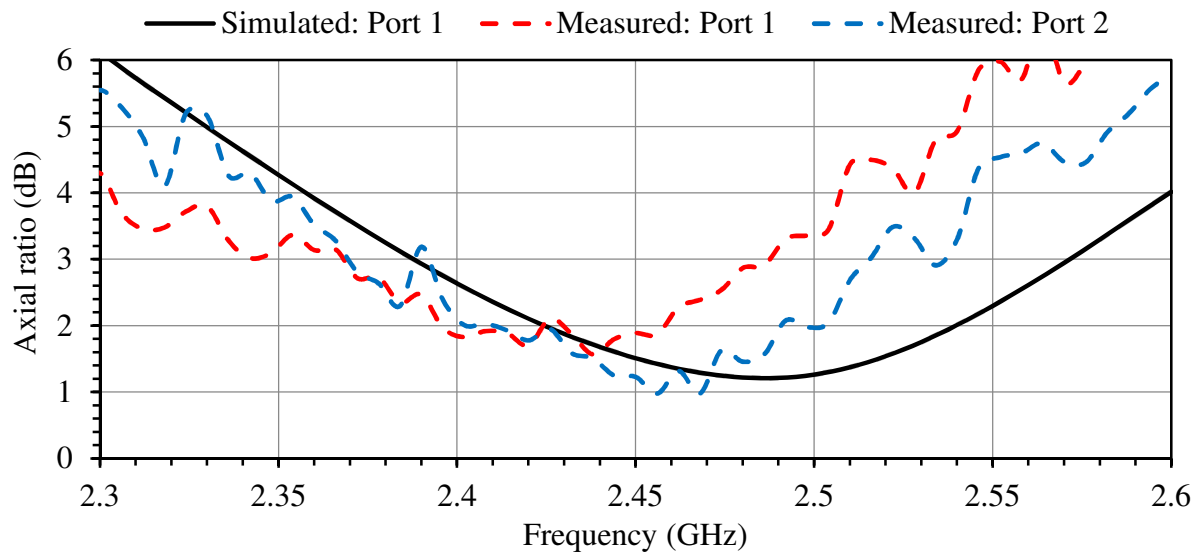


**Figure 4.18.** Measured bore-sight axial ratio over frequency.

# CHAPTER 5 CONCLUSION

## 5.1 SUMMARY OF WORK

In the literature study presented in Chapter 2, various aspects relating to the proposed design were investigated. In order to achieve uni-directional radiation patterns, metamaterial reflectors were investigated. It was found that these kinds of structures could significantly reduce the overall height of an antenna. It was also found that these structures can also offer significantly improved front-to-back ratios, albeit only over a limited bandwidth. Various antenna geometries were investigated namely: curl antennas, dipoles, monopoles, patch antennas, and slot antennas. The ring-slot geometry was found to be a compact structure which can achieve a fairly high impedance bandwidth when a capacitive feed network is used. The literature study also showed that ring-slot antennas are versatile structures that can be implemented to have both frequency and polarization diversity [14, 27, 50, 52]. In the literature study various dual-circularly polarized antennas were compared in terms of their size and performance. The literature study concluded with some background knowledge and possible benefits of the proposed dual-circularly polarized antenna design.

In Chapter 3 a simulation study was performed to investigate various aspects relating to the design of a dual-circularly polarized cavity-backed ring-slot antenna loaded with an AMC reflector. This investigation was performed through various CST simulations. Both CPW and microstrip feeding structures were investigated. It was found that the addition of a capacitive feed network can improve the impedance bandwidth without increasing the overall size of the antenna. A dual capacitive feed configuration was also investigated and it was found to work well as a feed for a dual-linearly polarized antenna. The square patch AMC reflector was analyzed using both CST simulations and the theory described in [26, 28]. The analysis shows that the bandwidth of the AMC reflector is mainly determined by the height of the structure, while the permittivity of the material and the choice in gap spacing determines the minimum size of the AMC unit cell. The rest of the chapter focused on the design of two cavity-backed ring-slot antennas loaded with AMC reflectors, the first of which was a linearly polarized capacitively-fed CPW ring-slot antenna and the second was a dual-circularly polarized ring-slot antenna.

Based on the design of the ring-slot cavity-backed antennas loaded with AMC reflectors in Chapter 3, two prototypes were manufactured and measured. The results are shown in Chapter 4. The S-parameters of the prototypes differed slightly from the simulation results, which shows that the simulation model requires some adjustment. Both the radiation patterns and the realized gain were measured in the Compact Range at the University of Pretoria. For the case of the CPW-fed ring-slot antenna the measured front-to-back ratio was significantly lower than what was achieved in simulation. It is suspected that this is due to coupling between the coaxial cable used to feed the CPW-line and the open cavity AMC structure. Chapter 4 also shows how the measurements were performed and how the measured data was processed. The results were found to be in good agreement with the simulated results.

## 5.2 CONTRIBUTIONS

The proposed dual-circularly polarized antenna is a novel extension of the single polarized antennas proposed in [23, 27]. In order to achieve a unidirectional radiation pattern, the cavity-backed ring-slot radiator was loaded with an AMC reflector, which consisted of a  $2 \times 2$  patch array. The two capacitive feeds were connected to a reduced size branch-line coupler proposed by Joubert et al. [29]. This coupler was placed over the center conductor of the ring-slot and was fed with two coaxial lines through the back of the cavity.

As a first prototype a CPW ring-slot radiator with a linear polarization with an AMC reflector was also analyzed and manufactured. This prototype used a capacitive feed structure similar to that used in [27]. Experimental results for the final antenna design with a size of  $0.457\lambda_0 \times 0.457\lambda_0 \times 0.056\lambda_0$  exhibits a 5.5% impedance bandwidth, maximum gain of approximately 7 dBi, a front-to-back ratio of 15 dB, and good cross-polarization.

The end result and contribution of the research presented in this work is a very low profile and small footprint antenna with reasonable gain and bandwidth, with two ports for dual-circular polarization operation, and very good front-to-back ratio and cross-polarization. Only a few dual-circularly polarized antennas have been reported in literature [2 – 10]. These antennas have been shown to either have low front-to-back ratios, low cross-pol

discriminations or they are large in terms of overall size. A comparison with results achieved by other dual-circularly polarized antennas is presented in Table 5.1. From the table, it is clear that the newly proposed antenna has a significantly better front-to-back ratio, good gain and reasonable bandwidth for its size. Note that the fractional bandwidth in Table 5.1 was defined as the bandwidth over which the return loss and isolation were better than 10 dB, as well as an axial ratio better than 3 dB. To the author's knowledge this is the smallest dual-circularly polarized antenna published up to date that has a suitable bandwidth for use in 2.4 GHz wireless local area network (WLAN) communication systems.

**Table 5.1.** Comparison of dual-circularly polarized antennas.

Ref.	Size ( $\lambda_0$ )	Eff. band. (%)	Gain (dBic)	Cross-pol. (dB)	F/B ratio (dB)
[2]	0.8×0.8×0.125	16	7	13	15
[3]	0.73×0.7×0.013	3.5	6	10	10
[4]	1.62×0.82×0.017	1.5	5	10	10
[5]	0.73×0.73×0.067	3.5	6	11	16
[6]	0.82×0.82×0.15	5	4	-	-
[7]	0.94×0.94×0.189	16	9	17	13
[8]	1.8×1.35×0.056	15	10	15	18
[9]	0.85×0.85×0.28	8.5	7	10	10
[10]	0.5×0.5×0.025	1	-	15	15
This work	0.5×0.5×0.067	4	6	18	>30

### 5.3 FUTURE WORK

The current design only achieved a 10 dB isolation bandwidth of 4%, which is undesirable for many applications. This narrow isolation bandwidth was shown to be due to the limited bandwidth of the AMC reflector. Future work may include finding a way to improve the isolation without having to increase the height of the AMC structure. One possible solution would be to use dual L- or V- shaped feeds that are designed to have opposite circular

polarization sense, where each feed is excited via a transmission line [15, 50]. This type of implementation could have significantly higher isolation at the cost of a narrower impedance bandwidth, due to the resonant nature of an AMC reflector.

Antennas used in WLAN application are often multiband in order to operate in all the commonly used bands such as 2.4 GHz, 5.2 GHz, and 5.8 GHz. Both ring-slot antennas and AMC reflectors have been shown to work in multiband applications [25, 27, 35]. Future work might also include the design of a multiband compact polarization diverse ring-slot antenna with unidirectional radiation patterns.

## REFERENCES

- [1] L. Bernard, G. Chertier and R. Sauleau, "Wideband circularly polarized patch antennas on reactive impedance substrates," *IEEE Antennas and Wireless Prop. Letters*, vol. 10, pp. 1015-1018, 2011.
- [2] J. Wu, H. Yang and Y. Yin, "Dual circularly polarized antenna with suspended strip line feeding," *Progress In Electromagnetic Research C*, vol. 55, pp. 9-16, 2014.
- [3] A. Narbudowicz, X. Bao and M.J. Ammann, "Dual circularly-polarized patch antenna using even and odd feed-line modes," *IEEE Trans. Antennas and Propagation*, vol. 61, no. 9, pp. 4828-4831, 2013.
- [4] G.Q. Luo and L.L. Sun, "A reconfigurable cavity backed antenna for circular polarization diversity," *Microwave and Optical Tech. Letters*, vol. 51, pp. 1491-1493, 2011.
- [5] X.-Z. Lai, Z.-M. Xie, Q.-Q. Xie and X.-L. Cen, "A dual circularly polarized RFID reader antenna with wideband isolation," *IEEE Antennas and Wireless Prop. Letters*, vol. 12, pp. 1630-1633, 2013.
- [6] G.-L. Wu, G. Zhao, and Y.-C. Jiao, "A novel design of dual circularly polarized antenna fed by L-strip," *Progress In Electromagnetics Research*, vol.79, pp. 39-46, 2008.
- [7] C. Zhang, X. Liang, X. Bai, J. Geng and R. Jin, "A broadband dual circularly polarized patch antenna with wide beamwidth," *IEEE Antennas and Wireless Prop. Letters*, vol. 13, pp. 1457-1460, 2009.
- [8] C.-H. Weng, H.-W. Zhao, and C.-F. Yang, "Dual circular polarization microstrip array antenna for WLAN/WiMAX applications," *Electronic Letters*, vol.46, pp. 609-611, 2010.
- [9] W. Hong, C.-T. Chenq, Y.-D. Lin and T. Kitazawa, "A novel dual circularly polarized microstrip antenna," *Proceedings of the 36<sup>th</sup> European Microwave Conference*, pp. 1629-1632, 2006.
- [10] M.T. Zhang, Y.B. Chen, Y.C. Jiao and F.S. Zhang, "Dual circularly polarized antenna of compact structure for RFID application," *Journal of Electromagn. Waves and Appl.*, Vol. 20, No. 14, 1895–1902, 2006.
- [11] Z.H. Jiang, D.E. Brocker, P.E. Sieber and D.H. Werner, "A compact, low-Profile metasurface-enabled antenna for wearable medical body-area network devices," *IEEE Trans. Antennas and Propagation*, vol. 62, no. 8, pp. 4021-4030, 2014.

- 
- [12] J. Joubert, J.C. Vardaxoglou, W.G. Whittow, and J.W. Odendaal, "CPW-fed cavity-backed slot radiator loaded with an AMC reflector," *IEEE Trans. Antennas and Propagation*, vol. 60, no. 2, pp. 735-742, 2012.
- [13] M. Qiu and G.V. Eleftheriades, "Highly efficient unidirectional twin arc-slot antennas on electrically thin substrates," *IEEE Antennas and Wireless Prop. Letters*, vol. 52, pp. 54-58, 2004.
- [14] M. Ramírez and J. Parrón, "Concentric annular ring slot antenna for global navigation satellite systems," *IEEE Antennas and Wireless Prop. Letters*, vol. 11, pp. 705-707, 2012.
- [15] W.L. Liu, M.-Y. Chen and T.R. Chen, "Wearable textile antenna is substrate integrated technology," *Microwave and Optical Tech. Letters*, vol. 54, no. 7, August 2012.
- [16] R. Moro, S. Agneessens and M. Bozzi, "A design for circularly polarized ring slot antennas backed by thin grounded substrate," *Electronic Letters*, vol. 48, no. 16, pp. 1768-1770, July 2012.
- [17] C. Löcker, T.Vaupel and T.F. Eibert, "Radiation efficient unidirectional low-profile slot antenna elements for x-band application," *IEEE Antennas and Wireless Prop. Letters*, vol. 53, pp. 2765-2768, 2005.
- [18] A. Vallechi and G.B. Gentili, "Microstrip-fed slot antennas backed by a very thin cavity," *Microwave and Optical Tech. Letters*, vol. 49, no. 1, pp. 247-250, 2007.
- [19] N. Nikolic, J.S. Kot and T.S. Bird, "Theoretical and experimental study of a cavity-backed annular-slot antenna," *IEE Proc.-Microw. Antennas Propag.*, vol. 144, no. 5, pp. 337-340. October 1997.
- [20] S.-W. Qu, J.-L. Li, Q. Xue and C.H. Chan, "Novel unidirectional slot antenna with a vertical wall," *Progress In Electromagnetic Research*, vol. 84, pp. 239-251, 2008.
- [21] J.Y. Park, C.-C. Chang, Y. Qian and T. Itoh, "An improved low-profile cavity-backed slot antenna loaded with 2D UC-PBG reflector," *Proc. IEEE AP-S Dig.*, vol.4, pp. 194-197, 2001-July.
- [22] G. Niyomjan and Y. Huang, "A suspended microstrip fed slot antenna on high impedance surface structure," *Proc. EuCAP, 2006-Nov.*
- [23] F. Elek, R. Abhari, and G.V. Eleftheriades, "A uni-directional ring-slot antenna achieved by using an Electromagnetic Band-Gap surface," *IEEE Trans. Antennas and Propagation*, vol. 53, no. 1, pp. 181-190, 2005.
- [24] X. Bao and M. J. Ammann, "Dual-frequency dual-sense circularly-polarized slot antenna fed by microstrip line," *IEEE Antennas and Wireless Prop. Letters*, vol. 56, no. 3, pp. 645-649, 2008.
-

- 
- [25] Y. Ranga, L. Matekovits, K.P Esselle and A.R. Wily, "Multioctave frequency selective surface reflector for ultrawideband antennas," *IEEE Antennas and Wireless Prop. Letters*, vol. 10, pp. 219-222, 2011.
- [26] D. Sievenpiper, L. Zhang, R.F.J. Broas, N.G. Alexopoulos, and E. Yablonovitch, "High-impedance electromagnetic surfaces with a forbidden frequency band," *IEEE Trans. Microw. Theory Tech.*, vol. 47, no. 11, pp. 2059–2074, Nov. 1999.
- [27] C.Y.D. Sim, F.R. Cai and Y.P. Hsieh, "Multiband slot-ring antenna with single- and dual-capacitive coupled patch for wireless local area network/worldwide interoperability for microwave access operation," *IET Microwaves, Antennas & Propagation*, Vol. 5, no. 11, pp. 1830–1835, 2011.
- [28] H. Mosallaei and K. Sarabandi, "Antenna miniaturization and bandwidth enhancement using a reactive impedance substrate," *IEEE Trans. Antennas and Propagation*, Vol. 52, no. 9, pp. 2403–2414, 2004.
- [29] J. Joubert and J.W. Odendaal, "Design of compact planar rat-race and branch-line hybrid couplers using polar curves," *Microwave and Optical Tech. Letters*, vol. 57, no. 11, pp. 2637-2640, 2015.
- [30] G. Mayhew-Ridgers, J.W. Odendaal and J. Joubert, "Single-layer capacitive feed for wideband probe-fed microstrip antenna elements," *IEEE Trans. Antennas and Propagation*, vol. 51, no. 6, pp. 1405-1407, 2003.
- [31] CST Microwave Studio 2015. [Online]. Available: <https://www.cst.com/>.
- [32] A. Vallechi, J.R. De Luis, F. Capolino and F. De Flavis, "Low profile fully planar folded dipole antenna on a high impedance surface," *IEEE Trans. Antennas and Propagation*, vol. 60, no. 1, pp. 51-62, 2012.
- [33] D.J. Kern, D.H. Werner, A. Monorcio, L. Lanuzza and M.J. Wilhelm, "The design synthesis of multiband artificial magnetic conductors using high impedance frequency selective surfaces," *IEEE Trans. Antennas and Propagation*, vol. 53, no. 1, pp. 8-17, 2005.
- [34] Y. Dong, H. Toyao and T. Itoh, "Compact circularly-polarized patch antenna loaded with metamaterial structures," *IEEE Trans. Antennas and Propagation*, vol. 59, no. 11, pp. 4329-4333, 2011.
- [35] S. Alam, N. Misran, B. Yatim and M.T. Islam, "Development of electromagnetic band gap structures in the perspective of microstrip antenna design," *International Journal of Antennas and Propagation*, 2013.

- 
- [36] R. Baggen, M. Martínez-Vázquez, J. Leiss, L.S. Drioli and P. de Maagt, "Low profile GALILEO antenna using EBG technology," *IEEE Trans. Antennas and Propagation*, vol. 56, no. 3, pp. 667-674, 2008.
- [37] J.R. Sohn, K.Y. Kim and H.-S. Tae, "Comparative study on various artificial magnetic conductors for low-profile antenna," *Progress In Electromagnetic Research*, vol. 61, pp. 27-37, 2006.
- [38] F. Yang and Y. Rahmat-Samili, "A low-profile circularly polarized curl antenna over an electromagnetic bandgap (EBG) surface," *Microwave and Optical Tech. Letters*, vol. 31, no. 4, pp. 264-267, 2001.
- [39] J. McVay, A. Hoorfar, and N. Engheta, "Small dipole-antenna near Peano high-impedance surfaces," *IEEE AP-S Int. Symp.*, Vol. 1, 305–308, 2004.
- [40] J. McVay, N. Engheta, and A. Hoorfar, "High impedance metamaterial surfaces using Hilbert-curve inclusions," *IEEE Microw. Wire. Comp. Lett.*, Vol. 14, No. 3, 130–132, 2004.
- [41] M. Hosseini and M. Hakkak, "Characteristics estimation for jerusalem cross-based artificial magnetic conductor," *IEEE Trans. Antennas and Propagation*, vol. 7, pp. 58-61, 2008.
- [42] K. Agarwal, Nasimuddin, and A. Alphones, "Wideband circularly polarized AMC reflector backed aperture antenna," *IEEE Trans. Antennas and Propagation*, vol. 61, pp. 1456-1461, 2013.
- [43] J.-M. Baracco, M. Paquay and P. de Maagt, "An electromagnetic bandgap curl antenna for phased array applications," *IEEE Trans. Antennas and Propagation*, vol. 53, no. 1, pp. 173-180, 2005.
- [44] W.E. McKinzie III and R.R. Fahr, "A low profile polarization diversity antenna built on an artificial magnetic conductor," *IEEE AP-S Int. Symp. Dig.*, vol. 1, pp. 762-765, 2002-Jun.
- [45] K. Agarwal, Nasimuddin, and A. Alphones, "RIS-based compact circularly polarized microstrip antennas," *IEEE Trans. Antennas and Propagation*, vol. 61, no. 2, pp. 547-554, 2013.
- [46] C. Ren, L. Bernard and R. Sauleau, "Investigations and design of small-size printed antennas on a reactive impedance substrate," *Proc. EuCAP, 2006-April*.
- [47] H.-D. Chen, J.-D Chen and J.-N. Li, "Ultra-wideband square-slot antenna," *Microwave and Optical Tech. Letters*, vol. 48, no. 1, pp. 500-502, 2006.

- 
- [48] C.-C. Lin, E.-Z Yu and C.-Y. Huang, "Dual-band rhombus slot antenna fed by CPW for WLAN application," *IEEE Trans. Antennas and Propagation*, vol. 61, no. 2, pp. 547-554, 2013.
- [49] C.-J. Wang and C.-H. Chen, "CPW-fed stair-shaped slot antennas with circular polarization," *IEEE Trans. Antennas and Propagation*, vol. 57, no. 8, pp. 2483-2486, 2009.
- [50] J.-S. Row, W.-L. Liu and T.-R. Chen, "Circular polarization and polarization reconfigurable designs for annular slot antennas," *IEEE Trans. Antennas and Propagation*, vol. 60, no. 12, pp. 5998-6002, 2012.
- [51] K.L. Wong, C.-C. Huang and W.-S. Chen, "Printed ring slot antenna for circular polarization," *IEEE Trans. Antennas and Propagation*, vol. 50, no. 1, pp. 75-77, 2002.
- [52] M. Gallo, E. Antonino-Daviu, M. Ferrando-Bataller, M. Bozzetti, J.M. Molina-Garcia-Pardo, and L. Juan-Llacer, "A Broadband Pattern Diversity Annular Slot Antenna," *IEEE Trans. Antennas and Propagation*, vol. 60, no. 3, pp. 1596-1600, 2012.
- [53] M.-H. Yeh, P. Hsu, and J.-F. Kiang, "Analysis of a CPW-fed slot ring antenna," *Proc. APMC*, vol. 3, pp. 1267-1270, 2001-Dec.
- [54] E.P. Irzinski, "The input admittance of a TEM excited annular slot antenna," *IEEE Trans. Antennas and Propagation*, vol. 23, pp. 829-834, Nov. 1975.
- [55] Y.-K. Jung and B. Lee, "Dual-band circularly polarized microstrip RFID reader antenna using metamaterial branch-line coupler," *IEEE Trans. Antennas and Propagation*, vol. 60, no. 2, pp. 786-791, 2012.